Analysis of Modern Landslide Deformations in the Thompson River Valley using InSAR

by

Jeffrey Journault

A thesis submitted in partial fulfillment of the requirements for the degree of

Master of Science

in

Geotechnical Engineering

Department of Civil and Environmental Engineering

University of Alberta

Abstract

The slow movement of historic landslides is a constant reality in the Thompson River Valley, with twelve such slides located within ten kilometers of the town of Ashcroft, B.C. alone. Beginning at the end of the 19th century, numerous rapid slope failures were reported by local residents and the two major Canadian railways occupying the corridor, Canadian Pacific (CP) and Canadian National (CN). These reports continued sporadically into the 20th century, with the most recent rapid failure occurring at the Goddard Slide in 1982. Today, slope movements in the Ashcroft area are more subdued, consisting primarily of slow displacements along established failure surfaces within or adjacent to historic landslide footprints.

The large spatial extent of the Thompson Valley and of most landslides contained within it has obliged railway operators to focus monitoring and investigative resources to the most active areas of instability. As part of this optimization effort, a small yet relatively active site, the Ripley Slide, was established as a research site for programs aimed at better understanding the mechanisms of instability within the corridor. This “field laboratory” has since supported a wide variety of geoscience research activities, ranging from material characterization, groundwater sampling, to a host of geophysical studies.

With the mechanisms of instability at the Ripley site becoming better understood, motivation has shifted to applying the lessons learned at Ripley to the other landslides in the area. In tandem with this shift, remote-sensing technologies have evolved and moved to the forefront of geotechnical science, largely due to their capacity to measure ground surface deformations over wide areas with great accuracy while at the same time requiring little to no ground-based equipment or works. Synthetic Aperture Radar Interferometry, or InSAR, is one such technology that has enabled researchers to expand geotechnical studies to the entire Ashcroft corridor.

Natural Resources Canada (NRCan) began acquiring radar images of the Thompson River Valley in 2011 using RADARSat-2, a Canadian Space Agency (CSA) satellite launched in late 2007 to replace the older RADARSat-1. In fall 2015, an interferometric analysis of the SAR images acquired up to that time was carried out using Persistent Scatterer Interferometry, or PSI.

This work presents a summary of the PSI analysis results, along with a review of landslide activity within Thompson Valley, a discussion of the technical background of InSAR, as well the validation of PSI results based on existing instrumentation data. In total, six zones of active ground deformation located within existing or historic landslide footprints are identified and discussed. The most active of these are the Ripley and Red Hill slides, both of which express clear seasonal variations in all PSI datasets. Following these in terms of deformation activity are the Goddard Toe, South Extension, and North Slide Toe. Finally, the Barnard slide has been identified as the least active AOI within the study area, showing subdued yet steady deformation over time.

Acknowledgements

Completing this work would not have been possible without the valuable contributions, both large and small, of many people to which I would like to offer my sincere thanks. First of these is Dr. Michael Hendry, not only for his supervision, patience, and financial support but also for opening the door to this research opportunity in the first place. Many thanks to Dr. Renato Macciotta for his enthusiastic support and numerous contributions to this research. Special gratitude is extended to Dr. David Cruden for his guidance during the early stages of this work.

I would like to acknowledge the essential support of Dr. Francois Charbonneau from NRCan, first for carrying out the bulk of the PSI analysis and second for assisting the author with understanding the finer details of interferometry. Additional thanks to Dr.'s Peter Bobrowski and David Huntley from the Canadian Geologic Survey, Tom Edwards of CN Railways, Chris Bunce of CP Rail, as well as my colleagues Matthew Schaffer, Gael Le Meil, and Kirsten Tappenedin for their various contributions along the way.

Final yet most sincere thanks go out to my wife, my family, and to my friends at home and abroad.

Table of Contents

List of Tables

List of Figures

Appendices

1.0 Introduction

Located within central British Columbia, the Thompson River Valley contains numerous landslides of various types, including rapid earth flows and slow-moving translational landslides. Twelve landslides are present within a ten-kilometer section of the valley near the town of Ashcroft (Tappenden 2014), many of which affect activities on the main lines of both Canadian National (CN) and Canadian Pacific (CP) railways (Figure 1-1). Though the area is sparsely populated, the potential risk associated with these landslides has motivated railway operators and government officials to support enhanced research activities in this area.

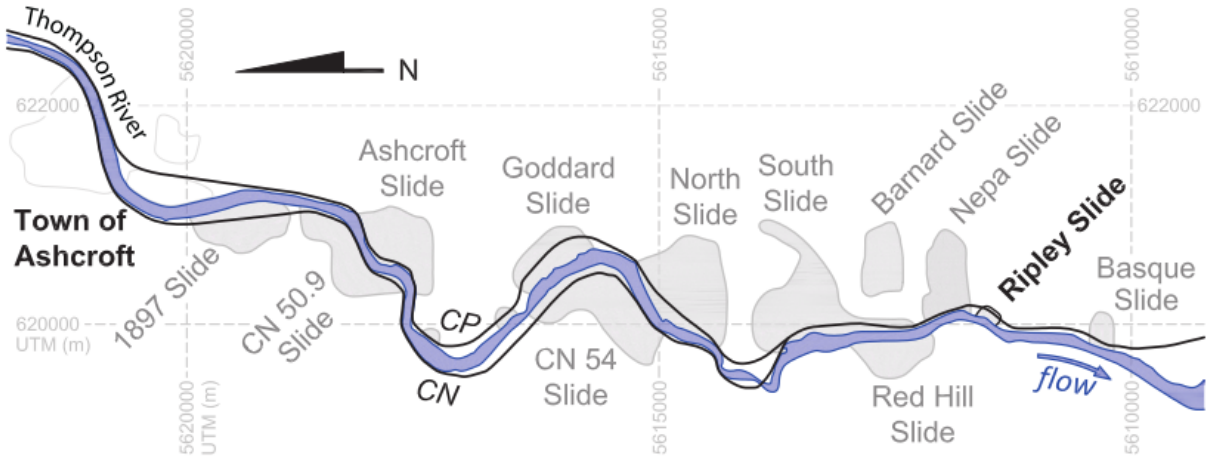

Figure 1-1: Landslides near Ashcroft, B.C. (Hendry et al., 2015)

The large spatial extent of the Thompson Valley and of many of the landslides contained within it has obliged these stakeholders to focus monitoring and investigative resources to the more active areas of instability. As part of this optimization effort, a small yet relatively active site, the Ripley Slide, was established as a research site for programs aimed at better understanding the mechanisms of instability within the corridor. This “field laboratory” has since supported a wide variety of geoscience research activities, ranging from material characterization, groundwater sampling, to a host of geophysical studies.

Based on the knowledge obtained from previous work at the Ripley Slide, there is now an opportunity to extend that understanding to the larger landslides within the valley using Synthetic Aperture Radar Interferometry, or InSAR.

1.1. Objectives

The specific objectives of this research study are as follows:

- Review the historical record of landslide activity within the study area to better understand the fundamental geologic forces affecting landslide behavior in the Thompson River Valley.
- Discuss the technical background of space-based InSAR with the aim of understanding the capabilities and limitations of the technology when it is used to measure ground deformations over a wide area.
- Validate the InSAR results obtained from the Thompson River Valley through comparisons with ground-based instrumentation measurements and observations taken from multiple sites within the study area.
- Once validated, expand the analysis of InSAR results to include all areas of interest (AOI) within the corridor to identify, delineate, and quantify concentrated ground movements.
- Evaluate the efficacy of using InSAR to detect active landslide activity within large geographic areas and thus allow more efficient allocation of additional monitoring resources.

2.0 Characteristics of Landslides in the Thompson Valley

2.1. Geologic Setting

The recent geologic history of the Thompson River Valley can be summarized as a series of glaciations punctuated by periods of erosion and river downcutting. Such events have filled the valley with a complex sequence of materials ranging from glacial deposits of poorly sorted sands and gravels to rhythmically bedded silts and clays (Figure 2-1). These periods of glaciation are demarcated by unconformities associated with interglacial periods of erosion and mass wasting (Clague and Evans 2003).

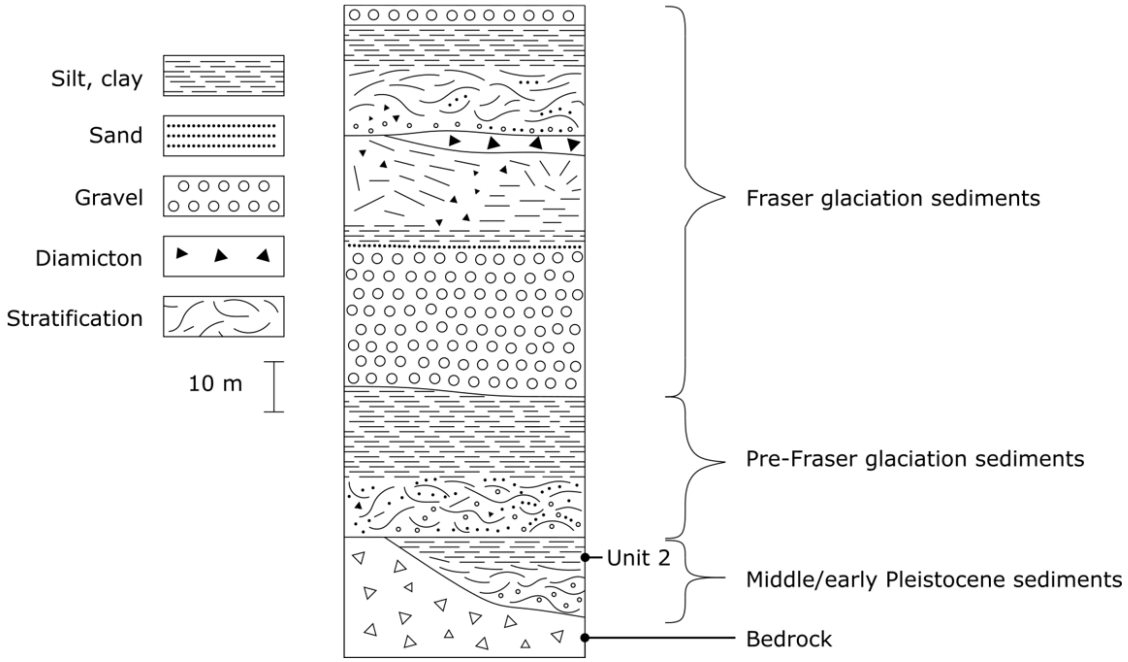

Figure 2-1: Glacial sediments near Ashcroft, B.C. (after Clague & Evans 2003)

One of the oldest deposits in the valley, a rhythmically bedded silt and clay located near the base of the sequence (shown above as Unit 2), has often been identified as being responsible for slope instability at many of the landslides within the valley (Porter et al. 2001, Clague and Evans 2003, Tappenden 2014). This older deposit appears to predate the Frasier Glaciation, having likely been deposited during the early or mid-Pleistocene (Clague and Evans 2003). This unit is particularly

weak as it contains many pre-sheared discontinuities that were formed either during periods of glacial advance and overriding or as a result of ancient slope movements (Eshraghian 2007).

With the retreat of the last glaciers to occupy the valley, the Thompson River rapidly down cut through the valley floor into the underlying glacial sediments creating a steep-walled inner valley (Eshraghian et al. 2007). Whenever this down cutting encountered the weakened clay and silt deposits, a large landslide would often form (Porter et al. 2001). Furthermore, portions of the valley where weaker materials are not present can be found supporting steep slopes and show no evidence of instability (Porter et al. 2001).

2.2. History of Activity

Accounts of large, rapid landslides in the Thompson Valley coincide with the arrival of western settlers and the subsequent construction of the two major national railway lines by CN and CP in 1895 and 1905, respectively (Tappenden 2014). This westward expansion of agricultural activity brought ditch-and-furrow irrigation to the valley, a method which essentially consisted of rapidly flooding entire valley terraces with water. This practice is commonly cited as a key contributor to several large slope failures from this time period as it would induce elevated pore pressures within soil that had up to that point been very dry (Barry 1897, Porter et al. 2001, Clague and Evans 2003, Bishop 2008, Tappenden 2014).

The earliest and most voluminous flow slide ever recorded within the corridor is the North Slide, which failed the evening of October 14, 1880 (Clague and Evans 2003). With an estimated volume of 15×10^6 m^3, the North Slide failed very rapidly, quickly blocking the flow of the Thompson River and eventually forming a lake nearly 14 km long which partially flooded the nearby town of Ashcroft (Clague and Evans 2003). The site has experienced several extremely slow translational reactivations along an initial failure plane since that time, two of which were significant enough to be reported by railway operators in 1997 and 2000 (Tappenden 2014).

Shortly after the failure of the North Slide, a second large and rapid flow slide occurred, most likely in 1881 (Eshraghian et al. 2007). Now known as the South Slide, this site followed a similar progression as the North Slide: several slow translational reactivations along historic failure planes following an initial rapid flow event. The most recent reactivation at this site occurred in 1997 after a period of flooding (Porter et al. 2001, Hendry et al. 2015). Since the initial failure, much of the activity at the South Slide has been attributed to erosion of the toe by the Thompson River. To combat this, a series of groins and other erosion protection measures were constructed along the toe of the South Slide, with largely successful results (Porter et al. 2001). While this work successfully slowed the rate of movement within the historic slide footprint, signs of instability in the adjacent slope immediately downstream were observed in an early InSAR analysis carried out in 2002 using data from RARDARSat-1 (Kosar et al. 2003, Froese et al. 2005).

The Goddard slide experienced its most recent retrogression in October 1886 (Eshraghian et al. 2008), which failed as a sudden translational flow with a volume of approximately 3 x 10^6 m^3 (Clague and Evans 2003, Bishop 2008, Tappenden 2014). This rapid failure was followed by several very slow translational reactivations until the site experienced a rapid reactivation in late September 1982 (Porter et al. 2001, Tappenden 2014). With an estimated volume of 2 x 10^6 m^3, this event completely disrupted railway traffic for 6 days after laterally displacing a 400 m section of track in excess of 30 m over only a few hours (Porter et al. 2001). Since 1982, the Goddard slide has remained a constant maintenance concern for CP operations due to very slow deformations that continue into this day (Bishop 2008).

The last flow slide for which the date of occurrence is known is the Red Hill Slide, which failed on August 21, 1921. Without warning, the event completely blocked the flow of the Thompson River for a short time and created a lake approximately 4 m deep (Clague and Evans 2003). The fact that a river flooding event occurred that same year may suggest that the Red Hill slide first failed

due to erosion at the toe of the slope (Porter et al. 2001). Little more is known about this site due to access difficulties and the fact that no railway lines traverse the slide at this location.

Located above the Thompson River on a valley terrace, the Barnard Slide is thought to have first failed several thousand years before present (Bishop 2008). The site has likely followed a similar pattern as the larger slides in the area, first failing as a rapid flow slide, reactivating in the late 19th century, and now moving as an extremely slow translation (Bishop 2008, Tappenden 2014).

The final landslide considered in this study is the Ripley Slide, which was first identified in 1951 by Charles Ripley after he reported an offset fence upslope from the CP railway tracks (Hendry et al. 2015). No rapid movements are suspected to have occurred at this site prior to its identification; however, the deformation rate did increase following the installation of a second CP track in 2005. Though smaller than the other landslides with an estimated volume of 1.0 x 10^6 m^3 (Eshraghian et al. 2007), the Ripley slide is scientifically important due to its current state of activity, ease of access, and high concentration of geotechnical monitoring instrumentation.

2.3. Landslide Kinematics

Due to their common geologic history, it is perhaps unsurprising that the landslides near Ashcroft share similar kinematic mechanisms in both their initial retrogressive failure and subsequent reactivations. Studies by others (Clague and Evans 2003, Eshraghian 2007) have suggested that cases of rapid slope failure in this area can be attributed to the initiation or retrogression of rupture surfaces within pre-weakened clay sediments due to river downcutting. These rapid retrogressive failures would then be followed by slow reactivations induced by the erosion of supporting material from the landslide toe. This sequence of retrogression followed by reactivation would often repeat as the river continued to cut into the weak clay deposits, leading to their classification by Eshraghian in 2007 as reactivated retrogressive multiple very slow to extremely slow translational earth slides (as per Cruden and Varnes 1996).

A good example of the resulting geometry of such a site can be seen at the Goddard Slide, which contains multiple blocks moving slowly along one or more rupture surfaces as the toe is eroded away (Figure 2-2).

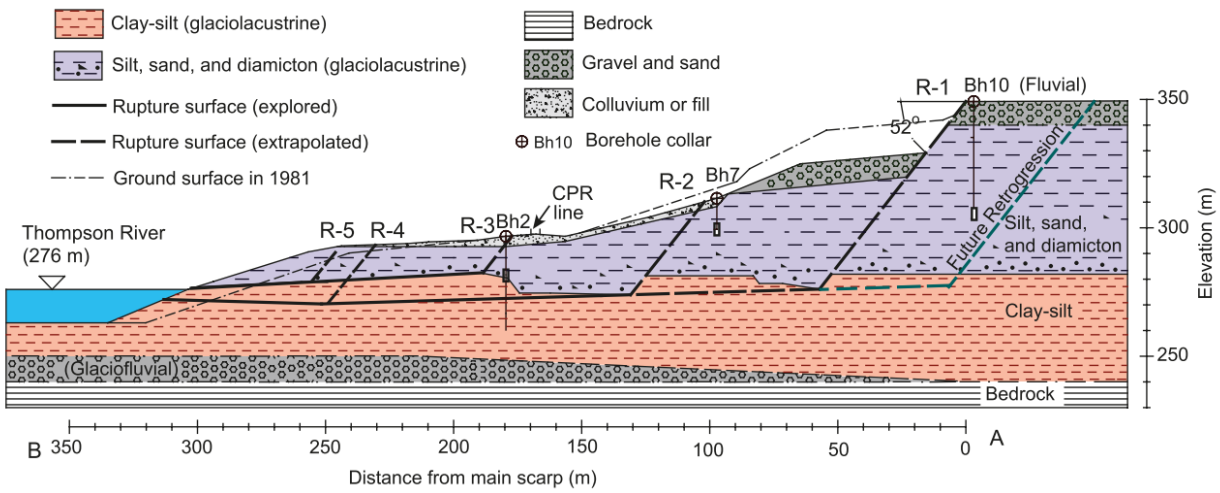

Figure 2-2: Cross section of Goddard Landslide (Eshraghian et al. 2008)

Aside from toe erosion, several other forces may cause landslide reactivations in the Ashcroft area. Often reactivation can be attributed to seasonal fluctuations in river level (Eshraghian 2007), which have been shown to correlate with landslide velocity, particularly at the Ripley Slide (Hendry et al. 2015). Anthropogenic forces that have contributed to slope instability include the crude irrigation practices introduced to the area with the arrival of western settlers at the turn of the 19th century (Clague and Evans 2003) as well as the modification of slope geometries due to construction and maintenance activities along the two railway lines running through the corridor.

3.0 Technical Background and Methodology for InSAR Analysis

3.1. Fundamentals of Interferometry

Synthetic Aperture Radar (SAR) satellites are active radar systems that transmit microwaves toward the earth's surface and record the signal reflected by individual points on the ground. The target area, or scene, is then partitioned into square pixels whose dimensions depend on the spatial resolution of the imaging mode used by the satellite to capture the image. Average values for the amplitude (A) and phase (ϕ) of the microwave signal reflected from within each pixel are then arranged into a two-dimensional complex valued image, hereafter referred to as a SAR image (Colesanti and Wasowski 2006, Wasowski and Bovenga 2014). In this form, the signal amplitude represents the reflectivity of the ground within each pixel (Froese et al. 2005) and can be used for multiple applications, including material distribution and land use mapping. The signal phase is representative of the distance between the SAR antenna and the scattering center of each pixel. However, due to its periodical form (limited to 2π) the phase data from a single SAR image is ambiguous and the total sensor-target distance cannot be determined.

Despite this ambiguity, it is possible to extract useful information from the signal phase using interferometry, or InSAR. This process compares the phase signal from two or more SAR images taken of the same area using identical imaging geometry but from different times and generates images called interferograms, which spatially represent the change in signal phase between each SAR image. This change, called the interferometric phase difference ($\Delta\phi$), can be expressed in terms of the microwave signal wavelength (λ) and the difference in geometric distance along the line of sight (LOS) between the satellite sensor and a given target for each SAR image (R_1, R_2) as per Equation 3.1 and Figure 3-1 (Wasowski and Bovenga 2014).

$$\Delta\phi = 2\pi \frac{(R_1 - R_2)}{\left(\frac{\lambda}{2}\right)} = \frac{4\pi}{\lambda} dR \qquad [3.1]$$

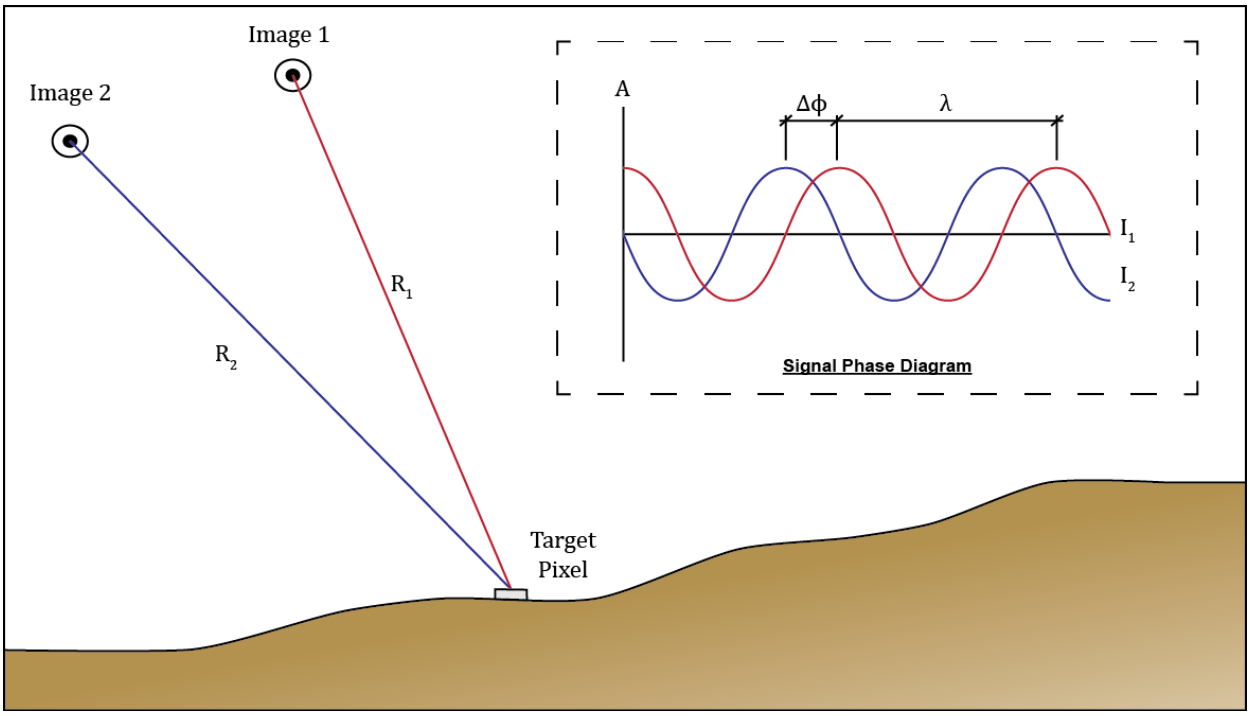

Figure 3-1: Fundamental Geometry of InSAR

The difference in sensor-target distance (dR) can be further reduced to four distinct constitutive factors (Simons and Rosen 2007, Wasowski and Bovenga 2014), each of which arises from either geometric variations or temporal changes between SAR images (Equation 3.2).

$$dR = dR_{topo} + dR_{disp} + dR_{atm} + dR_{noise} \quad [3.2]$$

It is thus possible to quantify ground displacements occurring between each SAR acquisition (dR_{disp}) using the calculated phase difference ($\Delta\phi$) so long as the topographic residual (dR_{topo}), atmospheric effects (dR_{atm}), and decorrelation sources (dR_{noise}) can be accounted for and eliminated; this concept forms the fundamental basis of interferometry (Ferretti et al. 2007).

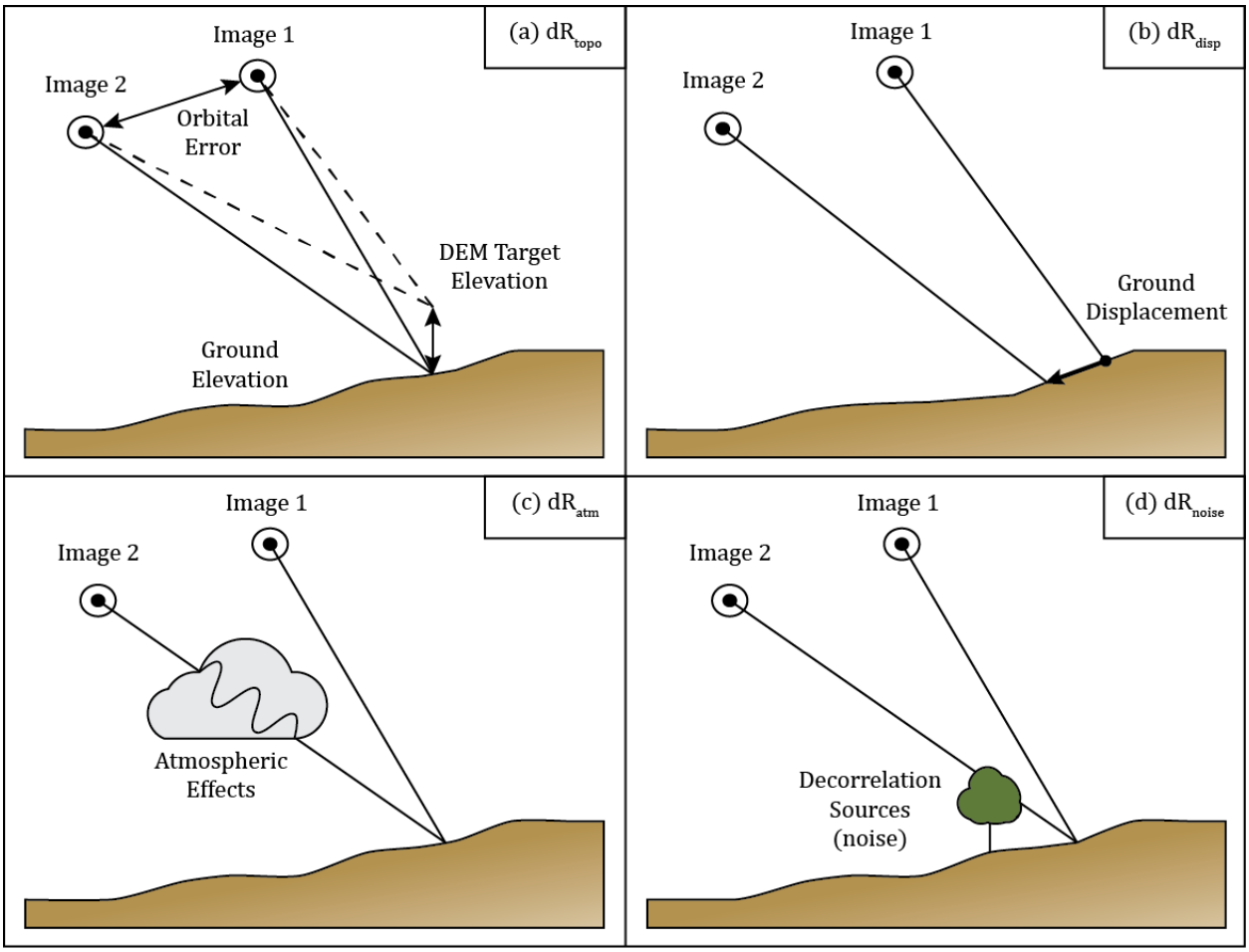

Note: (a) Geometric error, (b) ground displacements, (c) atmospheric effects, and (d) sources of decorrelation or noise.

Figure 3-2: Factors Affecting the Measured Sensor-Target Distance

The first component to be resolved from dR is the topographic residual (dR_{topo}), which arises from discrepancies between the ground elevation predicted by the reference digital elevation model (DEM) used for the analysis and that of the actual ground surface, as well as from inaccuracies in the recorded orbital position of the satellite during each SAR acquisition (Figure 3-2a). A prerequisite condition of interferometry is that the orbital position of the satellite during sequential SAR acquisitions must be very similar. The fortunate consequence of this is that interferometry is relatively insensitive to topographic variations due to the necessarily acute angle between subsequent LOS vectors. Therefore, a DEM of only moderate accuracy is sufficient to reduce the topographic residual to a negligible amount (Ferretti et al. 2007).

Though SAR imaging is technically capable of operating independent of atmospheric conditions, the temperature, pressure, and refractivity index of the air can each effect the "perceived" path length of the microwave signal as it travels through the atmosphere (Figure 3-2c). As these conditions vary unpredictably with time, their distorting effect (dR_{atm}) will be unique to each SAR image of a given area. Therefore, the effect of atmospheric change must be accounted for before ground deformations can be resolved using interferometry. Despite their unpredictability through time, atmospheric conditions can be assumed to vary smoothly through space. Thus, it is possible to utilize algorithmic processing to filter out their phase contribution so long as enough SAR images are available.

A second temporal factor affecting the measured sensor-target distance is that which arises from sources of decorrelation or noise (dR_{noise}). Many phenomena can cause signal noise, often by randomly affecting the reflectivity or phase length associated with a given target pixel. Example sources of decorrelation in the Thompson River Valley include seasonal vegetation, snow cover, or excessive surface erosion (Figure 3-2d). This effect is often mitigated using an algorithmic filter to remove sources of high decorrelation from InSAR results, leaving behind only the most consistent targets.

Once the above components of dR have been accounted for, the only remaining term in Equation 3.2 is dR_{disp}, which represents the magnitude of ground deformations along the satellite LOS. It is important to note that the value of this term is dependent on the relative direction of ground movement with respect to the satellite viewing geometry. When deformations occur in a direction away from the satellite dR_{disp} will be negative, while the opposite is true for deformations toward the satellite.

3.1.1. Differential Stacking

One of the early algorithmic techniques developed to mitigate the distorting effects of the atmosphere is a process called differential stacking interferometry, or DSI (Sandwell and Price 1998). This technique “stacks” and averages the phase differences from multiple interferograms to generate a single interferogram relatively free of atmospheric distortion (Ferretti et al. 2007). The topographic residual is accounted for using a separate DEM, while contributions due to atmospheric effects tend to average to zero if an adequate number of SAR images are available for processing (Colesanti and Wasowski 2006).

This technique is desirable in the sense that it is less computationally intense compared to more advanced algorithmic methods. However, it is not well suited to detecting small areas of isolated yet rapid deformation as such displacements tend to be smoothed-out during DSI processing.

3.1.2. Persistent Scatterer Interferometry

A second more advanced processing technique is Persistent Scatterer Interferometry, or PSI. This algorithm seeks out and identifies targets (CT) within a scene that represent locations where the microwave signal phase can be reliably measured through time (Wasowski and Bovenga 2014). CT are selected based on their inter-image coherence (γ), which is related to the standard deviation of the measured phase differences and calculated as a statistical measure of the stability of the phase data. High coherence at a given point implies that the radar scattering properties and thus the interferometric phase change data at that point are less variable. As a result, the PSI algorithm selects CT by comparing the coherence of each pixel to a threshold minimum value that must be exceeded before a point is designated as a CT (Wasowski and Bovenga 2014). A secondary benefit of selecting only points of high coherence is that the deleterious effects of atmospheric distortion and noise are filtered out, greatly reducing their influence on the results of PSI analysis.

Examples of ideal CT include buildings, stable rock outcrops, or purpose-built artificial corner reflectors (CR). Once designated, the time-series deformation between sequential SAR image acquisitions can be calculated at each CT (Colesanti and Wasowski 2006). The final product of PSI processing is a dataset consisting of the geographic coordinates, phase difference variability, and the time-series displacements for each CT within the processed scene (Colesanti et al. 2003).

3.2. InSAR Analysis in the Thompson River Valley

3.2.1. Previous Work

This study is not the first instance of using InSAR to monitor ground deformations within the Thompson River corridor, but rather a continuation of earlier work carried out by others in 2002 (Kosar et al. 2003) and 2005 (Froese et al. 2005). This early work synthesized data from the satellites RADARSat-1 (Canadian Space Agency, CSA), ERS-1, and ERS-2 (European Space Agency, ESA) to search for and quantify surface deformations using differential interferometry. The results of this work were promising for the time, producing spatial deformation maps which were relatively consistent with ground-based observations made over the same time period.

3.2.2. Current Study

With the launch of RADARSat-2 in 2007 by the CSA, the spatial resolution of SAR data available for civilian use increased considerably. Given the promising results of earlier work in the area, the Thompson River corridor was as an ideal candidate for more detailed analysis using the advanced capabilities of RADARSat-2. Collection of east-facing SAR images in the area began in spring 2011, while the first west-facing SAR images were acquired in September 2013. Though the collection of both image types continues to this day, this study only considers data collected up to October 2015. The typical time interval between RADARSat-2 acquisitions is 24 days (CSA 2015), however some larger gaps are present within the available datasets.

In total, this work considers one east facing and two west facing CT datasets, the geometric and temporal details of which are summarized in Table 3-1.

Table 3-1: Summary of RADARSat-2 Acquisition Datasets

PSI Dataset	Total Time of Observation (days)	Scanning Mode (Spatial Resolution)	Satellite Line of Sight (LOS)	
			Azimuth (degrees from North)	Incident angle (degrees from zenith)
U5	768	Ultra-Fine (3 m)	280	34
U21	696	Ultra-Fine (3 m)	280	45
F4N	1632	Fine (8 m)	80	44

3.2.3. Analysis of PSI Results

In collaborative effort between the Geologic Survey of Canada (GSC), Natural Resources Canada (NRCan), and the University of Alberta, PSI processing of RADARSat-2 imagery was carried out in October 2015. Input from CGS scientists, InSAR specialists, and the author ensured that PSI processing achieved an accurate representation of landslide activity in the study area. PSI results were then imported into a GIS program by the author for data visualization and spatial analysis. ArcGIS 10.3 (ESRI 2015) was chosen for this work due to its capabilities, availability, and relative ease of use. Spatial analysis was also aided significantly by the availability of high-resolution aerial photographs and LiDAR survey data acquired over the area in fall 2015 by CN Rail.

3.2.3.1. Precision of PSI Deformation Measurements

It is difficult to evaluate the quantitative precision of PSI analysis due to the necessity of critical, non-linear steps inherent to PSI processing (Wasowski and Bovenga 2014). These steps, in addition to several temporal and geometric factors detailed later in Section 3.3, make such an evaluation challenging. Nonetheless, others have shown that given an adequate CT density, suitable deformation model, and appropriate acquisition frequency modern InSAR systems can be expected to achieve accuracies of $\pm$1 mm/year for average displacement rates and $\pm$5 mm for individual displacement measurements (Wasowski and Bovenga 2014, Cloutier et al. 2015).

3.2.3.2. Spatial Distribution of Ground Deformations

It can be difficult to visualize the distribution of PSI data in its raw form as it consists of thousands of points randomly scattered across a target area. Thus, an initial step of this analysis was to generate movement intensity maps to better represent the interpolated distribution of annual deformation rates across the target scene. This processing was done in ArcGIS using the Inverse Distance Weighted (IDW) tool from the Spatial Analysist toolbox. This simple tool assigns a value to each cell within the processing area using the distance-weighted average of deformation rates from neighboring CT (ESRI 2015).

By overlaying these images above the high-resolution DEM and satellite imagery, the extent of each concentrated movement zone could be seen in detail. This clarity helped focus later analysis to include only those CT contained within the re-defined extents of each movement zone. Additionally, the intensity maps aided data validation efforts by allowing various ground-based instrumentation, such as slope inclinometers, GPS stations, or artificial corner reflectors (CR) to be spatially located within or alongside each movement zone.

3.2.3.3. Estimated Downslope Deformation Rate

One of the primary limitations of InSAR is that it is only capable of measuring deformations along the satellite LOS (Colesanti and Wasowski 2006) and is thus incapable of capturing three-dimensional displacement information using a single viewing geometry. Instead, measured LOS deformation rates (D_{LOS}) should be thought of as the projection of the actual 3D ground movement vectors along the satellite LOS. The LOS itself can be defined by a so-called sensitivity versor ($\overline{U}_{LOS}$), which is a unit vector parallel to the LOS oriented toward the satellite from the target location (Wasowski and Bovenga 2014).

Since the 3D components of actual ground movement vectors cannot be determined using one-dimensional InSAR measurements, the true magnitude of ground deformation is incalculable

using InSAR alone. However, if it is assumed that ground deformations occur in a direction defined by a unit vector ($\overline{U}_{slope}$) oriented along the average aspect and inclination (or dip and dip direction) for a given AOI, the deformation rate in the downslope direction (D_{slope}) can be estimated. This is done by mathematically reversing the projection of the assumed downslope deformation vector onto the sensitivity versor as per Equation 3.3 (Colesanti and Wasowski 2006):

$$D_{slope} = \left(1/\overline{U}_{slope} \cdot \overline{U}_{LOS}\right) \times D_{LOS} = S \times D_{LOS} \quad [3.3]$$

In the above equation, S represents a scalar factor whose value is dependent on the angular difference between $\overline{U}_{LOS}$ and $\overline{U}_{slope}$. If the two vectors are exactly parallel, S will be equal to unity. Conversely, as the two vectors approach orthogonality, S tends to infinity. If the angular difference between the two vector directions exceeds $90°$, the value of S will become negative, implying that the downslope vector is oriented away from the satellite. In addition to facilitating the estimation of downslope deformation rates, *S* can be used to quantify the amount of movement captured at a given AOI by each InSAR dataset by defining the inverse of S as the percentage of movement captured (P_C) by each viewing geometry as per Equation 3.4:

$$P_C = {}^{1}/_{S} \times 100\% \quad [3.4]$$

For example, at the Ripley Slide the value of S associated with the U5 dataset is -1.4, which corresponds to a P_C of 71%. However, the value of S associated with the F4N dataset at the same site is 2.7, which corresponds to a much lower P_C of 37%. Thus the value of S can be used as a means of assessing the precision of PSI deformation measurements for a given AOI and viewing geometry (Colesanti and Wasowski 2006). Once the values of S associated with each InSAR dataset and AOI have been determined, the previously disparate LOS deformations can be directly compared to one another in terms of downslope deformation. Furthermore, an overall estimate of the average downslope deformation rate for each AOI can be obtained using a weighted average biased toward those InSAR datasets whose S values are nearest to unity.

3.3. InSAR Limitations

3.3.1. Temporal Decorrelation

The utility of PSI is highly dependent on the density, or lack thereof, of natural coherent radar targets (Wasowski and Bovenga 2014). Cases of low CT density commonly arise in areas with few stable rock outcrops, extensive vegetation, sparse urbanization, variable snow cover, or unfavorable slope geometry, all of which can cause phase decorrelation (van Zyl 2009, Wasowski and Bovenga 2014). This limitation can be overcome in some cases by utilizing SAR imagery from both the ascending and descending orbital directions, or by installing artificial corner reflectors to increase the number of CT within a target area (Wasowski and Bovenga 2014).

3.3.2. Geometric Orientation of Slope Relative to Satellite LOS

As previously mentioned in Section 3.2.3.3, the sensitivity of InSAR to downslope movement is directly affected by the relative geometry of the satellite LOS and the aspect and inclination of the target slope (Colesanti and Wasowski 2006, Wasowski and Bovenga 2014). Ideally, ground deformations would occur in a direction sub-parallel to the LOS, thus allowing the satellite to fully capture actual ground displacements. However, in practice the LOS is offset from the ground movement vector in both aspect and inclination, meaning InSAR will detect only a portion of actual ground movements (Wasowski and Bovenga 2014). In the case of ground deformations moving in a direction orthogonal to the LOS, ground deformations are undetectable using InSAR.

Addressing this limitation by assuming a direction of ground displacement introduces its own set of concerns. Any error in the processed data will be scaled by the same factor S as the LOS deformation (D_{LOS}). Thus, the accuracy of the estimated downslope deformation rate (D_{slope}) is directly dependent on the value of S used in its computation; the larger the value of S, the greater the error in the estimated deformation rate. The estimated downslope deformation rate is also directly affected by the accuracy of the assumed ground movement direction ($\overline{U}_{slope}$). If the

difference between the assumed and actual ground displacement vector is large, the calculated ground displacement rate may be incorrect by a wide margin.

It is therefore of vital importance to select a satellite whose azimuth and inclination angle(s) are most appropriate for the site(s) under consideration as this will have a direct influence on the utility and accuracy of the results obtained. Additionally, a studied understanding of the expected kinematic behavior within each target area is essential in avoiding misinterpretation or misrepresentation of InSAR results (Colesanti and Wasowski 2006).

3.3.3. Rapid Ground Movements

An additional limitation of InSAR is its inability to detect very rapid ground movements. Short-lived phenomena, such as sudden slope failures, occur too rapidly for InSAR to properly capture in detail as they are likely to exceed the phase length of the radar signal. This introduces aliasing errors into the dataset, which make data processing significantly more difficult if not impossible. These events are also likely to destroy or displace most if not all CTs within the impacted area, thus breaking the continuity of PSI analyses at such a site.

3.3.4. Acquisition Frequency

Finally, InSAR systems are limited by their SAR image acquisition frequency. As current systems are unable to provide near-daily coverage of an area of interest, they cannot yet be relied upon to provide early warning of impending ground deformations. For the time being, such a role remains the domain of other ground-based monitoring technologies.

4.0 Validation of InSAR Results

Given the number of factors that can influence the accuracy of InSAR measurements, it has been necessary to validate the Thompson River Valley PSI results before proceeding with a detailed analysis. Validation was achieved through a qualitative comparison between InSAR results and ground-based instrumentation data or field observations at select locations within the study area. Specifically, this work focused on three sites: the Ripley Slide, South Extension, and a concrete pump station structure (Figure 4-1).

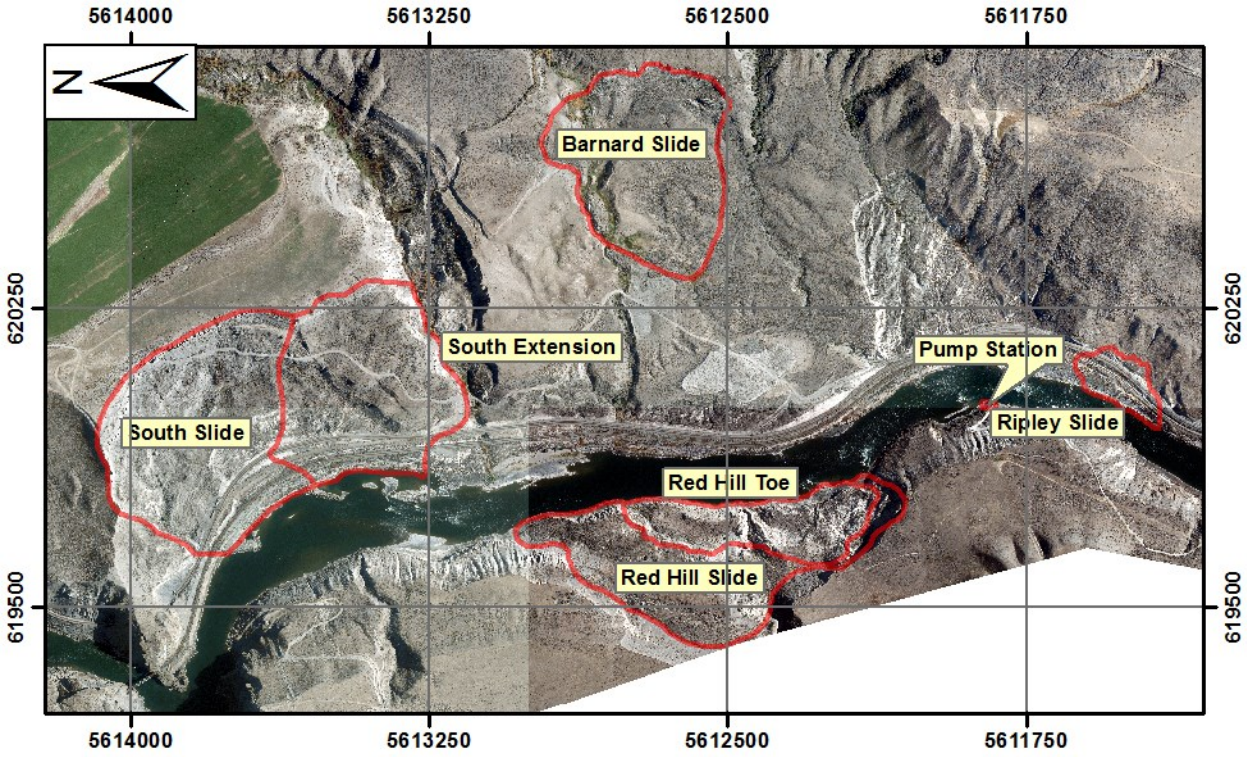

Figure 4-1: InSAR Validation Area

4.1. Ripley Slide GPS Stations

The Ripley Slide is ideally suited to InSAR validation as it has been well studied and hosts a large variety of geotechnical instruments (Figure 4-2). Here, validation efforts focused on comparing the three-dimensional movement of permanent GPS stations to the displacement of nearby CT

and GSC corner reflectors. The GPS stations have been in place since 2008 (Macciotta et al. 2015), with recorded data available through to October 2014.

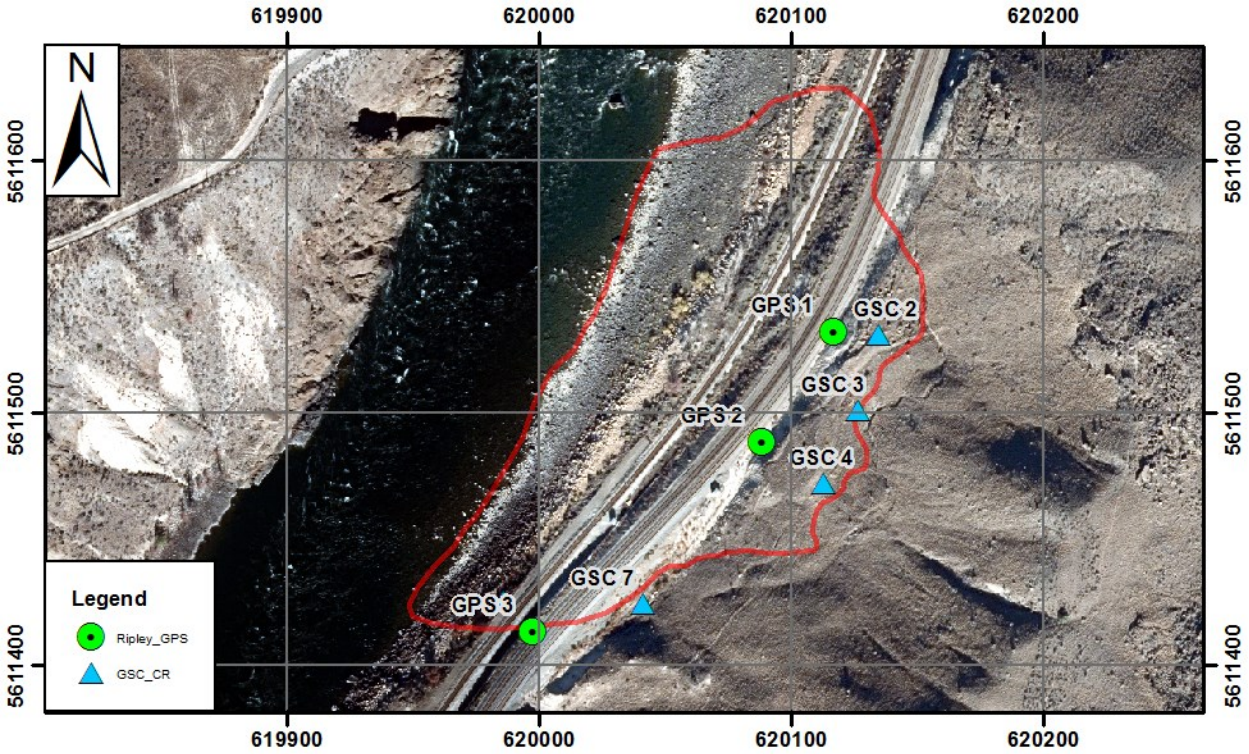

Figure 4-2: Plan View of Ripley Slide with GPS Stations

The U21 dataset was selected for validation analysis at Ripley as it has the highest percent coverage and CT density of the three available PSI datasets (82% and 1505 CT/km^2, respectively). Prior to comparing the 3D GPS data to the scalar LOS deformation of nearby U21 CT, the two measurement types had to be made geometrically equivalent. This was accomplished by projecting the known 3D GPS deformations onto the sensitivity versor of the U21 LOS. The projected GPS data was then directly compared to the LOS deformation of U21 CT within a 25 m radius of each GPS station.

Overall, these comparisons produced satisfactory results, especially at GPS stations 1 and 2, while results at GPS-3 were less successful due to the nature of its location and immediate surroundings. The following sections describe InSAR validation at each GPS station in detail.

4.1.1. GPS-1

The northernmost station at the Ripley Slide, GPS-1 is located immediately up-slope and adjacent to the CP rail lines (Figure 4-3). From November 2013 through October 2014 this station reported total horizontal and vertical displacements of 57.9 and -12.0 mm, respectively. Projected onto the U21 sensitivity versor, this equates to a cumulative displacement of -50.3 mm along the satellite LOS. Comparing this projected GPS-1 deformation to nearby U21 CT yielded promising results, with deformations at the station falling within one standard deviation of the average CT deformations. The median CT movement was an even closer match to GPS-1, while the corner reflector GSC-2 followed GPS-1 almost exactly (Figure 4-4).

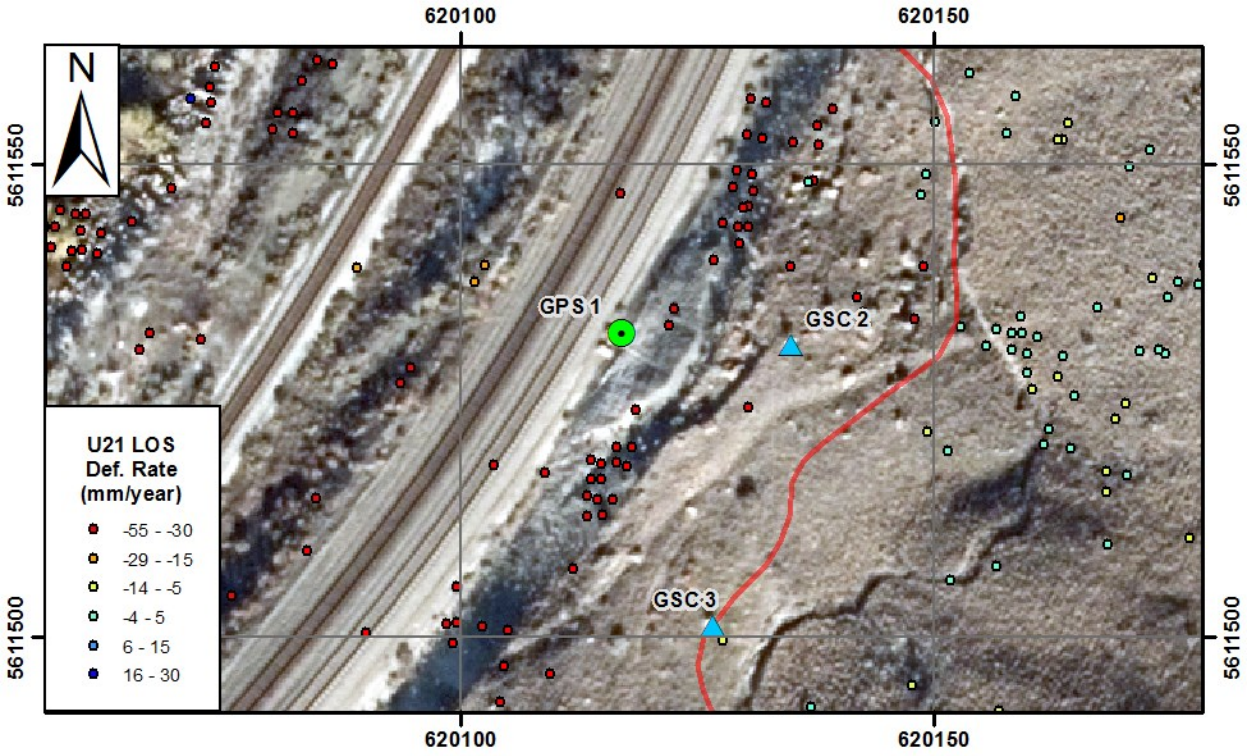

Figure 4-3: U21 CT Distribution near GPS-1

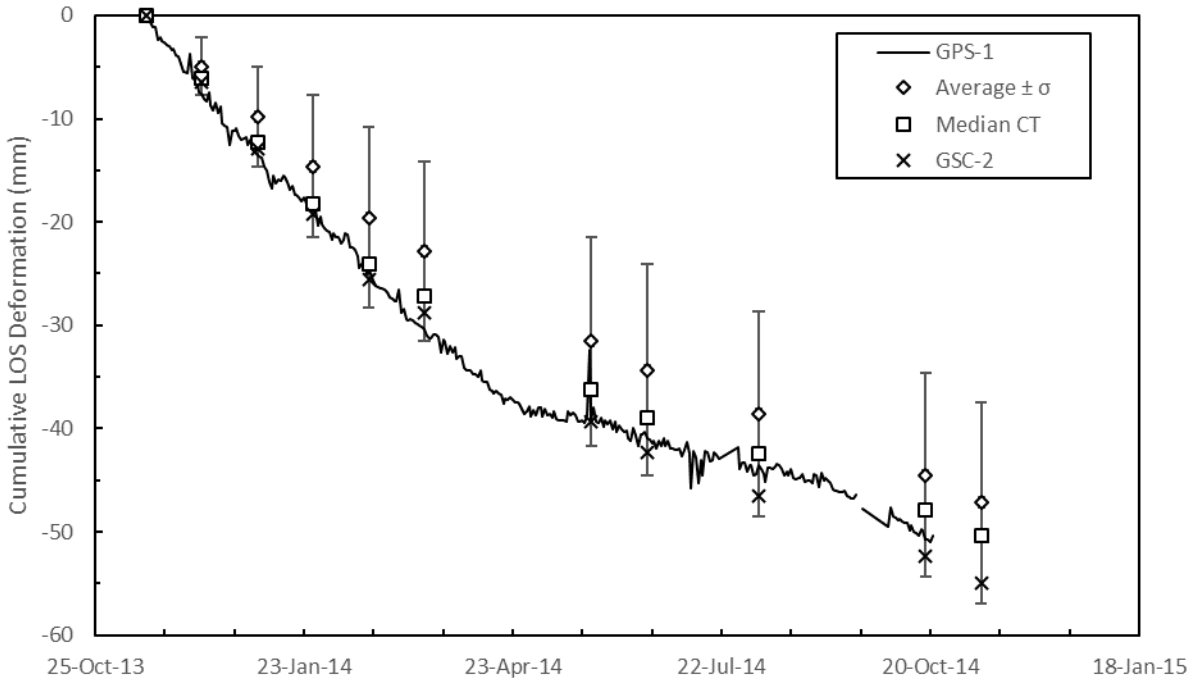

Figure 4-4: GPS-1 vs. CT Displacement along U21 LOS

4.1.2. GPS-2

Located near the centre of the Ripley AOI, GPS-2 is immediately adjacent to the CP rail lines at the base of a steep cutback slope (Figure 4-5). From November 2013 through late July 2014, this station reported total horizontal and vertical displacements of 55.2 and -11.0 mm, respectively. This equates to a cumulative U21 LOS displacement over the same period of -47.2 mm. The projected GPS-2 deformation again compares favorably to nearby U21 CT, however less so than at GPS-1, falling within two standard deviations of the average U21 cumulative deformation trend (Figure 4-6). Of interest is the observation that, of the 37 CT selected from the vicinity of GPS-2, many of the closest CT matched poorly to the reported GPS-2 deformation, while those further away on the natural slope matched more closely. Many of the poorly matching CT are situated on the steep cutback slope adjacent to the GPS station, suggesting that either the geometry of the cutback or perhaps some erosive or depositional phenomena is interfering with the U21 CT results along this steep slope feature.

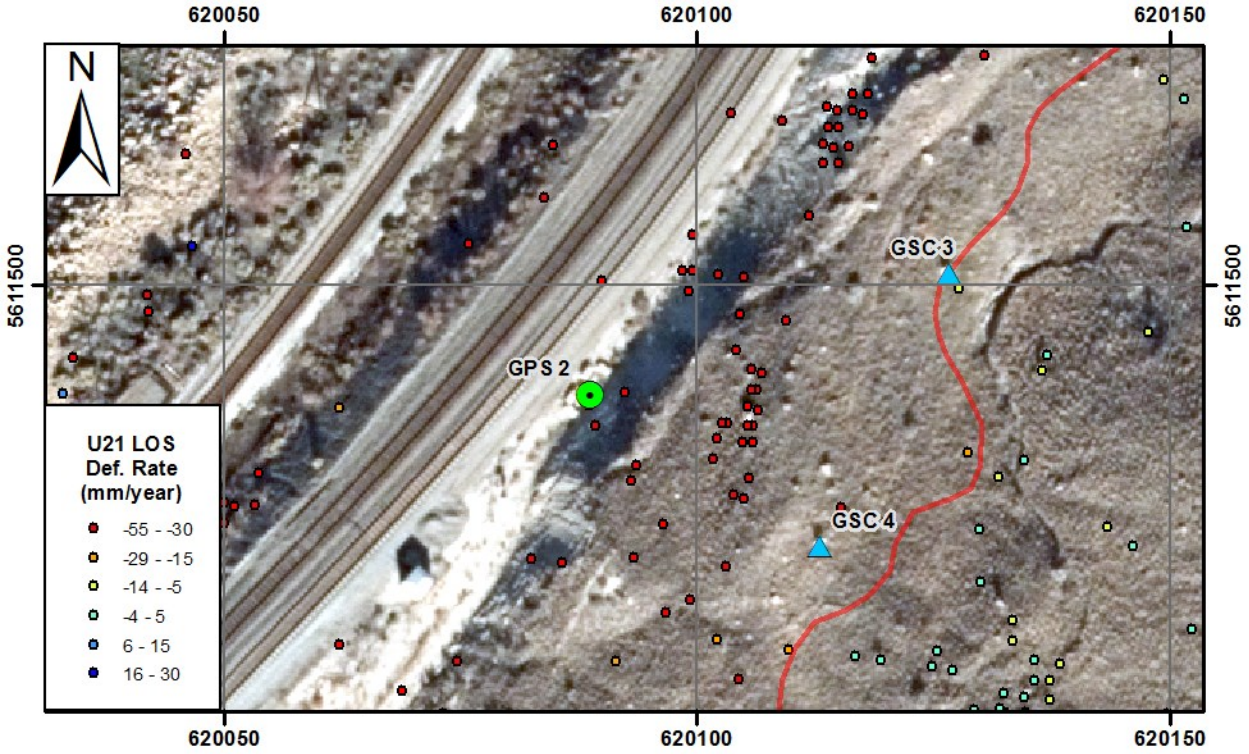

Figure 4-5: U21 CT Distribution near GPS-2

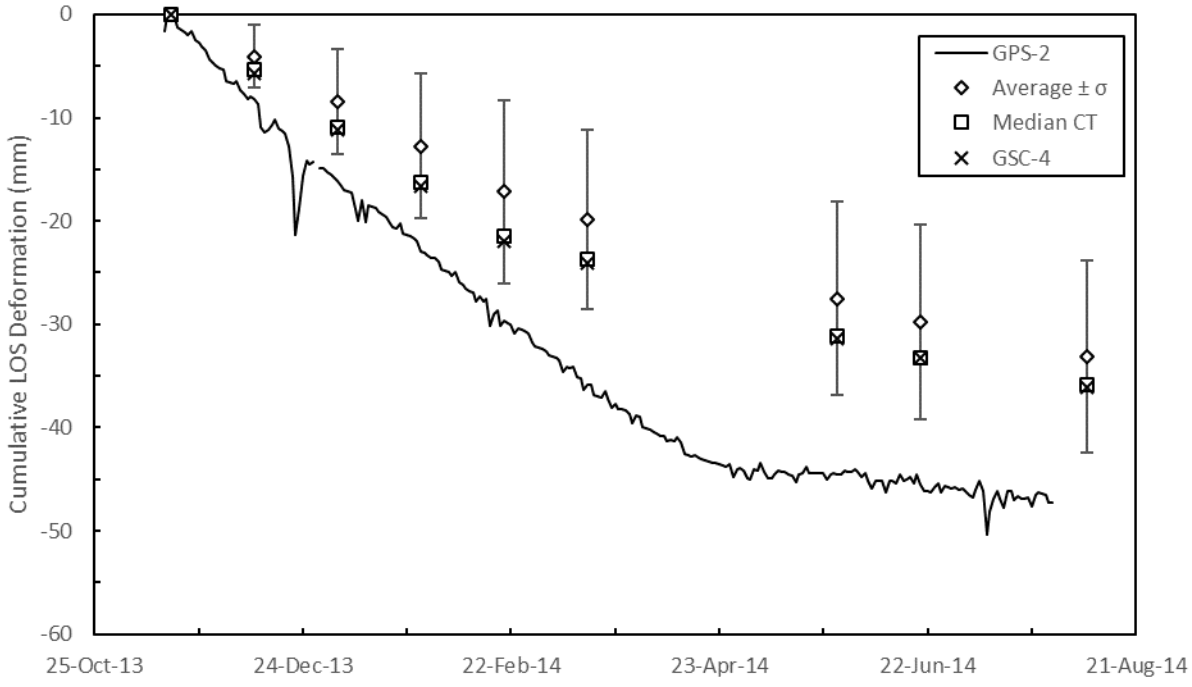

Figure 4-6: GPS-2 vs. CT Displacement along U21 LOS

4.1.3. GPS-3

Unlike GPS-1 and 2, PSI validation at GPS-3 did not produce favorable results. The station itself reported respective horizontal and vertical deformations of 77.9 and -55.0 mm from November 2013 through October 2014. Projected onto the U21 LOS direction, this equates to a cumulative deformation of -90.0 mm. Unlike GPS-1 and 2, GPS-3 is located downslope from the CP rail lines at the top of a vertical lock-block retaining wall, which itself straddles the southern boundary of the Ripley AOI (Figure 4-7). Comparing the projected GPS-3 movement to that observed at nearby U21 CT reveals a large disparity between the two measurement types, with none of the U21 CT or GSC corner reflectors moving as quickly as the GPS station itself.

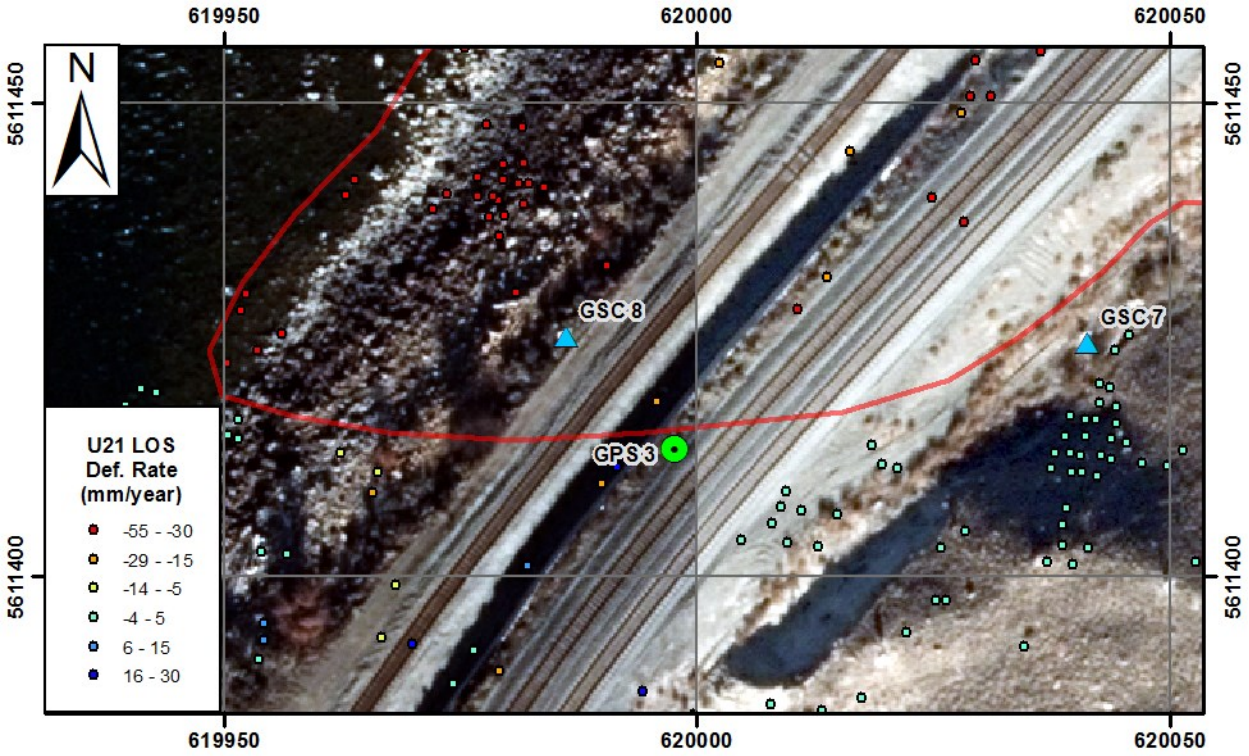

Figure 4-7: U21 CT Distribution near GPS-3

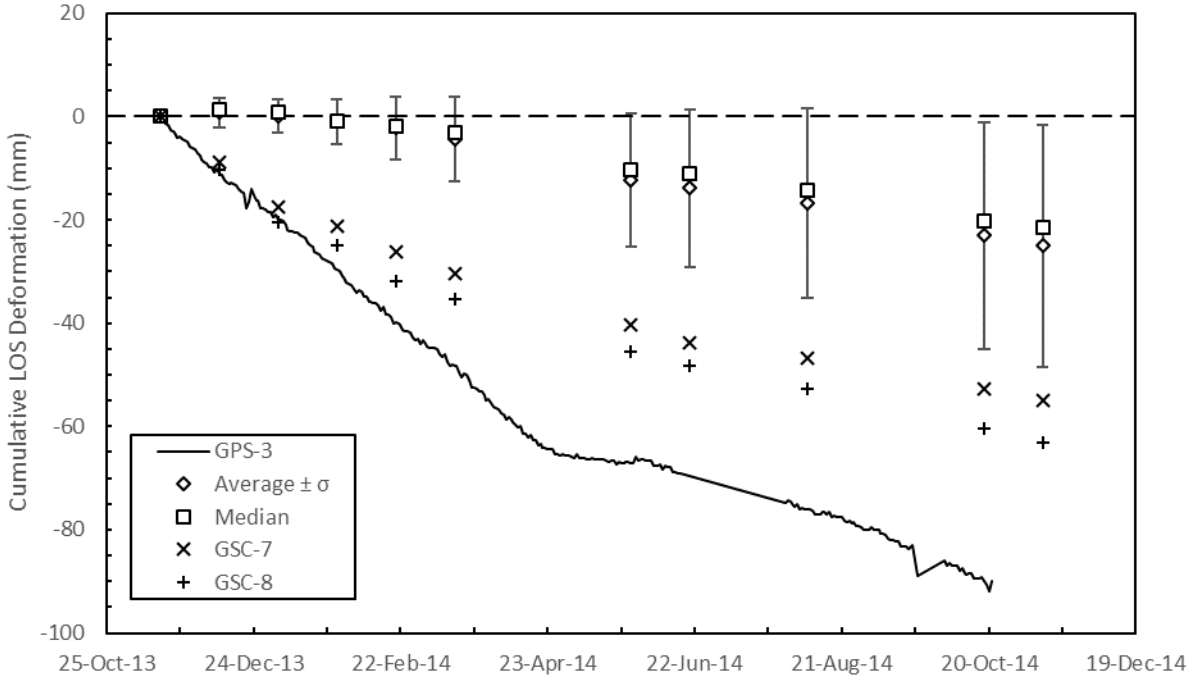

Figure 4-8: GPS-2 vs. CT Displacement along U21 LOS

It is likely that the disparity between GPS-3 and CT data originates from several factors working together to confound PSI analysis at this location. First among these is the nature of the deformations at GPS-3. Whereas GPS-1 and 2 report nearly horizontal deformations, GPS-3 is experiencing much more vertical deformation due to the localized settlement of the lock-block wall below the station. Other factors which complicate PSI analysis at this location include the unfavorable viewing geometry of the vertical lock-block wall relative to the west-facing datasets, frequent maintenance of nearby rail lines, and the station's location on the edge of the Ripley AOI. Thankfully, these confounding factors are localized to the area immediately surrounding GPS-3 and thus should not be seen to invalidate PSI results taken from Ripley or the wider study area.

4.2. South Slide Inclinometers

Located 2 km north of the Ripley Slide, the South Slide was selected for InSAR validation as it is relatively active and contains geotechnical instrumentation within the active zone. Specifically, validation focused on a portion of the South Slide situated on the southern flank of the historic footprint. This active zone, herein referred to as the “South Extension”, is approximately 450 x 450 m in size (Figure 4-9). Surface materials found at this site range from previously disturbed landslide debris to valley terraces undisturbed in modern history.

Of the three available PSI datasets, the U21 dataset has the highest percent capture and CT density (85% and 1304 CT/km^2, respectively) within the South Extension. Therefore, InSAR validation at the South Extension focused on U21 CT only, as they are most representative of actual surficial deformations in this area.

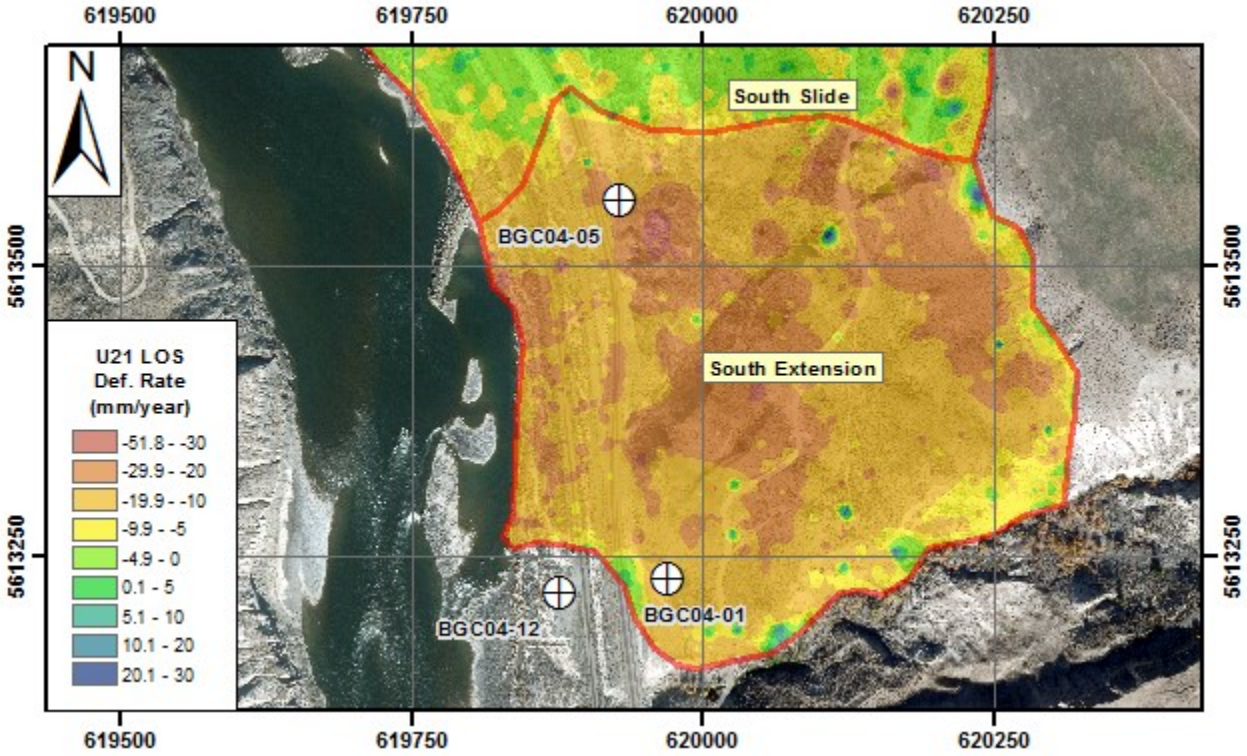

Figure 4-9: South Extension Movement Zone – U21 LOS Deformation Rates

Though multiple geotechnical instruments are located within the footprint of the South Slide, the South Extension contains only three slope inclinometers (SI) with deformation data relevant to this study. Two of these, BGC04-01 and BGC04-12, are located along the southern boundary of the South Extension and remain active to this day. The third (BGC04-05) was located in the north-east portion of the South Extension until its deactivation in 2010 after excessive deformation damaged the casing at depth (Newcomen and Pritchard 2009). All three of these inclinometers have been monitored since their installation in 2004 by BGC Engineering Inc. as part of the construction of a railway siding extension (Roberts et al. 2015).

In the same manner as at the Ripley Slide, the first step in validating PSI results using inclinometer data was to ensure that the two measurements were geometrically equivalent. As inclinometers record only horizontal deformations, equivalence was achieved by projecting the deformation reported by each SI onto the horizontal component of the U21 sensitivity versor. In turn, the measured LOS deformations of nearby U21 CT were reduced to their horizontal components using the known U21 LOS inclination angle of 45°. Note that since the azimuths of the three inclinometers used in this analysis were unavailable to the author it has been assumed that each is oriented in the downslope direction plus or minus any skew angle noted in the literature.

4.2.1. BGC04-01

BGC04-01 is located above a slope cut along the CP right-of-way just within the footprint of the South Extension (Figure 4-10). The most recent data from BGC04-01 available to the author indicates the average horizontal displacement rate at this location from October 29, 2014 to April 7, 2015 was 3.2 mm/year at a depth of 14.5 m (Roberts et al. 2015).

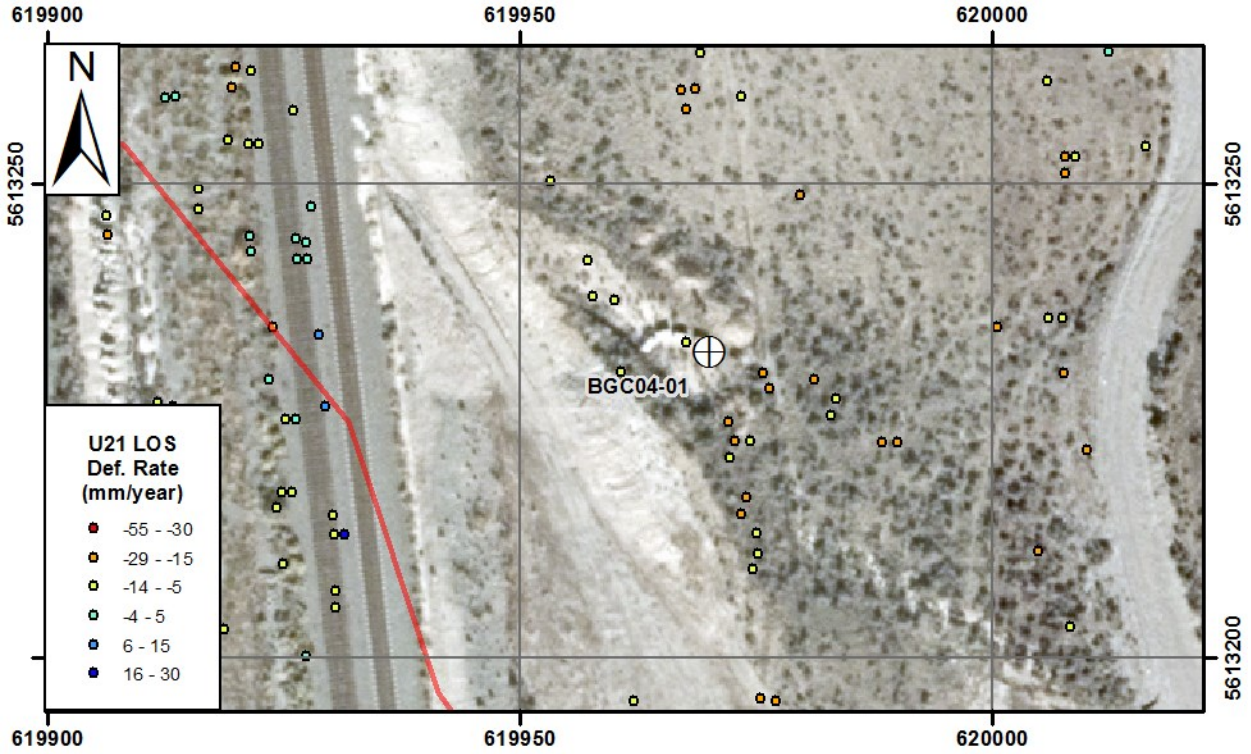

Figure 4-10: U21 CT Surrounding BGC04-01

PSI results from CT within a 25 m radius of BGC04-01 indicate an average annualized horizontal movement rate of 9 mm/year over the observed time interval (Figure 4-11). Though elevated with respect to the SI reported value, the PSI rate is not unexpected, especially when the depth at which the SI rate was measured is considered. Additionally, both movement rates are relatively small when compared to the average and maximum U21 LOS deformation rates observed within the South Extension AOI (-17 and -50 mm/year, respectively).

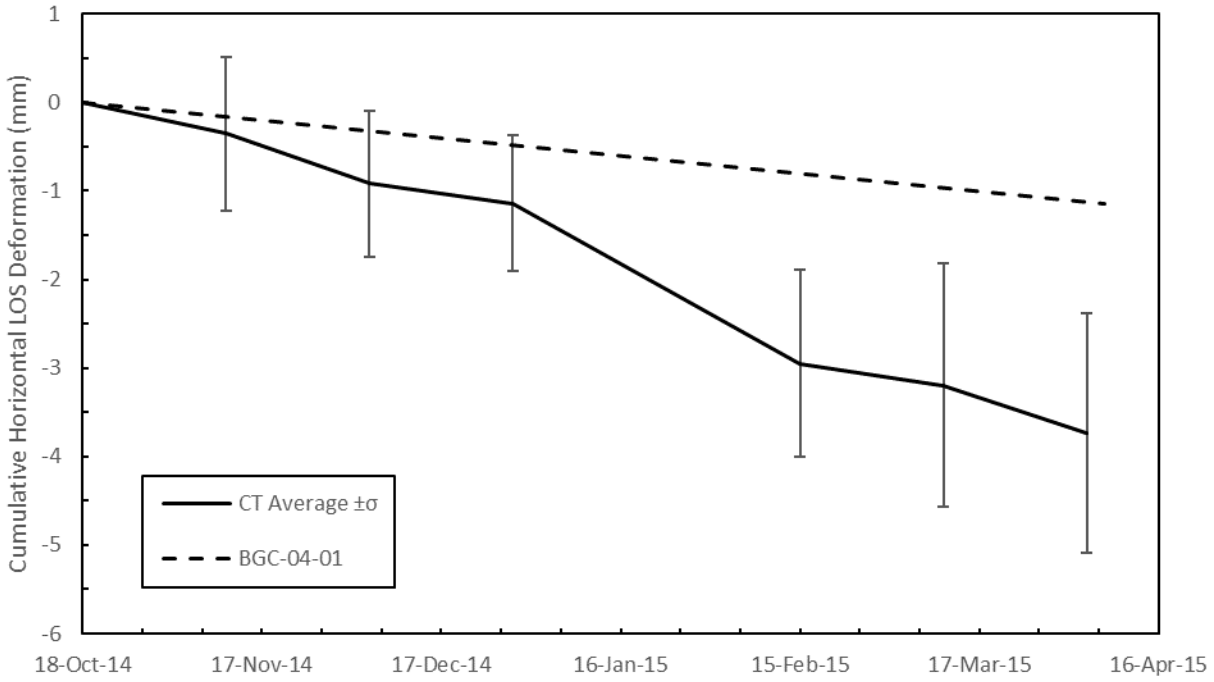

Figure 4-11: Cumulative Horizontal Deformation at BGC04-01 along U21 Azimuth

4.2.2. BGC04-05

Located in the northwest quadrant of the South Extension footprint (Figure 4-12), BGC04-05 was deactivated in 2010 after deformations averaging 16 mm/year caused the inclinometer's casing to fail at a depth of 14.2 m. Other active inclinometers near this instrument indicate that movement rates in the area have not changed substantially since that time. It is not unreasonable then to assume that PSI results should show a movement rate similar to the 16 mm/year last recorded at this location. Evaluating the results from U21 CTs within a 25 m radius of BGC04-05 indicates that this assertion is indeed correct, with consistent horizontal deformations of 15 mm/year on average reported from November 2013 to November 2015.

Figure 4-13 presents the average time-series deformation of these U21 CT, as well as a linear representation of the last reported movement rate at this SI. This figure shows that the measured CT data follows the presumed SI movement closely, with the latter remaining within one standard deviation of the average CT deformation trend.

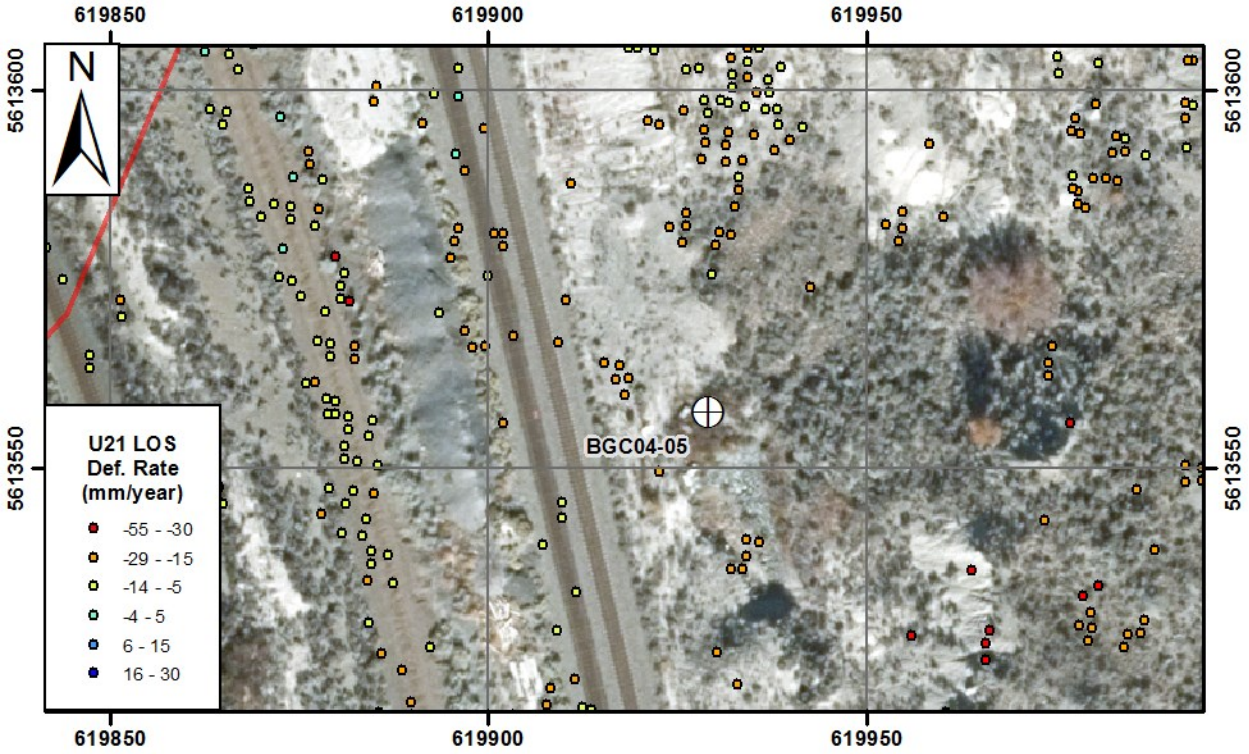

Figure 4-12: U21 CT Surrounding BGC04-05

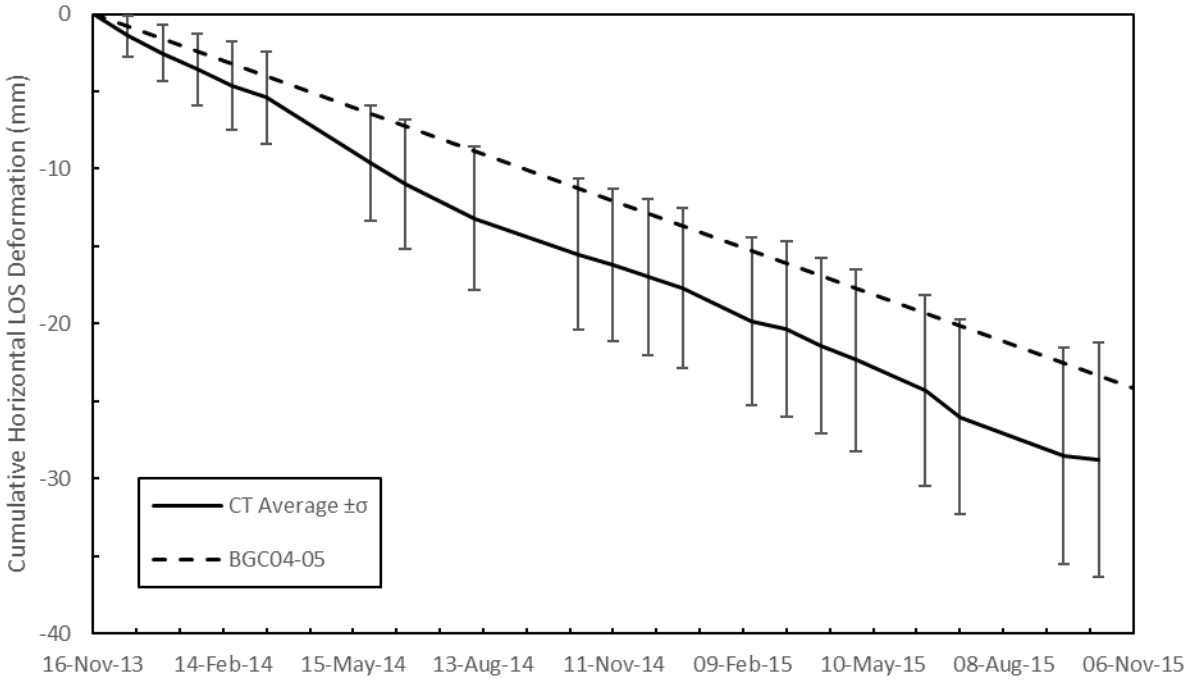

Figure 4-13: Cumulative Horizontal Deformation at BGC04-05 along U21 Azimuth

4.2.3. BGC04-12

The third inclinometer considered for PSI validation at the South Extension, BGC04-12, is located just outside the southern toe of the South Extension movement zone (Figure 4-14).

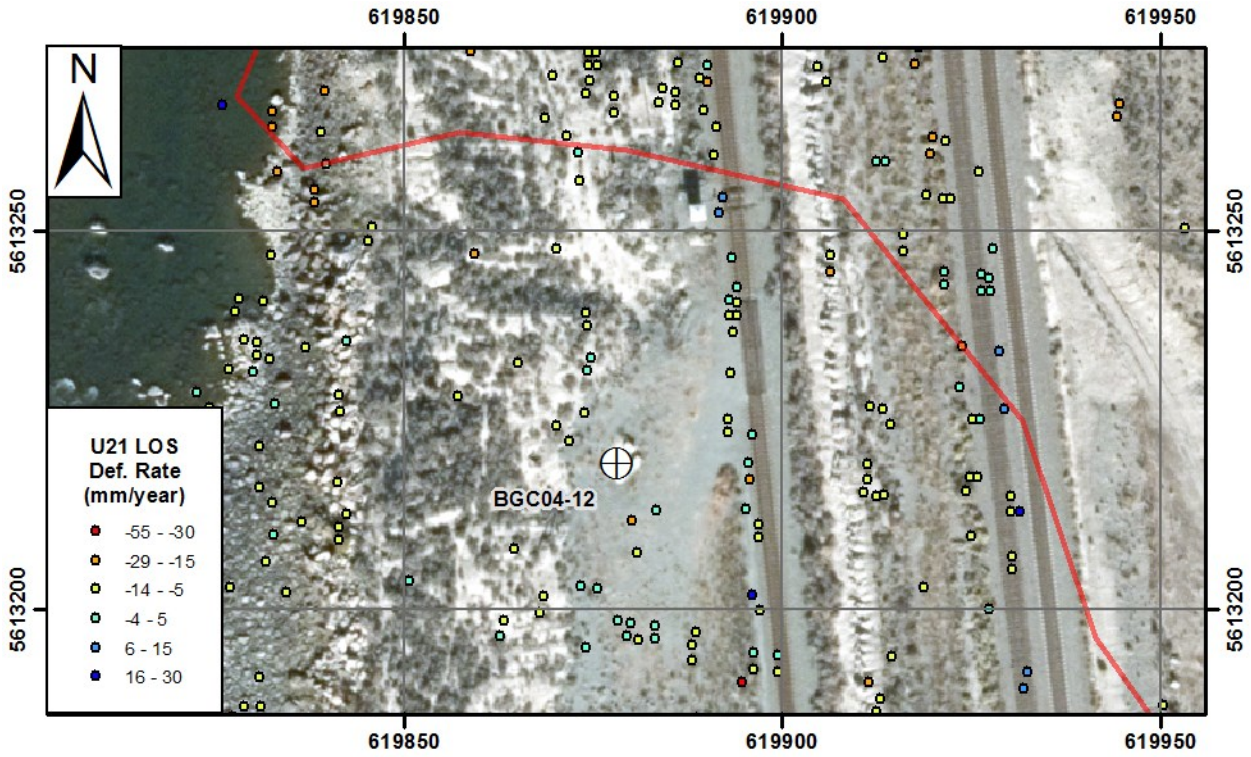

Figure 4-14: U21 CT Surrounding BGC04-12

Recent data from this SI indicated a horizontal movement rate of 3.5 mm/year at a depth of 8.2 m in November 2010 (Roberts et al. 2015). In comparison, U21 CTs within a 25 m radius of this instrument indicated an average horizontal deformation rate of 5 mm/year. Figure 4-15 presents the average time-series deformation of these CT as it compares to a linear representation of the last recorded movement rate at BGC04-12. Once again, the SI reported movement rate consistently falls within one standard deviation of the reported U21 CT deformations, indicating a good match between the SI and PSI data.

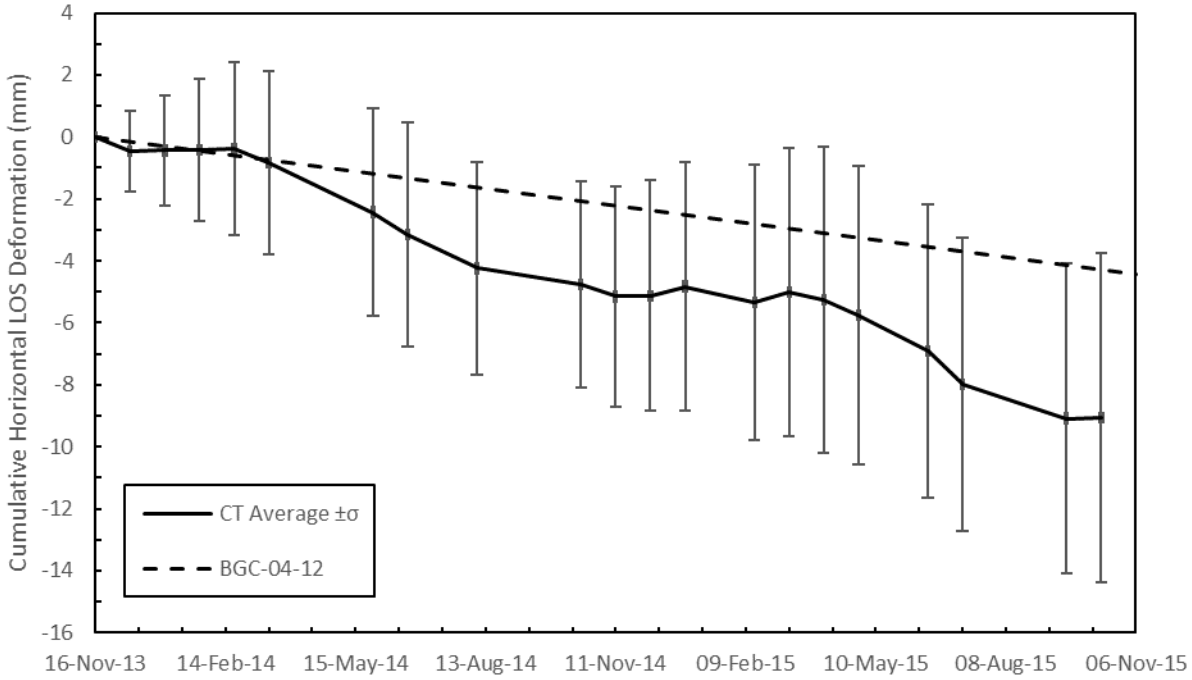

Figure 4-15: Cumulative Horizontal Deformation at BGC04-12 along U21 Azimuth

4.3. Ripley Pump Station

The final location used for PSI validation is a concrete pump station located across the river and just upstream from the Ripley Slide (Figure 4-16). Unlike the Ripley and South slides, this location was chosen due to its anticipated stability over time relative to the surrounding landslides. Positive validation at this location is thus indicated by an absence of long-term deformation in the PSI data.

The U21 dataset was chosen for validation purposes at this location as it contains the greatest number of CT that can be associated with the pump station structure (23 in total). Figure 4-17 presents the time-series deformation of these CT along with the assumed stable condition of the pump station structure. Finally, Figure 4-18 presents the statistical distribution of annualized U21 deformation rates at this location.

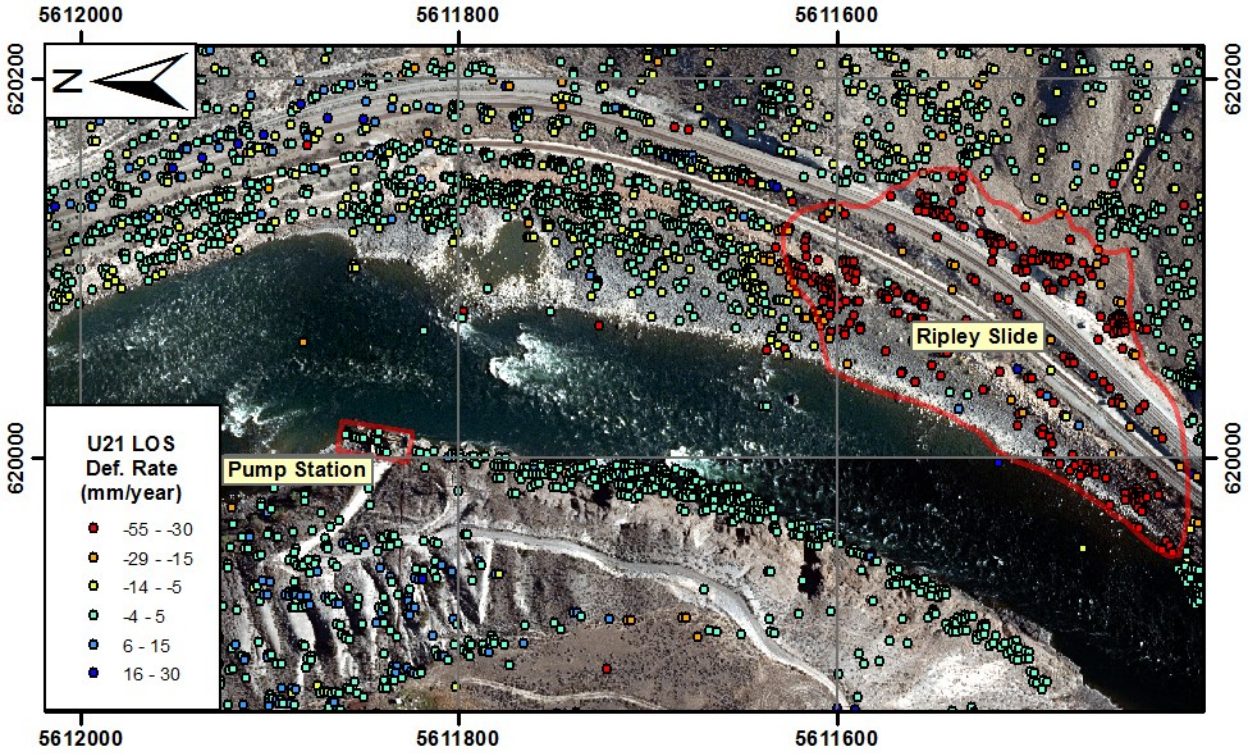

Figure 4-16: Ripley Pump Station

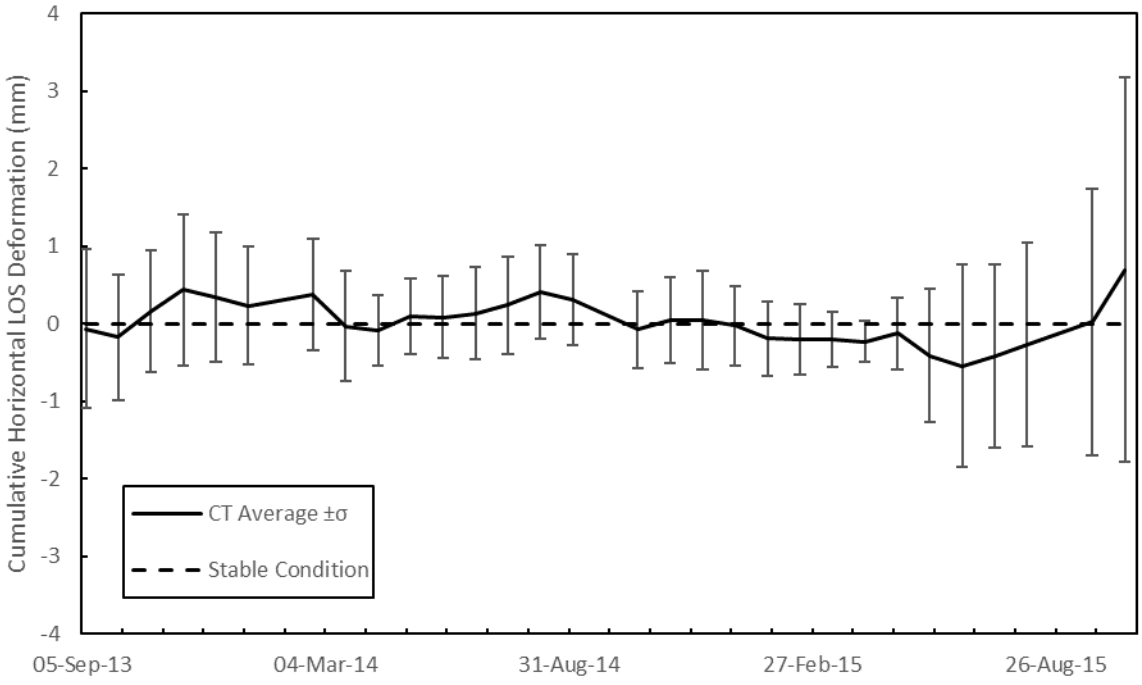

Figure 4-17: Cumulative Deformation of U21 CT Associated with Ripley Pump Station

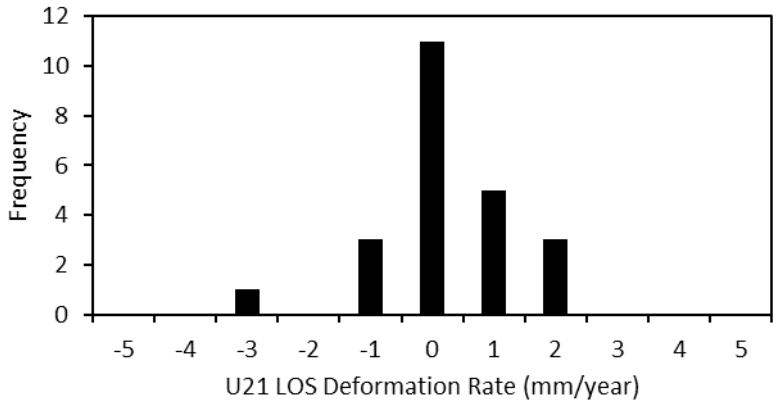

Figure 4-18: Statistical Distribution of Annual Deformation Rates – Ripley Pump Station

As can be seen from the preceding figures, PSI analysis indicates that the pump station is indeed stable over the long term, with no appreciable long term trend in the time-series data. Though there is some variability in the average trend, these variations never exceed ±1 mm from the stable condition. Attributable to signal noise or other forms of measurement error rather than actual deformations, such small variations are to be expected when considering data on a minute scale approaching the minimum sensitivity of the radar system. Note that the increased variability observed in summer 2015 is likely due to construction & maintenance activities at the pump station observed by the author during field visits to the Ripley Slide.

4.4. Summary of PSI Validation

Apart from the unfavorable results at GPS-3, all locations selected for PSI validation showed good agreement between the InSAR and ground-based deformation measurements. In addition, PSI indicated no appreciable ground movement where none was expected, confirming that the processing method does not report false positives. Though only U21 validation results are presented here, similar data validation results can be achieved using the other PSI datasets. Therefore, the Thompson River PSI data is considered to have been successfully validated.

5.0 InSAR Analysis of Landslides along the Thompson River

Extending PSI analysis to the greater study area within the Thompson River corridor has identified six zones of concentrated movement, all of which are within or surrounding historic landslide footprints. Table 5-1 provides a geometric summary of each identified movement zone, as well as the Cartesian components of the slope vector $\overline{U}_{slope}$ associated with each AOI. Aspect direction angles are referenced to true north, while slope angles (or dip angles) reference the horizontal plane. Cartesian vector components follow the right-hand rule, with the positive x-direction corresponding to due east.

Correspondingly, Table 5-2 presents the geometric components of the sensitivity versor ($\overline{U}_{LOS}$) associated with each PSI dataset considered in this analysis. Finally, interpolated movement intensity maps for each active AOI are presented in Appendix A.

Table 5-1: Geometric Summary of Active AOI

Area of Interest (AOI)	Area (m^2)	Aspect Direction (degrees)	Average Slope (degrees)	$\overline{U}_{slope}$ Vector Components		
				x	y	z
Ripley	23,458	298	-13.2	-0.860	0.457	-0.228
South Extension	180,760	235	-17.8	-0.780	-0.546	-0.306
Goddard Toe	19,864	209	-16.9	-0.457	-0.841	-0.290
North Slide Toe	49,171	335	-16.7	-0.405	0.868	-0.288
Barnard	175,328	272	-14.1	-0.969	0.034	-0.244
Red Hill Toe	78,428	85	-21.5	0.927	0.081	-0.367

Table 5-2: Sensitivity Versor Geometry

PSI Dataset	Aspect (degrees)	Elevation (degrees)	$\overline{U}_{LOS}$ Vector Components		
			x	y	z
U5	100	34	0.551	-0.097	0.829
U21	100	45	0.696	-0.123	0.707
F4N	260	44	-0.684	-0.121	0.719

5.1. Ripley Slide

One of the more studied sites in the Thompson Valley, the Ripley Slide is the most densely instrumented and active AOI under consideration in this work. The site is ideally oriented for RADARSat-2 imaging, with the U5 and U21 datasets each capturing 71% and 82% of ground movements, respectively. CT densities are similarly greatest for the west-facing datasets U5 and U21 (1322 and 1505 points/km^2, respectively), while the F4N dataset had a much lower CT density of 68 points/km^2 due to its lower spatial resolution. These data, as well as the average cumulative and annual LOS deformation for the Ripley Slide are summarized in Table 5-3.

The statistical distribution of LOS movement rates for the U5 and U21 dataset at the Ripley Slide are shown in Figure 5-1, while the average time-series deformation of the U21 dataset is shown in Figure 5-2. The U21 movement intensity map for this site is presented Figure 5-3, while maps of the remaining PSI datasets are given in Appendix A.1. These maps indicate ground movement at the Ripley Slide is concentrated within the centre of the sliding mass, with the most rapid deformations occurring upslope from developed railway property.

Table 5-3: PSI Results at the Ripley Slide

Dataset	U5	U21	F4N
CT Density (per km^2)	1322	1505	68
Geometric Scale Factor (S)	-1.4	-1.2	2.7
Percent Capture (P_c)	71%	82%	37%
Average Cumulative LOS Deformation (mm)[1]	-75	-75	96
Average LOS Deformation Rate (mm/year)	-34	-39	21
Standard Deviation of LOS Def. Rate (mm/year)	8	12	11

1. Total deformation as measured relative to the first SAR acquisition of each dataset.

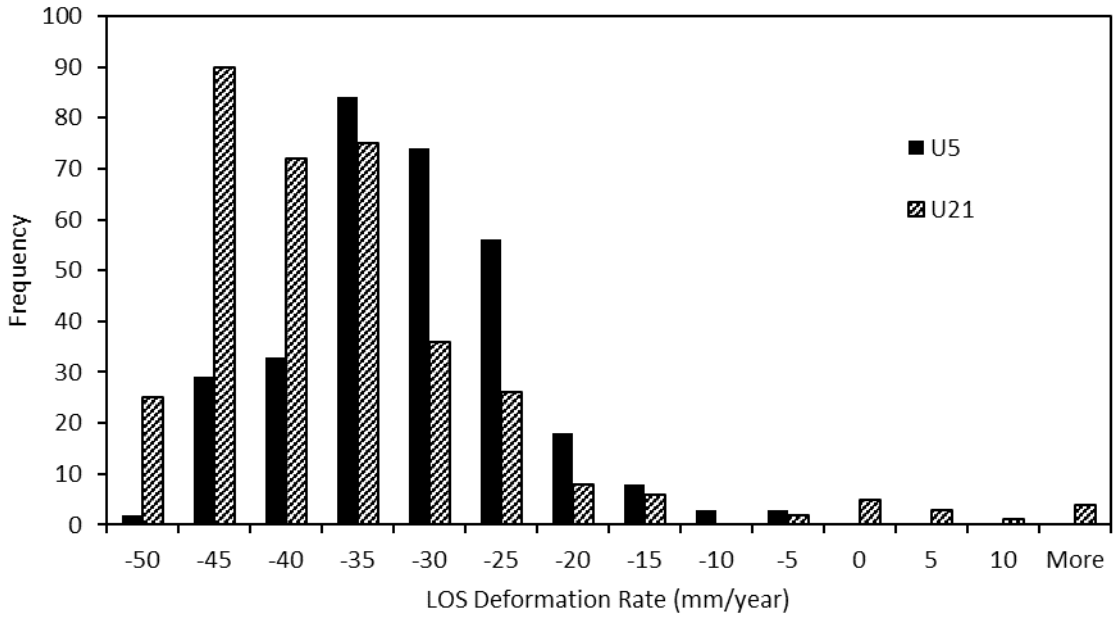

Figure 5-1: Distribution of U5 and U21 LOS Movement Rates - Ripley Slide

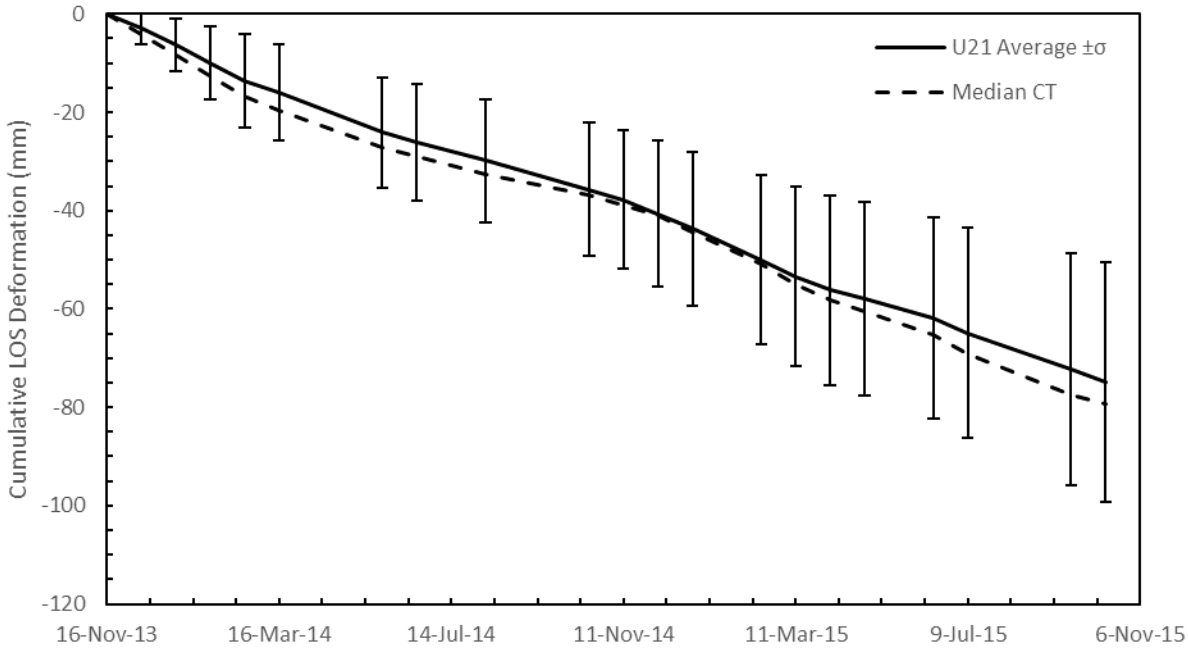

Figure 5-2: Cumulative U21 LOS Deformation - Ripley Slide

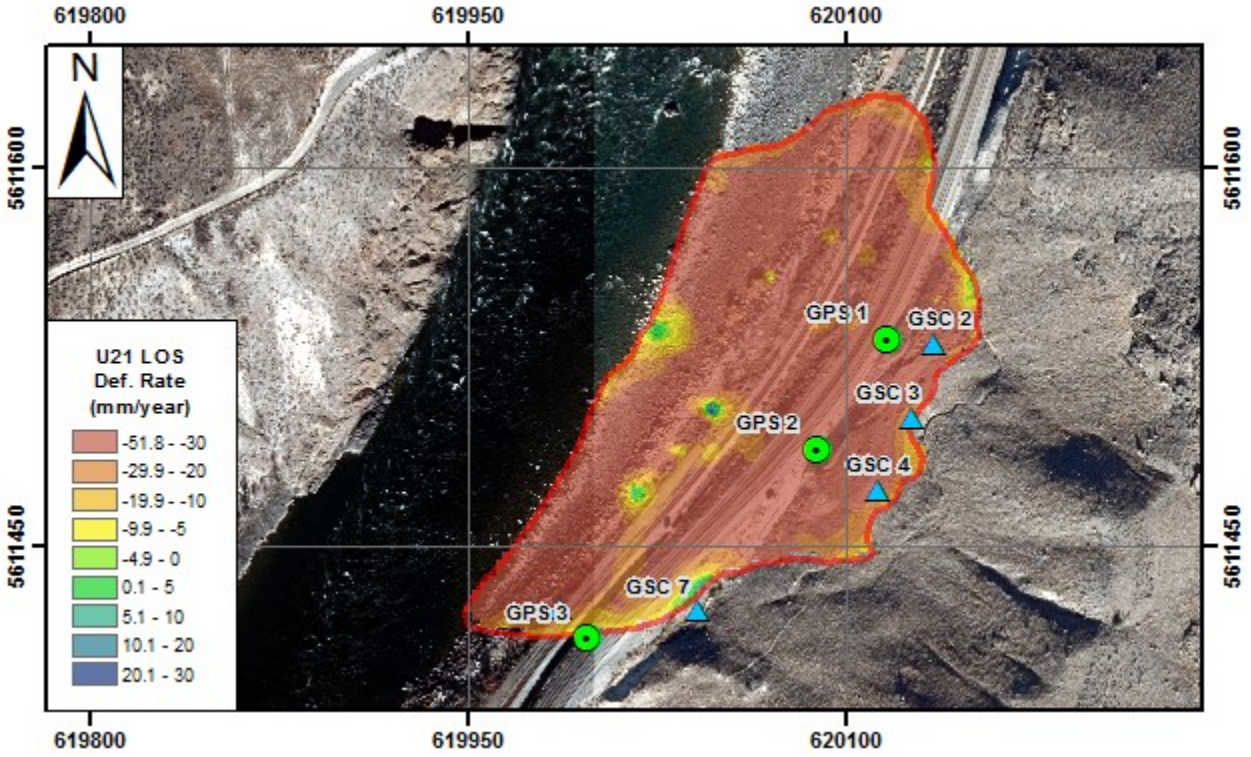

Figure 5-3: U21 Movement Intensity Map - Ripley Slide

Though subdued in Figure 5-2, individual CT at the Ripley slide show a clear pattern of seasonal variation, with elevated deformation over the winter months (November through March) and subdued movement in the summer and fall. This seasonal variation, which has been associated by others with pore water pressure fluctuations induced by changes in water level in the Thompson River (Schafer 2016), induces a non-linear movement pattern at the Ripley slide. The consequence of this is that annualized deformation rates calculated using an assumed linear model may not capture the range of deformation rates possible at the Ripley Slide. However, as a means of comparing the activity of multiple sites within a given area they remain a useful metric.

Considering all PSI datasets together using the methods outlined in Section 3.2.3.3, the overall average and maximum downslope deformation rates at the Ripley Slide have been estimated as 49 mm/year and 77 mm/year, respectively. These rates, especially the maximum estimated rate,

are consistent with data published by others (Hendry et al. 2015, Schafer et al. 2015) taken from slope inclinometers, shape accel arrays (SAA), and GPS monuments.

5.2. South Slide

The South Extension of the South Slide is the largest active movement zone detected within the study area, encompassing approximately 181,000 m^2. Compared to the Ripley Slide, the South Extension not as well oriented for RADARSat-2 imaging, with the U5 and U21 datasets each capturing 63% and 69% of ground movements, respectively. CT densities at the South Extension were greatest for the west facing U5 and U21 datasets (1130 and 1304 points/km^2, respectively), while the F4N CT density was 185 points/km^2. A summary of this information, as well as the average cumulative and annual LOS deformation within the South Extension is presented in Table 5-4. The statistical distribution of LOS movement rates for the U5 and U21 dataset at the South Extension are shown in Figure 5-4, while the average time-series deformation of the U21 dataset is shown in Figure 5-5. The U5 movement intensity map for this site is presented in Figure 5-6, while maps of the remaining PSI datasets are given in Appendix A.2. These maps indicate that ground movement at the South Extension is concentrated within two 75 m bands traversing the AOI in a direction parallel to the river. The smaller of the two bands is located just below the upper scarp of the movement zone, while the second lies near the centre of the AOI immediately upslope from developed railway property.

Table 5-4: PSI Results within the South Slide Extension

Dataset	U5	U21	F4N
CT Density (points per km^2)	1130	1304	185
Geometric Scale Factor (*S*)	-1.6	-1.4	2.6
Percent Capture (P_c)	63%	69%	38%
Average Cumulative LOS Deformation (mm)[1]	-34	-32	52
Average LOS Deformation Rate (mm/year)	-16	-17	12
Standard Deviation of LOS Def. Rate (mm/year)	7	8	7

1. Total deformation measured relative to the first SAR acquisition for each dataset.

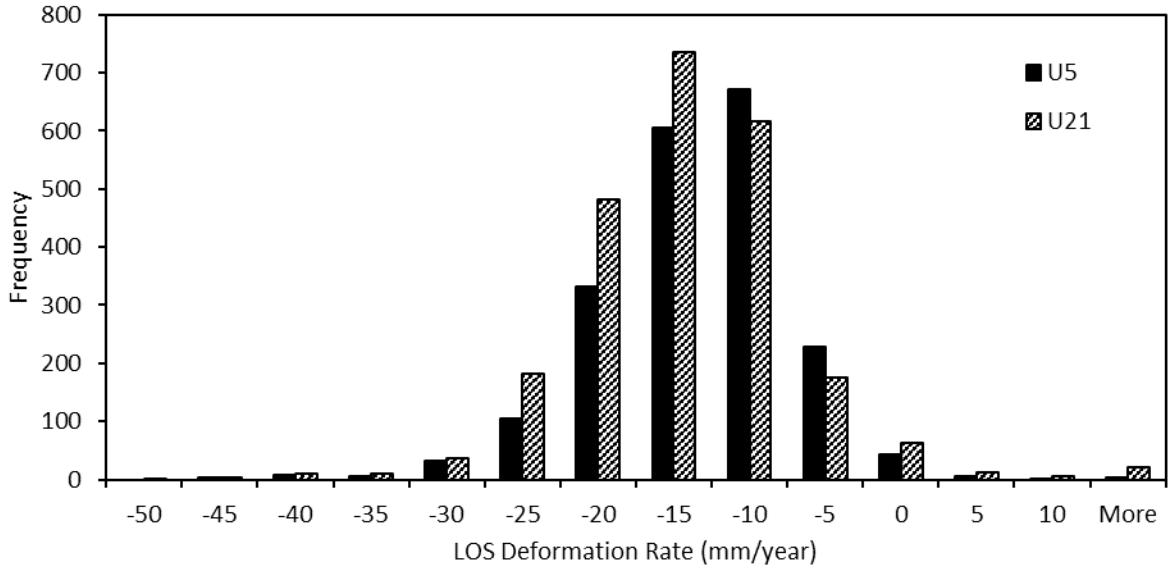

Figure 5-4: Distribution of U5 and U21 LOS Movement Rates - South Extension

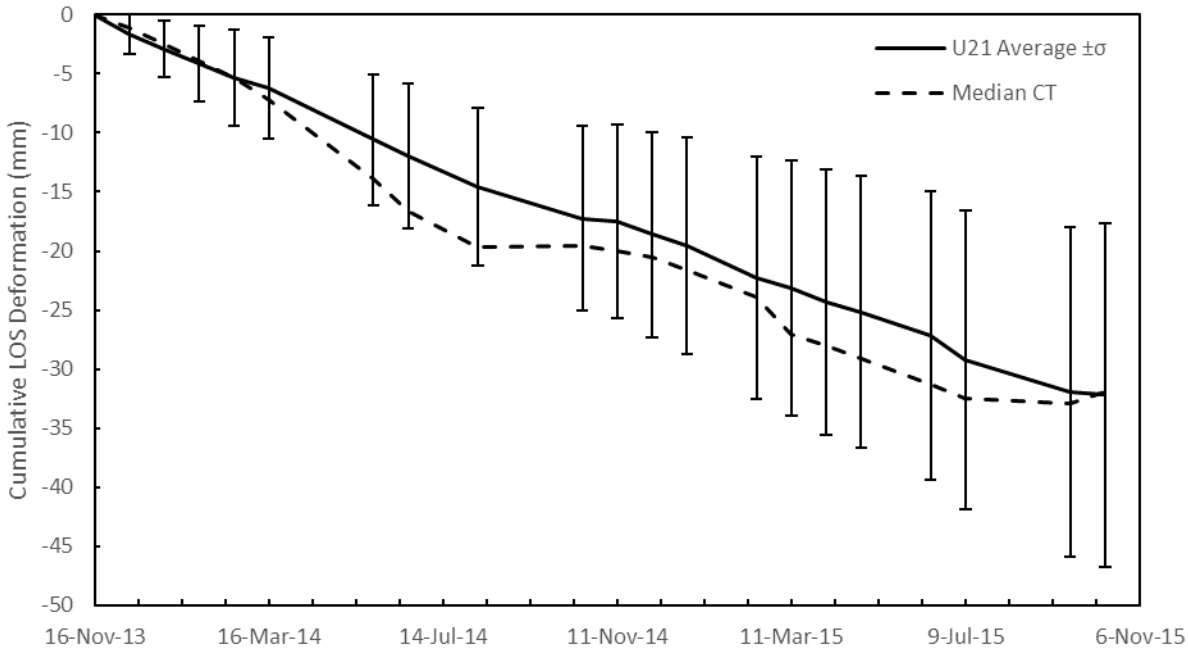

Figure 5-5: Cumulative U21 LOS Deformation - South Extension

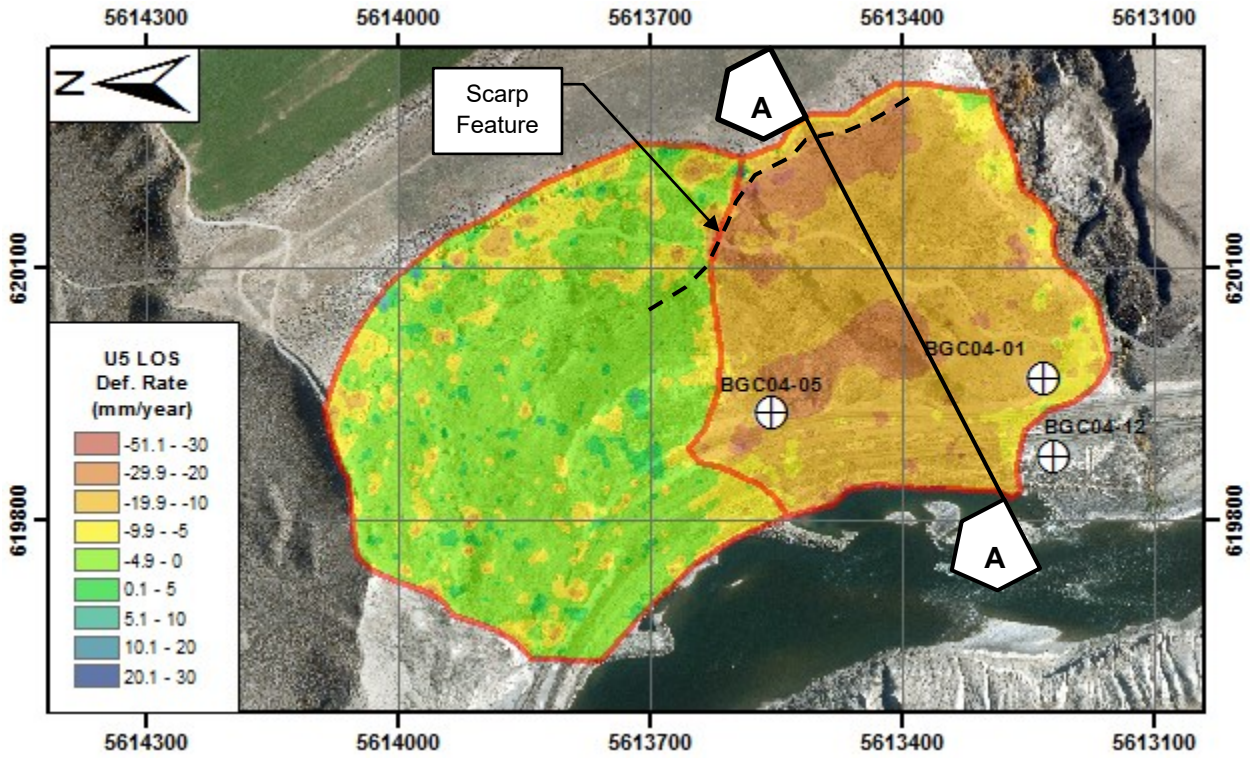

Figure 5-6: U5 Movement Intensity Map - South Slide

Unlike the Ripley Slide, the average time-series data at the South Extension shows very little seasonal variability in ground deformation intensity. Deformations at the AOI tend to be relatively constant throughout the year if only the average trend is considered. However, looking at individual CTs reveals that there are some locations which do in fact express seasonal variability, such as the time series for the median CT shown in Figure 5-5. These CT show a near absence of activity during the summer and early winter months while the most active deformation is observed in the late winter or early spring.

A ground-based investigation of the South Extension was carried out by the author in October, 2015 as part of an effort to locate potential surface expressions of the deformation identified from PSI analysis. Though this investigation failed to locate any obvious surficial features, a later analysis of high-resolution LiDAR and aerial imagery did identify a potentially active scarp along the boundary between the South Slide and South Extension AOI (Figure 5-6). This feature

corresponds well with the upper limits of the active South Extension movement zone as delineated by the PSI movement intensity maps. Section A-A further illustrates the location of this feature by showing the steep reduction in LOS deformation rate just below the terrace crest (Figure 5-7).

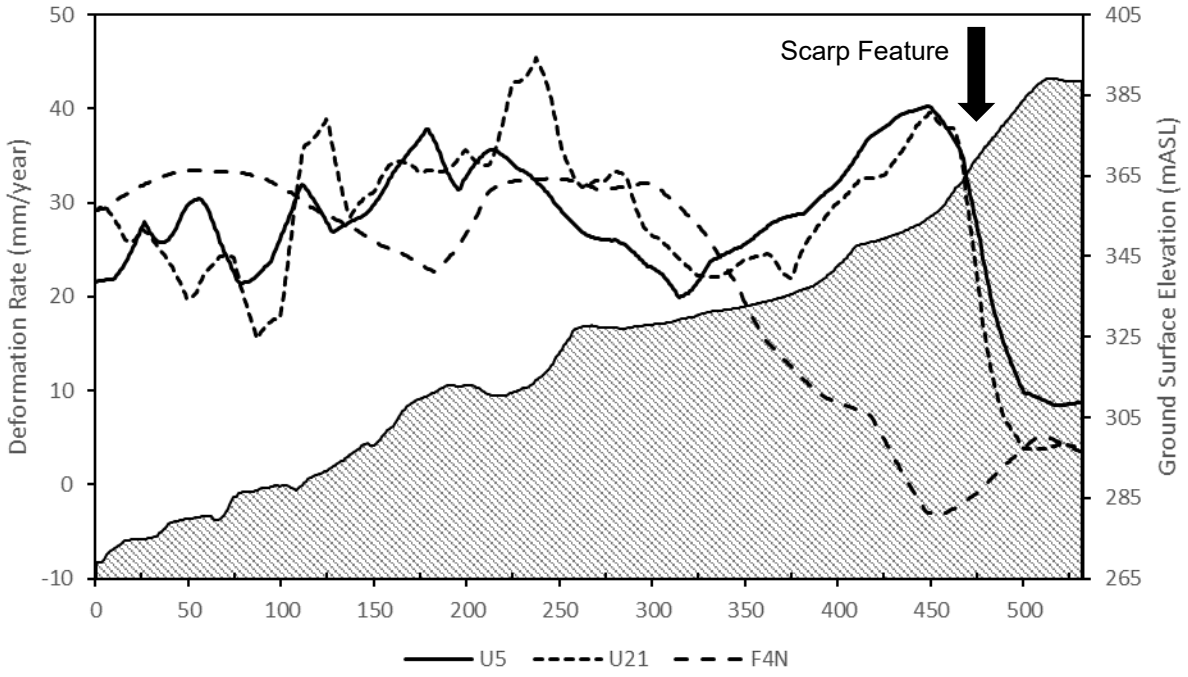

Figure 5-7: Section A-A - South Extension AOI with LOS Deformation Rate Overlay

Considering all PSI datasets at the South Extension together, the average and maximum downslope deformation rates at the site have been estimated as 21 and 60 mm/year, respectively.

5.3. Red Hill Slide

Situated on the west bank of the Thompson River, the Red Hill Slide is a historic failure whose footprint contains a smaller area of active deformation, referred to in this work as the Red Hill Toe. As this zone is oriented approximately due east (85° azimuth), the U5 and U21 coverage is significantly lower than at other sites (20% and 37%, respectively). Though the F4N coverage is much better (91%), the F4N CT density remained low within the AOI (26 points per km^2). Despite their reduced precision at this site, PSI analysis still provides valuable insight into the nature of ground movements within this otherwise unstudied site.

Table 5-5 presents a summary of PSI data from the Red Hill Toe, while the average F4N time-series deformation is shown in Figure 5-8. The U21 movement intensity map for this site is presented in Figure 5-9, while maps of the remaining PSI datasets are given in Appendix A.3.

Table 5-5: PSI Results at the Red Hill Slide Toe

Dataset	U5	U21	F4N
CT Density (points per km^2)	708	1109	26
Geometric Scale Factor (*S*)	5.1	2.7	-1.1
Percent Capture (P_c)	20%	38%	91%
Average Cumulative LOS Deformation (mm)[1]	26	38	-104
Average LOS Deformation Rate (mm/year)	12	19	-23
Standard Deviation of LOS Def. Rate (mm/year)	12	14	10

1. Total deformation measured relative to the first SAR acquisition for each dataset.

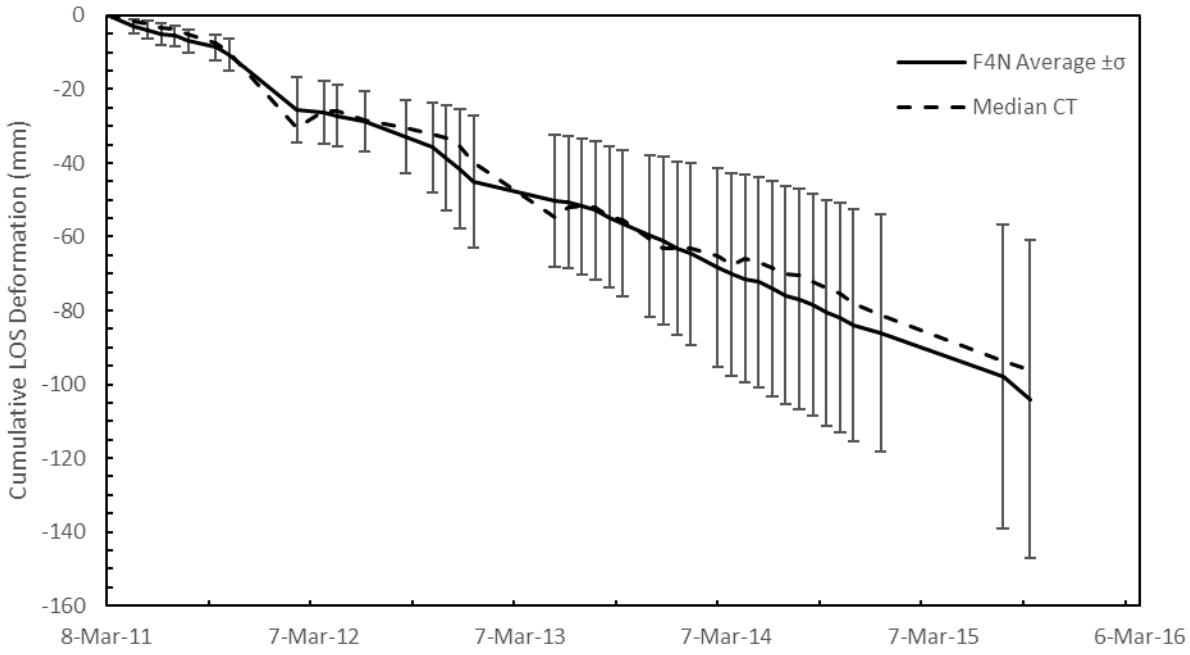

Figure 5-8: Cumulative F4N LOS Deformation - Red Hill Toe

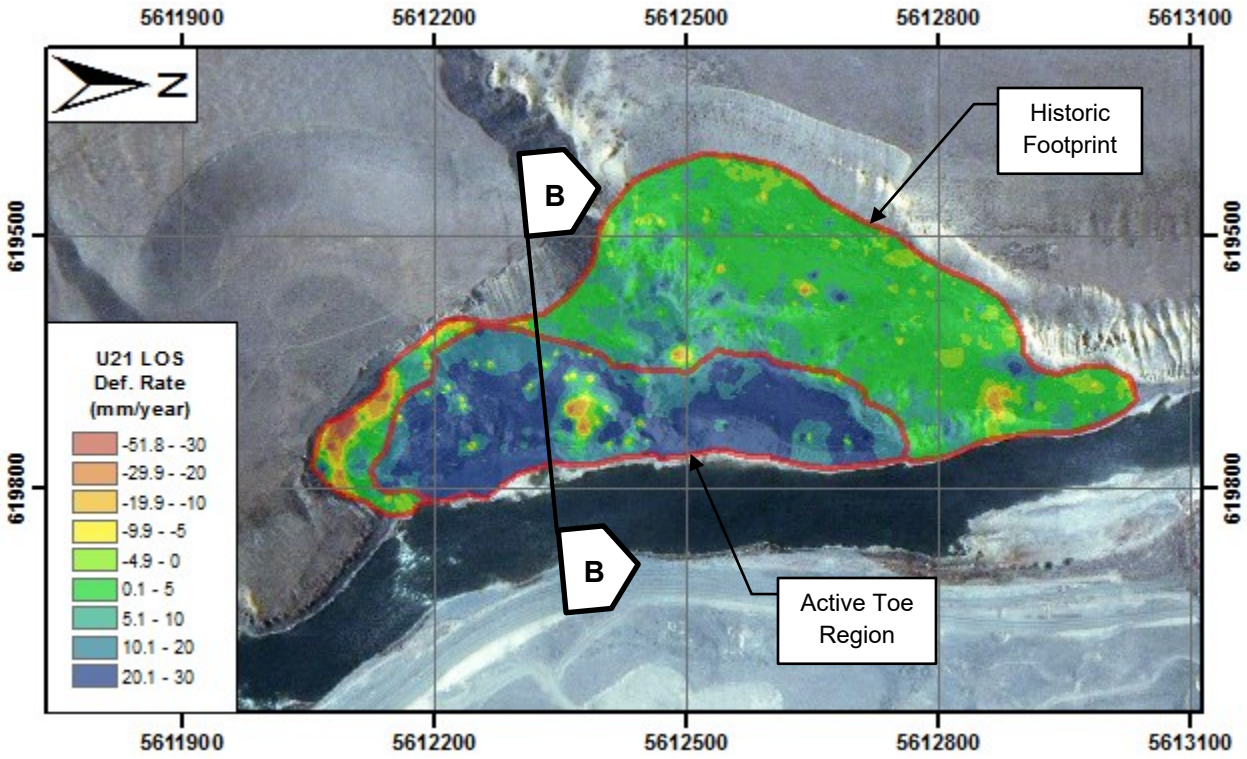

Figure 5-9: U21 Movement Intensity Map - Red Hill Slide

As illustrated in the time-series data presented above, ground movements within the Red Hill Toe can be strongly affected by a seasonal variation. Periods of increased slope movement are often seen in the late fall and winter months, while movements become relatively subdued from mid-spring through to summer. However, this seasonal variation was not always observed in the PSI results. This absence of seasonality is most evident in the time-series data from June 2013 through July 2015, where the F4N LOS deformation rate was a relatively constant 23 mm/year. Given the similarity of this seasonal variability to that observed at the Ripley Slide, as well as the proximity of the two sites, it is probable that a similar mechanism of pore water pressure fluctuations associated with changes in river flow volume is contributing to instability observed at the Red Hill Slide.

Further evidence of the river's influence on movements at this location is the extensive erosion and sloughing of the riverbank observed during a field visit in October 2015 (Figure 5-10). Material from the toe of the slide appears as if it has been actively eroded by the river during periods of high flow. Whether this erosive activity is a contributing factor or consequence of the instability observed at the site is a matter for future study.

Figure 5-10: Active Erosion and Sloughing of the Red Hill Toe (looking southwest)

A sectional view of the Red Hill Slide provides a clearer look at the elevated movement zone located at the toe of the slope. Section B-B presents the elevation profile of the site as well as the absolute annual deformation rate profile of each PSI dataset along the section (Figure 5-11). While the F4N trend suggests wider instability at this location, the U5 an U21 profiles together show increasing deformation toward the toe of the slope which appears consistent with movement induced by material erosion at the landslide toe.

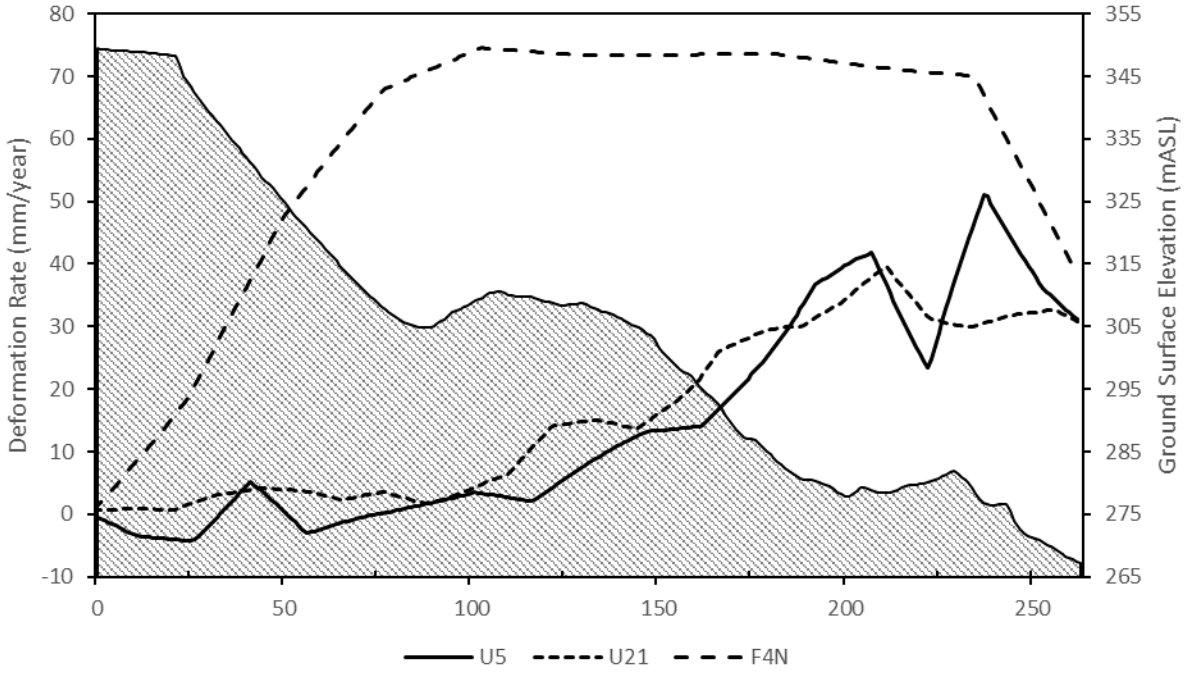

Figure 5-11: Section B-B - Red Hill AOI with LOS Deformation Rate Overlay

Taking all three PSI datasets together, the average and maximum estimated downslope deformation rates at this location have been calculated as 37 and 89 mm/year, respectively. These rates suggest that the Red Hill Toe is nearly as active as the Ripley Slide, which is located just downstream on the opposite bank of the Thompson River.

5.4. Barnard Slide

Opposite the Red Hill Slide on an upper terrace of the Thompson Valley is the Barnard Slide. Movements at this location are very slow, with only minor deformations detected in each PSI dataset. With an orientation similar to those of the Ripley and South slides, the Barnard Slide has good coverage from both the U5 and U21 datasets (74% and 85%, respectively). CT density is reduced compared to other nearby AOI, perhaps due to the increased vegetative cover on the upper terrace. However, it is not so low as to hinder PSI analysis at this AOI.

A summary of PSI data from the Barnard Slide is given in Table 5-6, while the statistical distribution of LOS movement rates is presented in Figure 5-12. The average cumulative U21 LOS deformation is shown in Figure 5-13. The U5 movement intensity map for this site is presented in Figure 5-14, while maps of the remaining PSI datasets are given in Appendix A.4.

Table 5-6: PSI Results at the Barnard Slide

Dataset	U5	U21	F4N
CT Density (points per km^2)	549	703	135
Geometric Scale Factor (*S*)	-1.4	-1.2	2.1
Percent Capture (P_c)	74%	85%	48%
Average Cumulative LOS Deformation (mm)[1]	-18	-19	4
Average LOS Deformation Rate (mm/year)	-9	-11	2
Standard Deviation of LOS Def. Rate (mm/year)	5	8	3

1. Total deformation measured relative to the first SAR acquisition for each dataset.

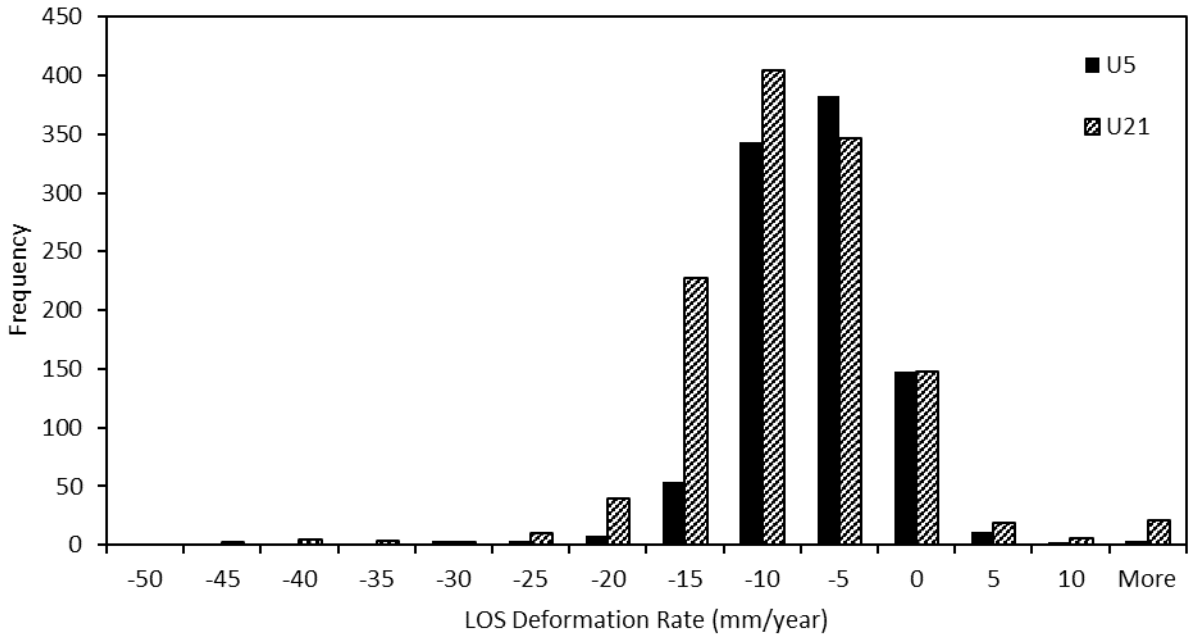

Figure 5-12: Distribution of U5 and U21 LOS Movement Rates - Barnard Slide

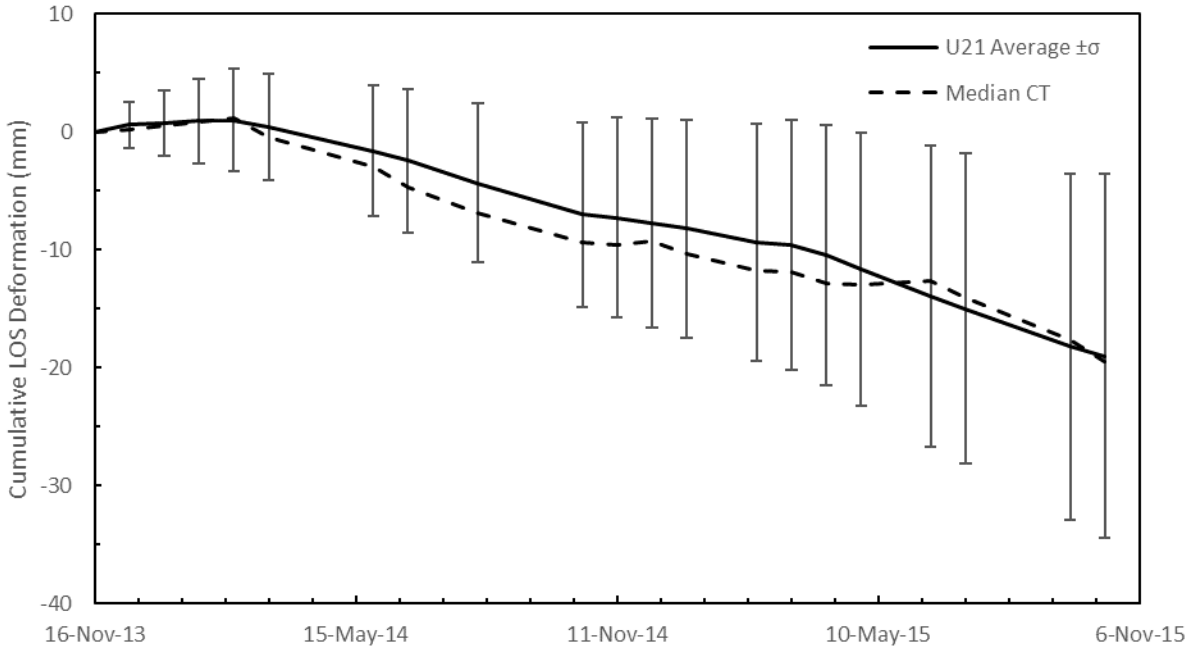

Figure 5-13: Cumulative U21 LOS Deformation – Barnard Slide

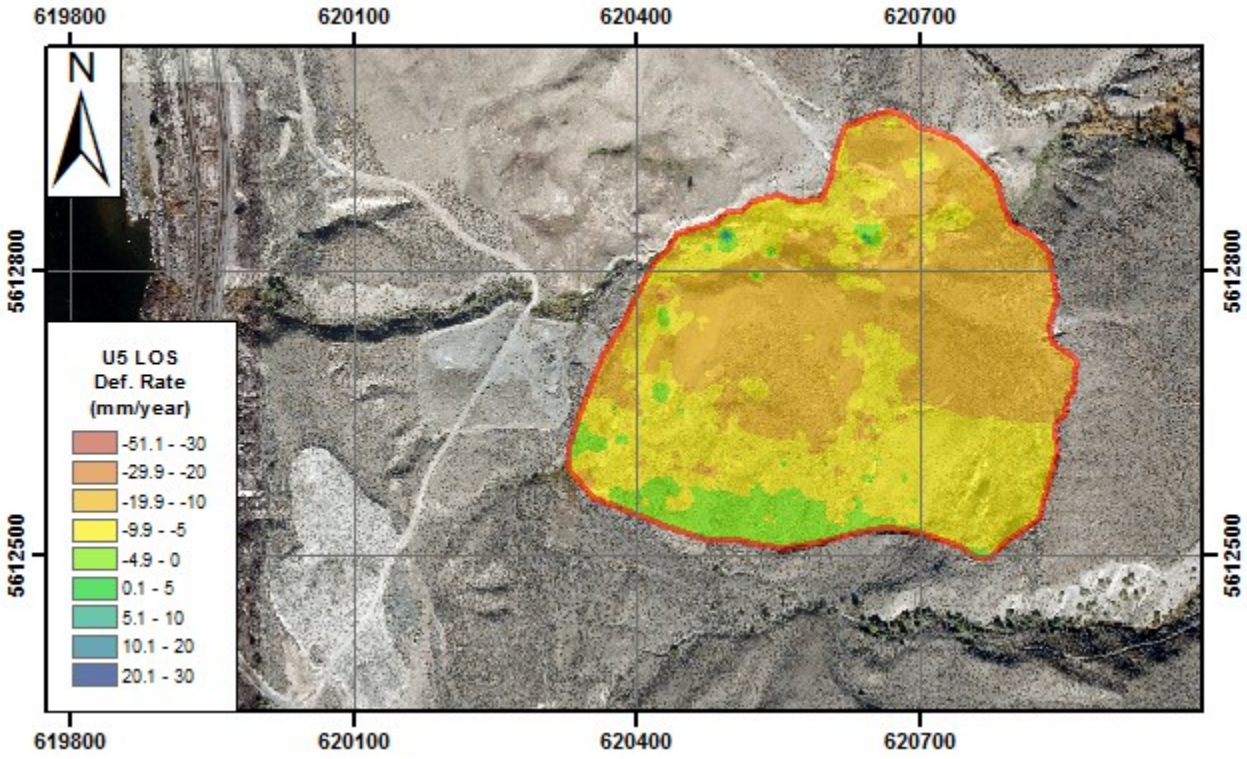

Figure 5-14: U5 Movement Intensity Map - Barnard Slide

Intriguingly, PSI results for the Barnard Slide indicate a seasonal movement pattern that is opposite to those observed at the Ripley and Red Hill sites. Whereas the latter two sites exhibit elevated deformations during the fall and winter months, the Barnard Slide is most active from the spring to early fall. This suggests that the mechanism influencing seasonal behavior at the Barnard Slide is separate from that which is controlling stability at the Ripley and Red Hill slides.

Scaling and combining the results from all three PSI datasets at the Barnard Slide gives average and maximum downslope deformation rates of 10 and 50 mm/year, respectively.

5.5. North and Goddard Slides

Two large and historically active landslides within the study area are the North and Goddard slides. These sites have each experienced high-volume, rapid failures in the past, the most recent of which was a rapid reactivation of the Goddard slide in 1982 (Tappenden 2014). Despite the tumultuous history of both sites, PSI results indicate that very little movement is occurring at these locations today, with active deformations limited to riverbank instability and toe erosion.

5.5.1. North Slide

The largest historic landslide footprint within the study area, the North Slide, is located just upstream from the South Slide. Though its footprint is adequately captured by the west-facing U5 and U21 datasets, PSI coverage of the actively deforming toe is relatively poor due to its north-west orientation. CT densities within the toe are correspondingly low, with the U5 and U21 densities much lower than those obtained at the Ripley Slide and South Extension.

Table 5-7 presents a summary of PSI data from the North Slide toe, while Figure 5-15 presents the cumulative U21 LOS deformation over time within the same area. The U21 movement intensity map for this site is presented in Figure 5-16, while maps of the remaining PSI datasets are given in Appendix A.5.

Table 5-7: PSI Results at the North Slide Toe

Dataset	U5	U21	F4N
CT Density (points per km^2)	594	492	65
Geometric Scale Factor (*S*)	-1.8	-1.7	-28.8
Percent Capture (P_c)	55%	59%	3%
Average Cumulative LOS Deformation (mm)[1]	-24	-27	-15
Average LOS Deformation Rate (mm/year)	-11	-14	-4
Standard Deviation of LOS Def. Rate (mm/year)	10	13	5

1. Total deformation measured relative to the first SAR acquisition for each dataset.

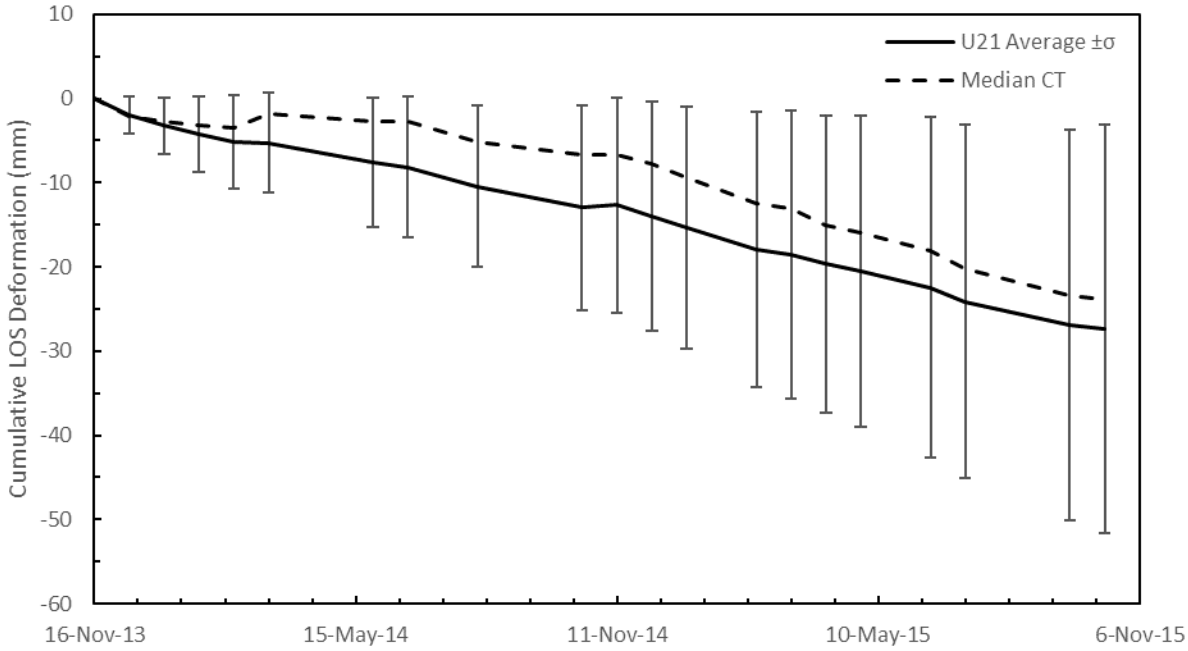

Figure 5-15: Cumulative U21 LOS Deformation – North Slide Toe

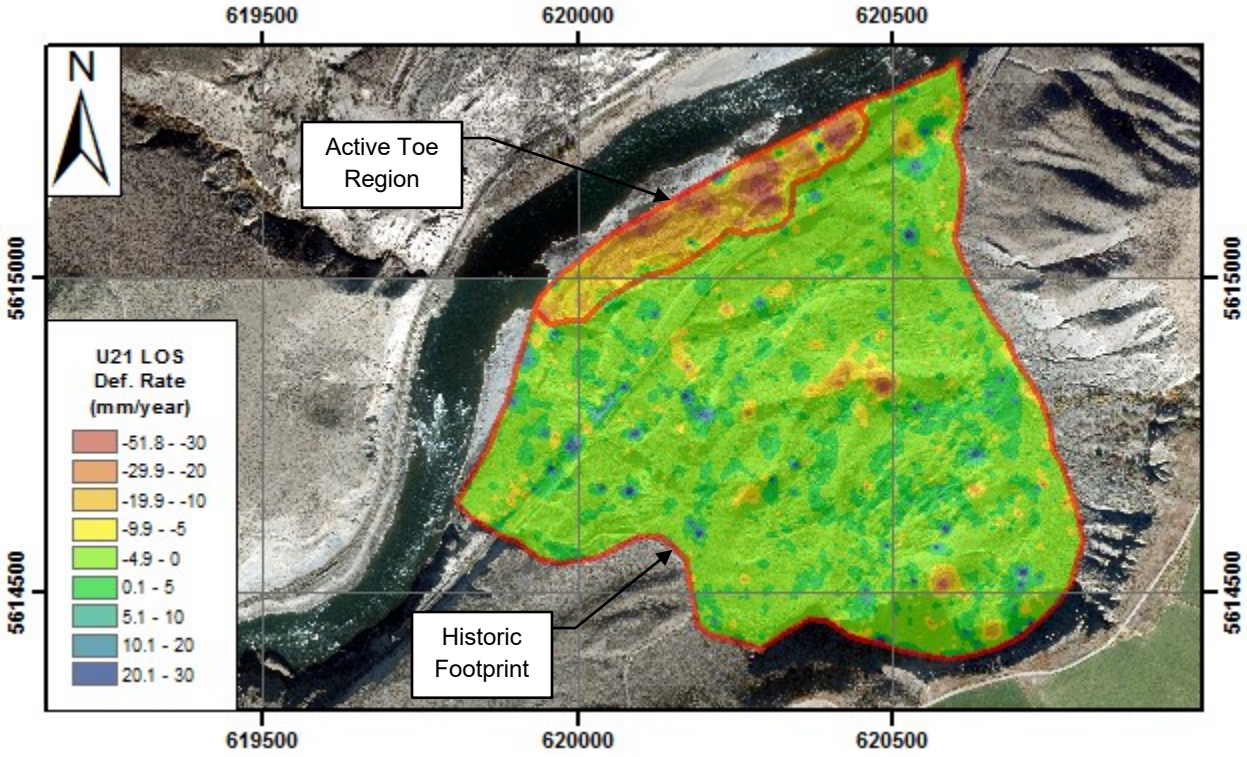

Figure 5-16: U21 Movement Intensity Map - North Slide

A zone of concentrated movement located at the toe of the North Slide is visible in all three movement intensity maps, while the remainder of the historic slide is shown as relatively stable. Though small pockets of displacement can be seen within the historic footprint, these have been interpreted to represent localized sloughing of historic landslide debris as they erode. The toe instability appears to encroach upon developed railway property, which corresponds to reports of increased rail maintenance requirements over this portion of track as compared to other sections.

Combining the PSI results from all three datasets within the toe of the North Slide yields average and maximum annual downslope deformation rates of 25 and 81 mm/year, respectively.

5.5.2. Goddard Slide

Due to its location at the northern limit of the study area and its unfavorable south-west orientation, PSI coverage at the Goddard Slide is notably poor. The U5 and U21 datasets capture only 41% and 42% of ground movement, respectively, while the F4N dataset does not cover the area at all.

Correspondingly, CT densities within the Goddard Slide footprint are low, with the U5 and U21 datasets each containing less than 550 points per km^2.

Table 5-8 presents a summary of PSI data from the toe of the Goddard Slide, while Figure 5-17 presents the average cumulative U21 LOS deformation of the same area. The U21 movement intensity map for this site is presented in Figure 5-18, while maps of the remaining PSI datasets are given in Appendix A.6.

Table 5-8: PSI Results at the Goddard Slide Toe

Dataset	U5	U21	F4N[2]
CT Density (points per km^2)	539	493	N/A
Geometric Scale Factor (*S*)	-2.4	-2.4	N/A
Percent Capture (P_c)	41%	42%	N/A
Average Cumulative LOS Deformation (mm)[1]	-25	-28	N/A
Average LOS Deformation Rate (mm/year)	-12	-14	N/A
Standard Deviation of LOS Def. Rate (mm/year)	10	12	N/A

1. Total deformation measured relative to the first SAR acquisition for each dataset.
2. The Goddard Toe contains no CT from the F4N dataset.

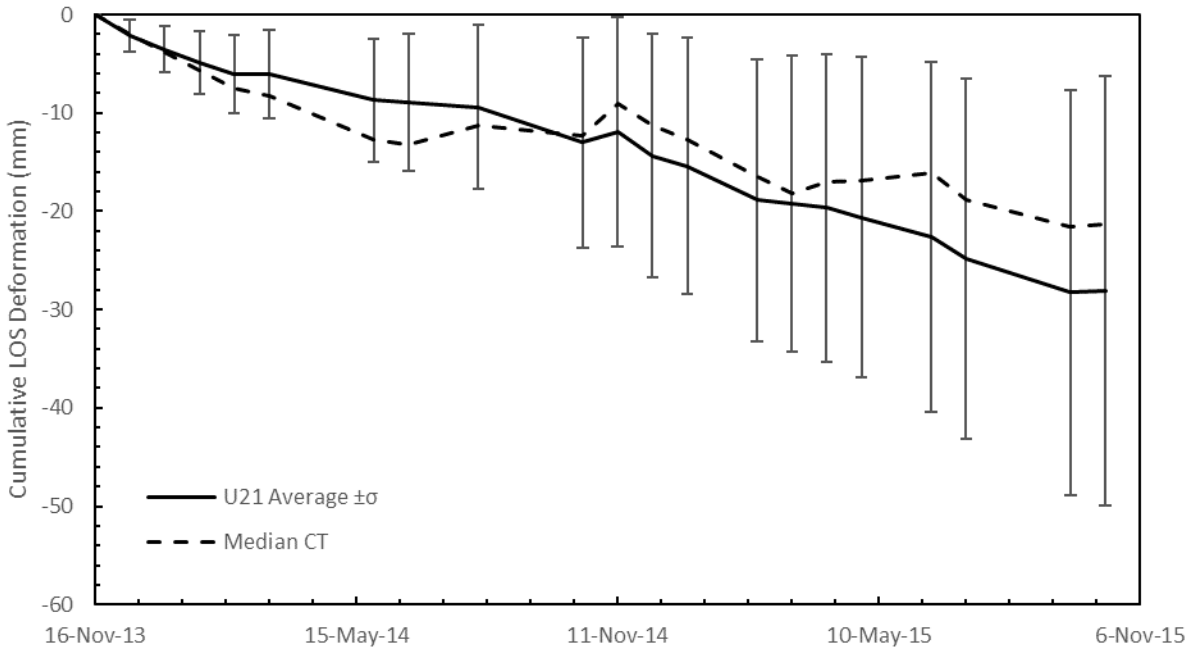

Figure 5-17: Cumulative U21 LOS Deformation – Goddard Slide Toe

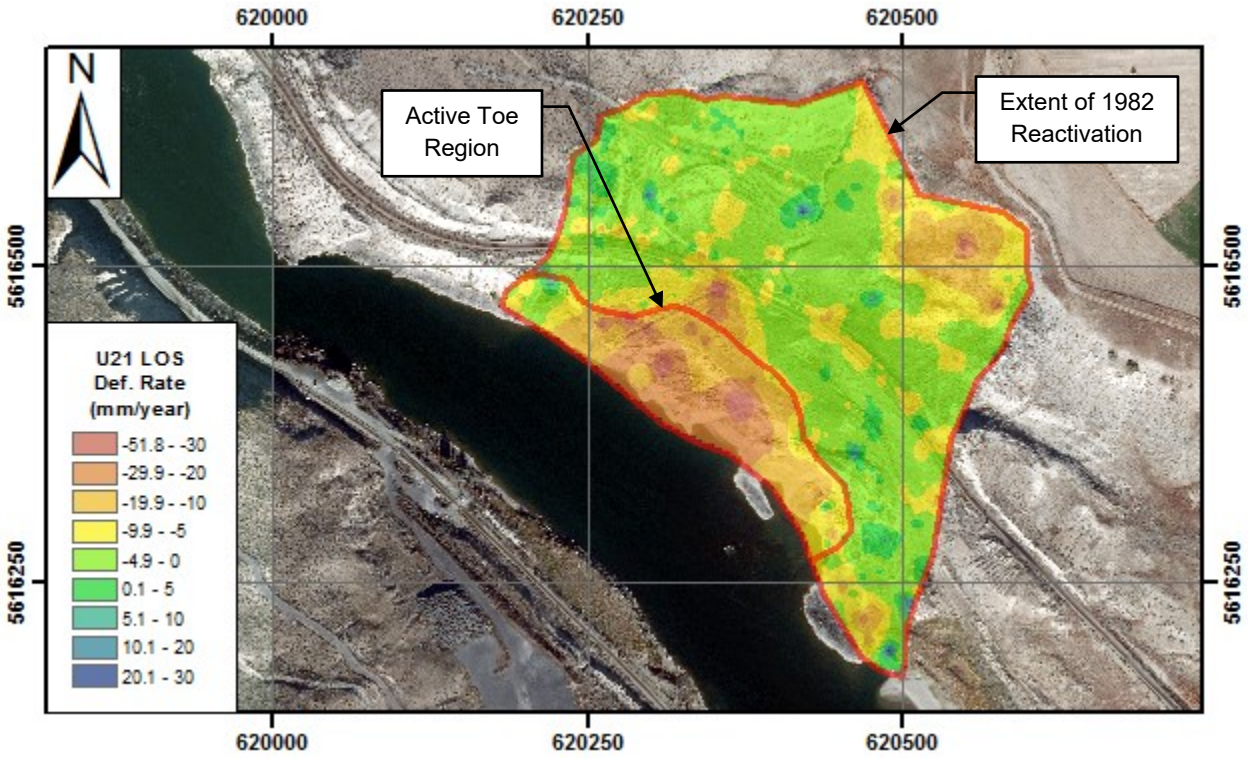

Figure 5-18: U21 Movement Intensity Map - Goddard Slide

In a manner similar to that observed at the North Slide, active deformation at the Goddard Slide is limited to a concentrated zone located at the toe of the slope. Smaller pockets of isolated deformation are visible at higher elevations within the historic slide footprint, however these likely represent localized sloughing or erosion of the upper slopes. Time series data from this location suggests there may be a weak seasonal variation at this site, with observed movement rates being most elevated from November through February. In terms of downslope deformation, the average and maximum deformation rate at this location have been estimated as 31 and 120 mm/year, respectively.

5.6. Summary

In total, PSI analysis in the Thompson River Valley has identified six AOI within the study area that contain zones of active deformation. Most of these sites exhibit seasonal deformation patterns which suggest the factors found to be influencing landslide activity at some locations (Tappenden 2014, Schafer 2016) are likely widespread within this region. This seasonal movement trend is most evident at the Ripley, Red Hill, and Goddard slides, which experience increased deformations during the late fall and winter months versus relative stability during the spring and summer.

Table 5-9 presents a summary of PSI deformation data for all active AOI, showing LOS deformation rates, estimated downslope deformation rates, as well as the season of highest activity.

Table 5-9: Summary of PSI Deformation Data for All AOI

AOI	Average LOS Deformation Rate (mm/year)			Average Downslope[1] Deformation Rate (mm/yr)		Season of Highest Observed Activity, if Applicable
	U5	U21	F4N	Average	Max	
Ripley	-34	-39	21	49	77	November - March
Red Hill Toe	12	19	-23	37	89	October – March
Goddard Toe	-12	-14	N/A	31	120	November – Feb.
South Extension	-16	-17	12	26	73	N/A
North Slide Toe	-11	-14	-4	25	81	N/A
Barnard	-9	-11	2	10	50	March - October

1. Calculated using a weighted average biased to PSI datasets with higher percent coverage.

Comparing the time-series behavior of each AOI to one another in terms of LOS deformation is difficult and of limited use given the varying slope geometries and other conditions mentioned previously. To address this, the average LOS time-series deformation of each AOI has been scaled using methods outlined earlier in Section 3.2.3.3. The result of this scaling is presented in the following figures, which show the time-series deformation of each active AOI.

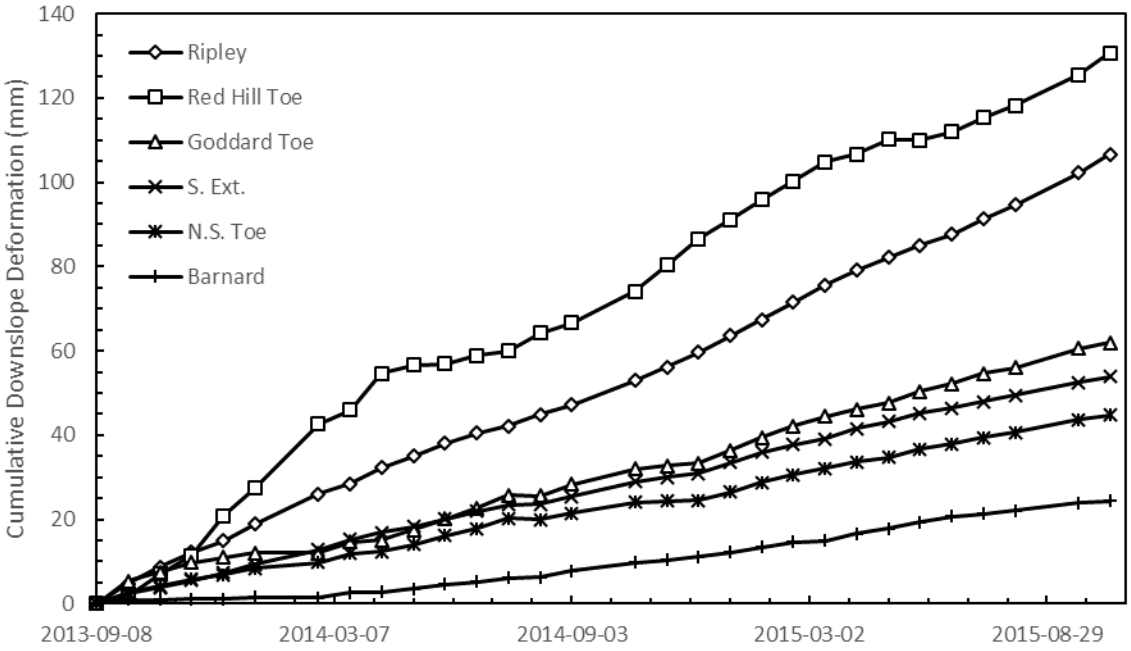

Figure 5-19: Scaled Downslope Deformation of All AOI - U5 Dataset

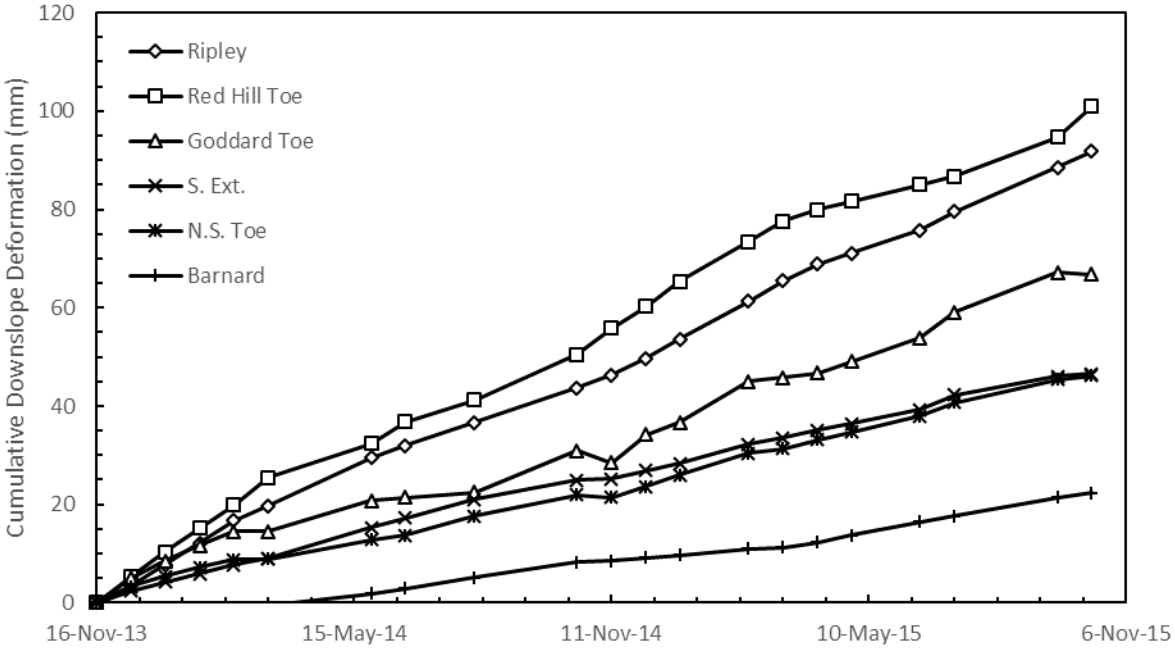

Figure 5-20: Scaled Downslope Deformation of All AOI - U21 Dataset

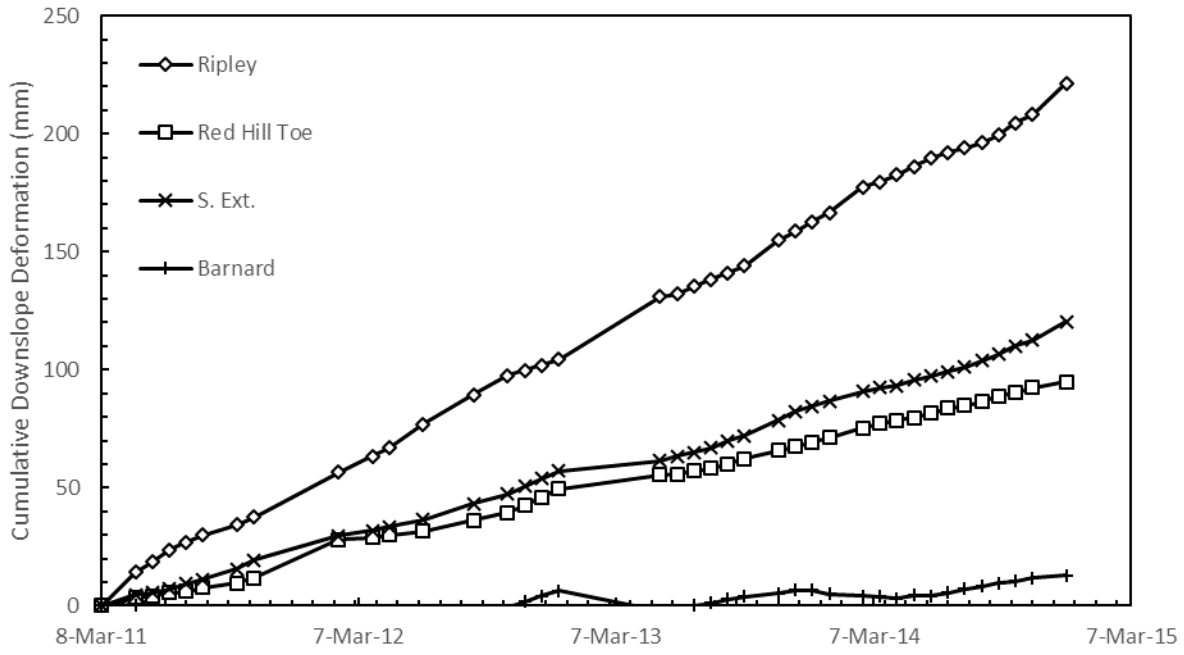

Figure 5-21: Scaled Downslope Deformation of All AOI - F4N Dataset

Based on the preceding figures it is evident that the Ripley and Red Hill slides are the most active sites within the study area, each deforming in a downslope direction at an average rate of 49 and 37 mm/year, respectively. Both sites show signs of seasonal variability, with elevated deformation observed in the late fall and winter months. At the Ripley Slide, this variation has been attributed to pore pressure fluctuations induced by changes in the volume of flow in the Thompson River. The similarity in movement patterns and proximity of the two sites suggest that a similar mechanism may be affecting movements at the Red Hill Slide as well.

Grouped together at a lower activity level relative to the previous two landslides are the South Extension, Goddard toe, and North Slide toe. Each of these sites deform in their respective downslope directions at estimated rates ranging between 25 and 31 mm/year. Of these three sites, only the Goddard expresses a seasonal pattern of movement that is most active during the late fall and winter months. In contrast, the South Extension and North Slide toe show little to no seasonal variability overall, with only select CTs from within these AOI showing variable

movement patterns. The mechanisms controlling deformation at these sites should thus be considered subjects of future study.

Finally, the Barnard slide has been identified as the least active site within the study area, moving only an average of 10 mm/year in the downslope direction. Despite this slow rate of deformation, this site remains interesting due to the unique seasonal pattern of movement observed at the site. Whereas other AOI in the corridor are most active during the late fall and winter months, the Barnard Slide shows the opposite pattern, being most active from the spring to early fall. The reason for this unique movement pattern is unknown and remains a question for future study.

6.0 Conclusions

For several years InSAR has been used successfully to measure and delineate ground deformations over very wide areas, many of which contain landslides. The technology itself is ever evolving, with more advanced satellites and new algorithmic processing techniques continuously under development to address new problems or improve existing methods. With each advancement comes new opportunities to study ever more challenging areas, both large and small. The Thompson River Valley south of Ashcroft, B.C. is one such area known to contain many large landslide features of varying levels of activity. It is an ideal study location due to the high concentration of active sites, the radar reflective properties of the ground cover, the wealth of geotechnical studies previously carried out in the valley, as well as the economic importance of the two major railway lines running through the corridor. The launch of RADARSat-2 in 2007 by the CSA brought with it the opportunity to carry out a detailed study of landslide activity in the corridor using the satellite's increased imaging resolution and accuracy.

This work has drawn on the understanding garnered from previous and ongoing studies of specific sites within the Ashcroft area, each of which have helped to increase the collective understanding of the triggers and mechanisms affecting the behavior of landslides in the Thompson River Valley. The analysis presented in this thesis was carried out with the broad goal of utilizing satellite InSAR data to identify and compare the most active areas of instability within the corridor to one another.

Achieving this goal first required the validation of InSAR results using ground-based instrumentation data and observations wherever possible. At the three sites chosen for this purpose, the Ripley Slide, South Extension, and a local pump station, this validation effort was largely successful, showing good agreement between InSAR data and expected ground behavior. Where discrepancies were observed, extenuating circumstances or localized phenomena could often be drawn upon to explain the inconsistencies in the available data rather than calling into question the validity of InSAR analysis itself. The conclusion of this portion of the study is that the

InSAR data from within the Thompson River Valley is indeed valid and thus is a viable tool for studying landslide activity within the corridor.

Expanding InSAR analysis to the broader study area revealed a total of six zones of active ground deformation, all of which are located within existing or historic landslide footprints. The most active of the identified sites are the Ripley and Red Hill slides, both of which express clear seasonal variations in all PSI datasets. These are followed by the Goddard Toe, South Extension, and North Slide Toe, which each exhibit a similar level of deformation activity to one another. Finally, the Barnard slide stands alone as the least active AOI within the study area, showing subdued yet steady deformation over time.

The behavior of these sites can in some cases be attributed to mechanisms known to exist within the study area. For instance, the seasonal variability of the Ripley and Red Hill slides is likely directly attributable to fluctuations in pore water pressures induced by changes in river flow volumes. River erosion is also a major contributor to localized instability at the Red Hill, North Slide, and Goddard Slide toes. Conversely, the mechanism(s) of action affecting the South Extension and Barnard slides are largely unknown and should form the basis of further study.

Though the results of this work provide valuable insight into landslide activity in the corridor, there remain limitations that would improve the level of understanding gained from similar work if addressed. First of these is the fact that the direction of ground movement at most sites had to be assumed prior to estimating the magnitude of deformation in the downslope direction. If the actual ground surface deformation vectors were known, the comparison of AOI movements to one another would be of much greater validity. Further improvement could be gained by acquiring SAR images from a different orbital geometry. Such data could be selected to improve the coverage of sites whose geometry was shown to be unfavorable in this study.

6.1. Recommendations for Future Research

The opportunities for further research in the Ashcroft area based on the results of this study are many. An obvious choice would be to carry out a detailed kinematic analysis of active AOI within the corridor, especially at those sites where the mechanism of action is not precisely known (South Extension, North Slide Toe, and Barnard Slide). Such a study would not only further improve the understanding of instabilities in the area, but would also allow for a better grouping or classification of landslides based on kinematic behavior rather than on deformation rate alone. A second opportunity for study would be to compare the results of InSAR analysis to recorded changes in railway track geometry through the corridor. Doing so would help to further delineate the extent of active AOI, as well as potentially identify smaller zones of instability that are less apparent in the PSI results. Finally, a study of the potential correlation between observed landslide seasonality and environmental or climactic changes could yield valuable insight into both past and future landslide behavior in the area.

References

Barry, J.W. 1897. The Great Land-Slides on the Canadian Pacific Railway in British Columbia. *In* The Institution of Civil Engineers. *Edited by* R.B. Stanton. Victoria, B.C. pp. 1–21.

Bishop, N.F. 2008. Geotechnics and hydrology of landslides in Thompson River Valley, near Ashcroft, British Columba. University of Waterloo.

Clague, J.J., and Evans, S.G. 2003. Geologic framework of large historic landslides in Thompson River Valley, British Columbia. Environmental & Engineering and Geoscience, **IX**(3): 201–212.

Cloutier, C., Locat, J., Charbonneau, F., and Couture, R. 2015. Understanding the kinematic behavior of the active Gascons rockslide from in-situ and satellite monitoring data. Engineering Geology, **195**: 1–15. Elsevier B.V. doi:10.1016/j.enggeo.2015.05.017.

Colesanti, C., Ferretti, A., Prati, C., and Rocca, F. 2003. Monitoring landslides and tectonic motions with the Permanent Scatterers Technique. Engineering Geology, **68**(1–2): 3–14. doi:10.1016/S0013-7952(02)00195-3.

Colesanti, C., and Wasowski, J. 2006. Investigating landslides with space-borne Synthetic Aperture Radar (SAR) interferometry. Engineering Geology, **88**(3–4): 173–199. doi:10.1016/j.enggeo.2006.09.013.

Cruden, D.M., and Varnes, D.J. 1996. Landslide types and processes. *In* Special Report - Transportation Research Board, National Research Council, Washington, DC, United States. National Academy of Sciences.

CSA. 2015. Satellite Characteristics. Available from http://www.asc-csa.gc.ca/eng/satellites/radarsat/radarsat-tableau.asp [accessed 16 October 2015].

Eshraghian, A. 2007. Hazard Analysis of Reactivated Earth Slides in the Thompson River Valley, Ashcroft, British Columbia. University of Alberta.

Eshraghian, A., Martin, C.D., and Cruden, D.M. 2007. Complex Earth Slides in the Thompson River Valley, Ashcroft, British Columbia. Environmental and Engineering Geoscience, **13**(2): 161–181. doi:10.2113/gseegeosci.13.2.161.

Eshraghian, A., Martin, C.D., and Morgenstern, N.R. 2008. Movement triggers and mechanisms of two earth slides in the Thompson River Valley, British Columbia, Canada. Canadian Geotechnical Journal, **45**(9): 1189–1209. doi:10.1139/T08-047.

ESRI. 2015. ArcGIS 10.3 for Desktop. ESRI Inc. Available from https://www.esri.com/software/arcgis/arcgis-for-desktop.

Ferretti, A., Monti-guarnieri, A., Prati, C., Rocca, F., and Massonnet, D. (CNES). 2007. InSAR processing: a mathematical approach (Part C). *In* InSAR Principles: Guidelines for SAR Interferometry Processing and Interpretation. *Edited by* K. Fletcher. ESA Publications, Noordwijk. pp. 120–234.

Froese, C.R., Keegan, T.R., Cavers, D.S., and van der Kooij, M. 2005. Detection and monitoring of complex landslides along the Ashcroft rail corridor using spaceborne InSAR. *In* Landslide Risk Management. *Edited by* Hungr, Fell, Couture, and Eberhardt. Taylor & Francis Group, London. pp. 565–570.

Hendry, M., Macciotta, R., Martin, C.D., and Reich, B. 2015. Effect of Thompson River elevation on velocity and instability of Ripley Slide. Canadian Geotechnical Journal, **52**(July 2014): 257–267. doi:10.1139/cgj-2013-0364.

Kosar, K., Revering, K., Keegan, T.R., Black, K., and Stewart, I. 2003. The use of spaceborne InSAR to characterize ground movments along a rail corridor and open pit mine. *In* Canadian Conference on Geotechnique and Natural Hazards. Edmonton, AB. pp. 177–184.

Macciotta, R., Hendry, M., and Martin, C.D. 2015. Developing an early warning system for a very slow landslide based on displacement monitoring. Natural Hazards, **81**(2): 887–907. Springer Netherlands. doi:10.1007/s11069-015-2110-2.

Newcomen, W., and Pritchard, M. 2009. CN ASH Sub Mile 55.2 / CPR THOM Sub Mile 52.80 South and Inner South Slide October 28, 2009 Monitoring Event. Kamloops.

Porter, M.J., Savigny, K.W., Keegan, T.R., Bunce, C., and Mackay, C. 2001. Controls on stability of the Thompson River landslides. *In* 55th Canadian Geotechnical Conference. pp. 1393–1400.

Roberts, M., Danielson, J., and Schmid, C. 2015. CN ASH Sub Mile 55.2/CPR THOM Sub Mile 52.90 South and Inner South Slide April 7, 2015 Monitoring Event. Kamloops.

Sandwell, D.T., and Price, E.J. 1998. Phase gradient approach to stacking interferograms. Journal of Geophysical Research: Solid Earth, **103**(B12): 30183–30204. doi:10.1029/1998JB900008.

Schafer, M. 2016. Kinematics and Controlling Mechanics of the Slow Moving Ripley Landslide. University of Alberta.

Schafer, M., Macciotta, R., Hendry, M., Martin, C.D., Bunce, C., Choi, E., and Edwards, T. 2015. Instrumenting and Monitoring a Slow Moving Landslide. *In* 68th Canadian Geotechnical Conference. Quebec City.

Simons, M., and Rosen, P. a. 2007. Interferometric Synthetic Aperture Radar Geodesy. *In* Treatise on Geophysics. *Edited by* T. Herring and G. Schubert. Elsevier. pp. 391–446. doi:10.1016/B978-0-12-386874-9.00010-5.

Tappenden, K.M. 2014. Climatic Influences on the Ashcroft Thompson River Landslides, British Columbia, Canada. *In* Canadian Conference on Geohazards. Kingston, Ontario, Canada. pp. 15–17.

Wasowski, J., and Bovenga, F. 2014. Investigating landslides and unstable slopes with satellite Multi Temporal Interferometry: Current issues and future perspectives. Engineering Geology, **174**: 103–138. Elsevier B.V. doi:10.1016/j.enggeo.2014.03.003.

van Zyl, J. 2009. Radar Remote Sensing for Earth and Planetary Sciences. Pasadena, CA.

Appendix A

PSI Movement Intensity Maps

A.1. Ripley Slide

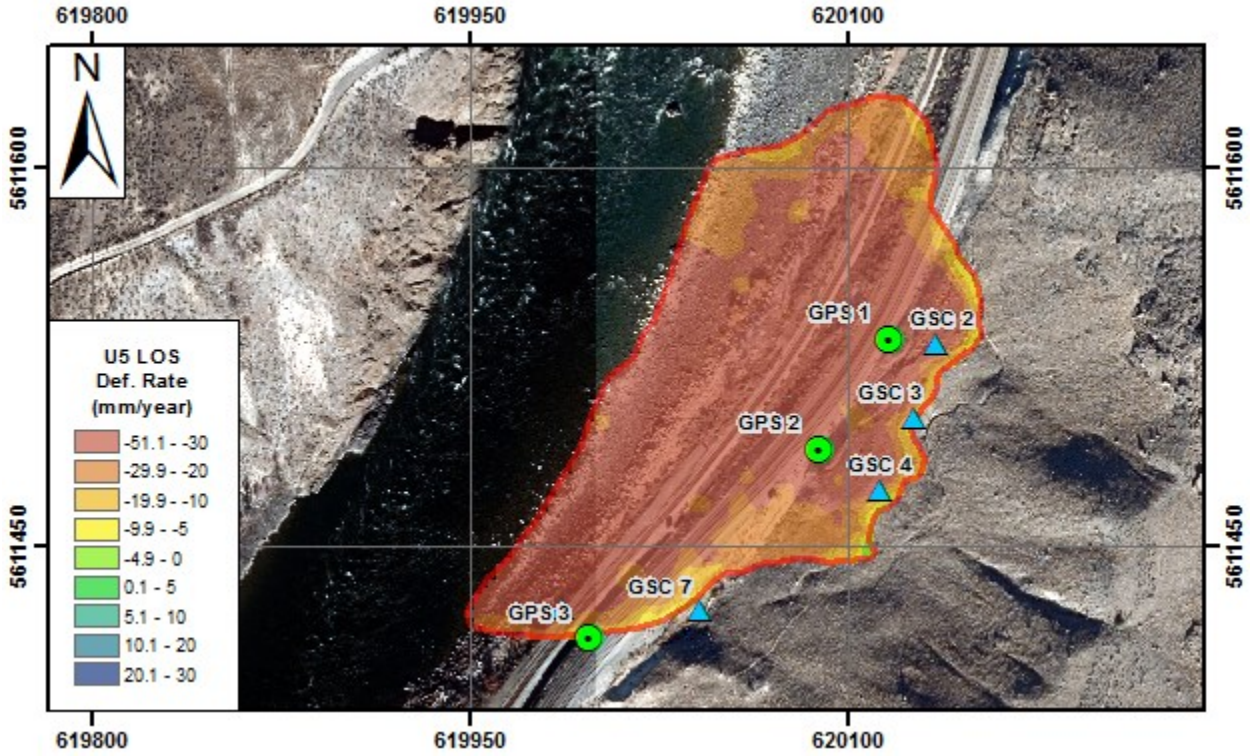

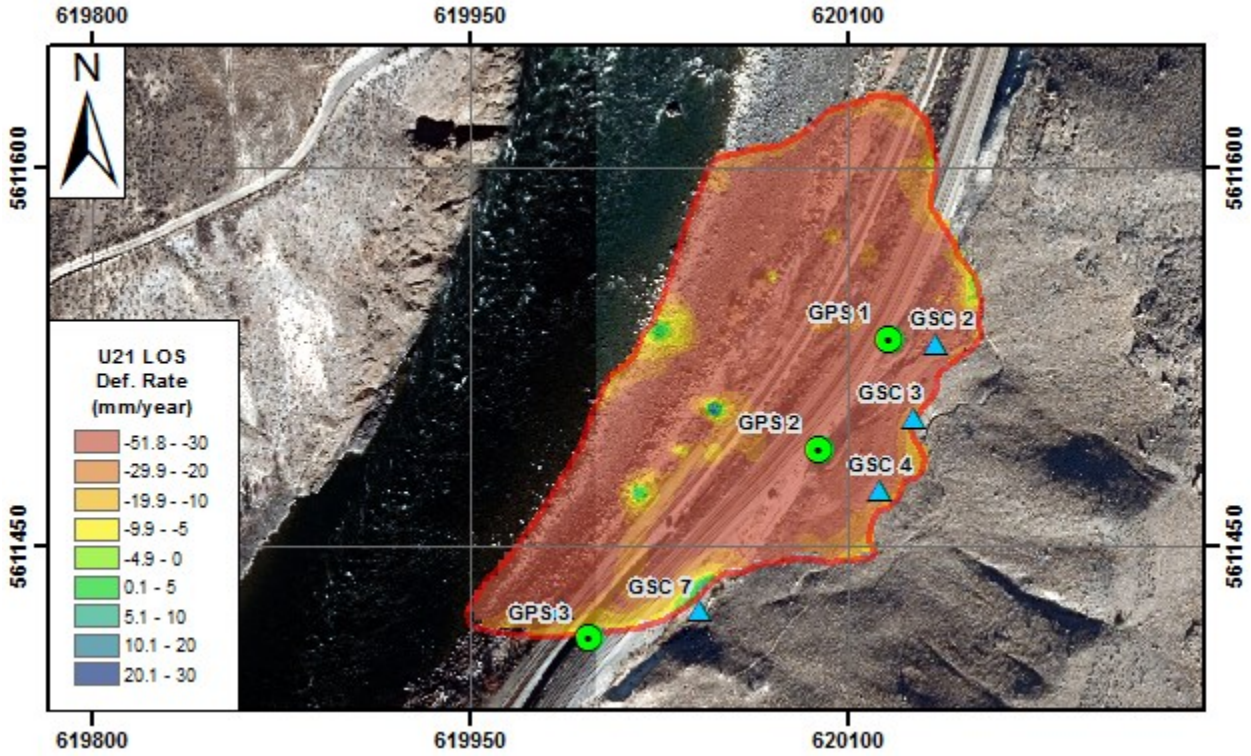

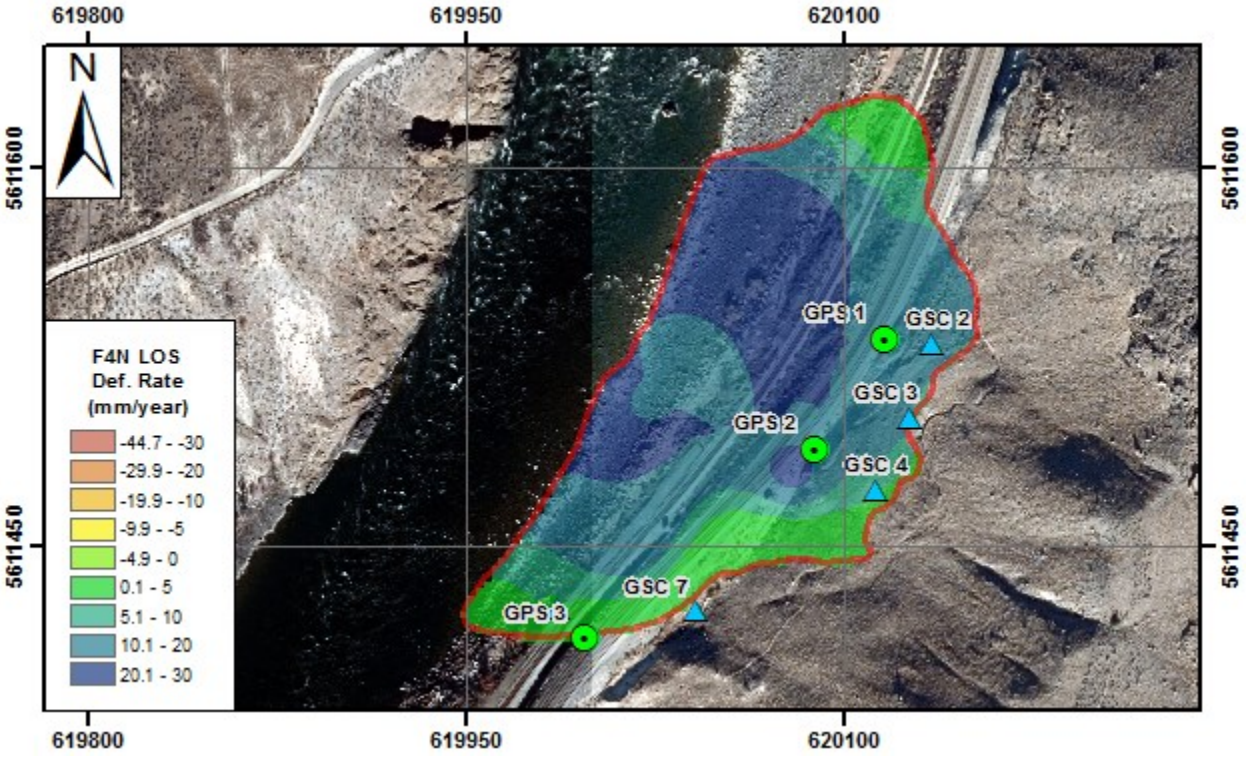
619800
619950
620100
5611600
5611450
N
F4N LOS
Def. Rate
(mm/year)
-44.7 - -30
-29.9 - -20
-19.9 - -10
-9.9 - -5
-4.9 - 0
0.1 - 5
5.1 - 10
10.1 - 20
20.1 - 30
GPS 1
GSC 2
GSC 3
GPS 2
GSC 4
GSC 7
GPS 3

A.2. South Slide

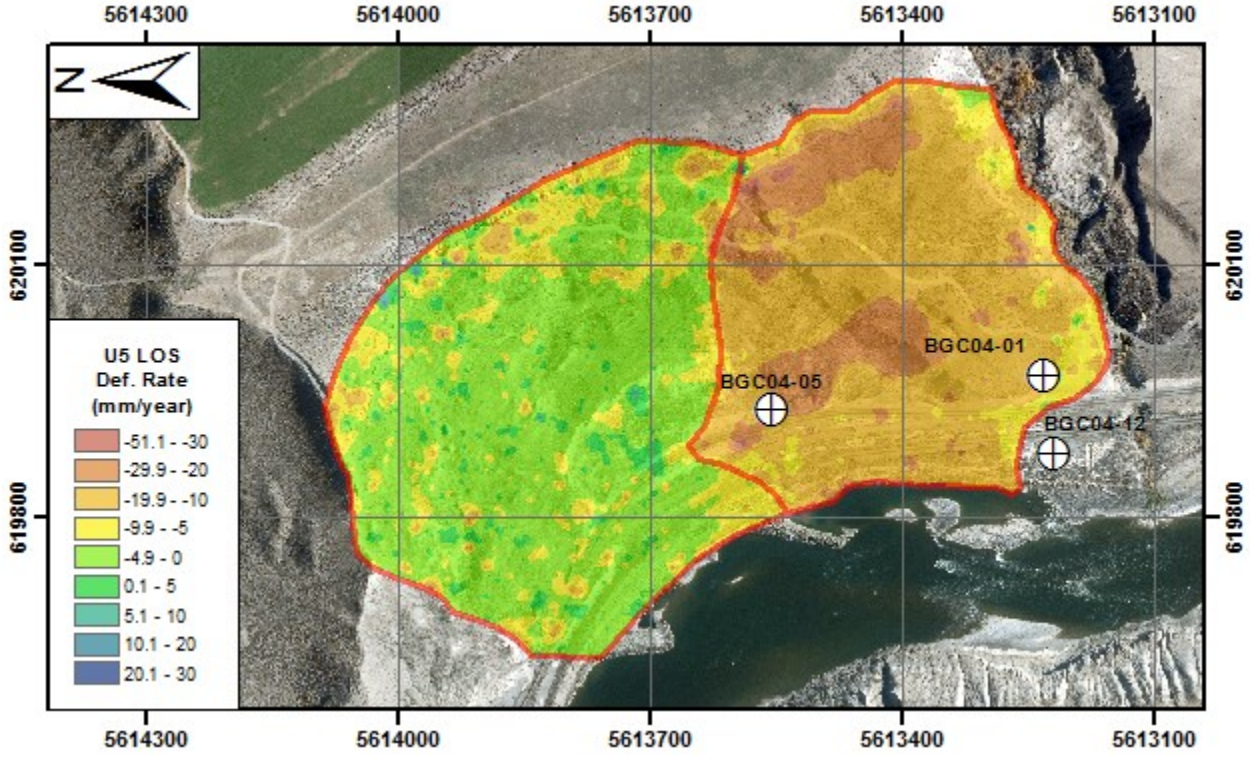

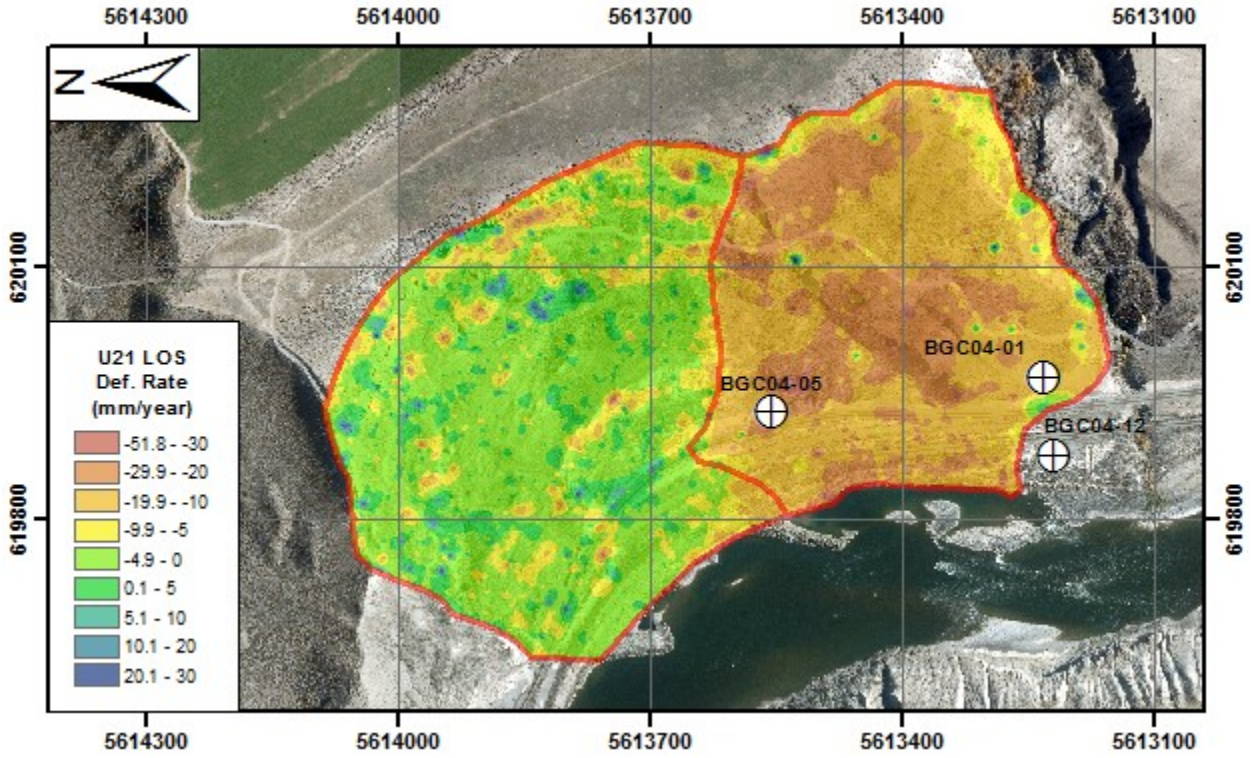

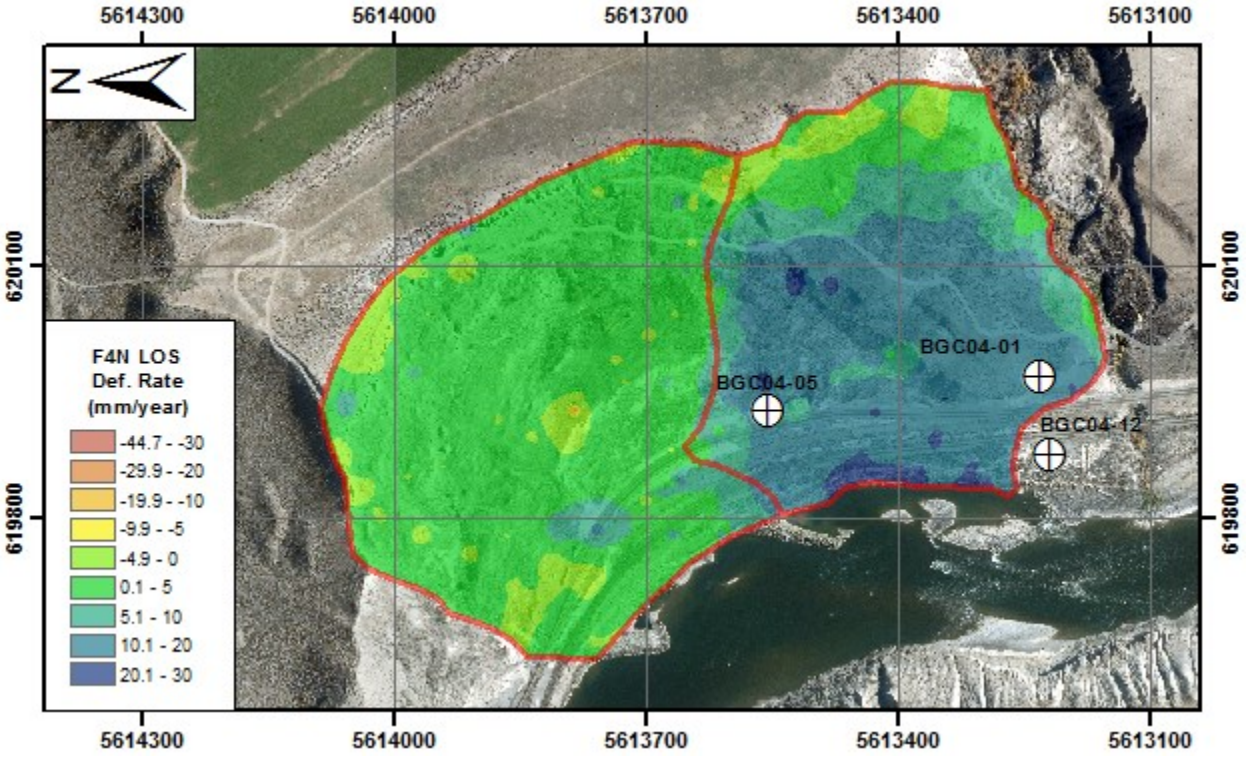
5614300
5614000
5613700
5613400
5613100
620100
619800
N
F4N LOS
Def. Rate
(mm/year)
-44.7 - -30
-29.9 - -20
-19.9 - -10
-9.9 - -5
-4.9 - 0
0.1 - 5
5.1 - 10
10.1 - 20
20.1 - 30
BGC04-01
BGC04-05
BGC04-12

A.3. Red Hill Slide

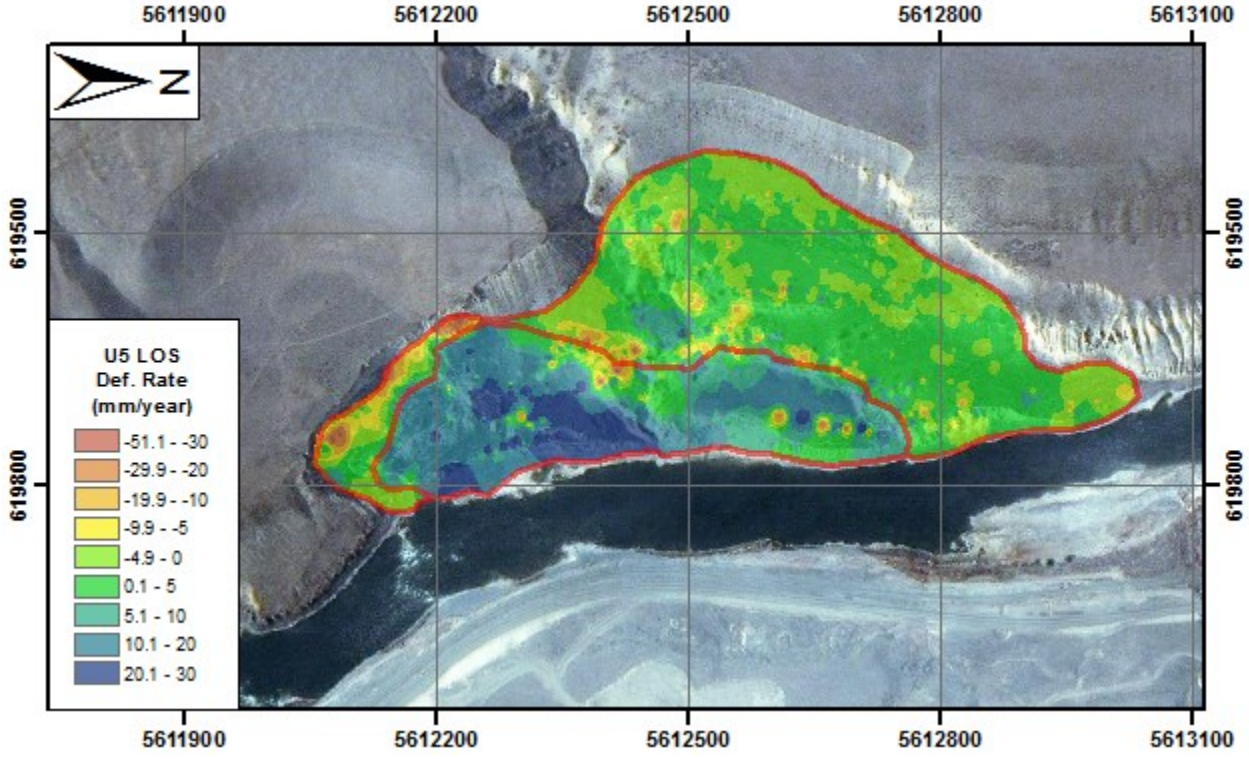

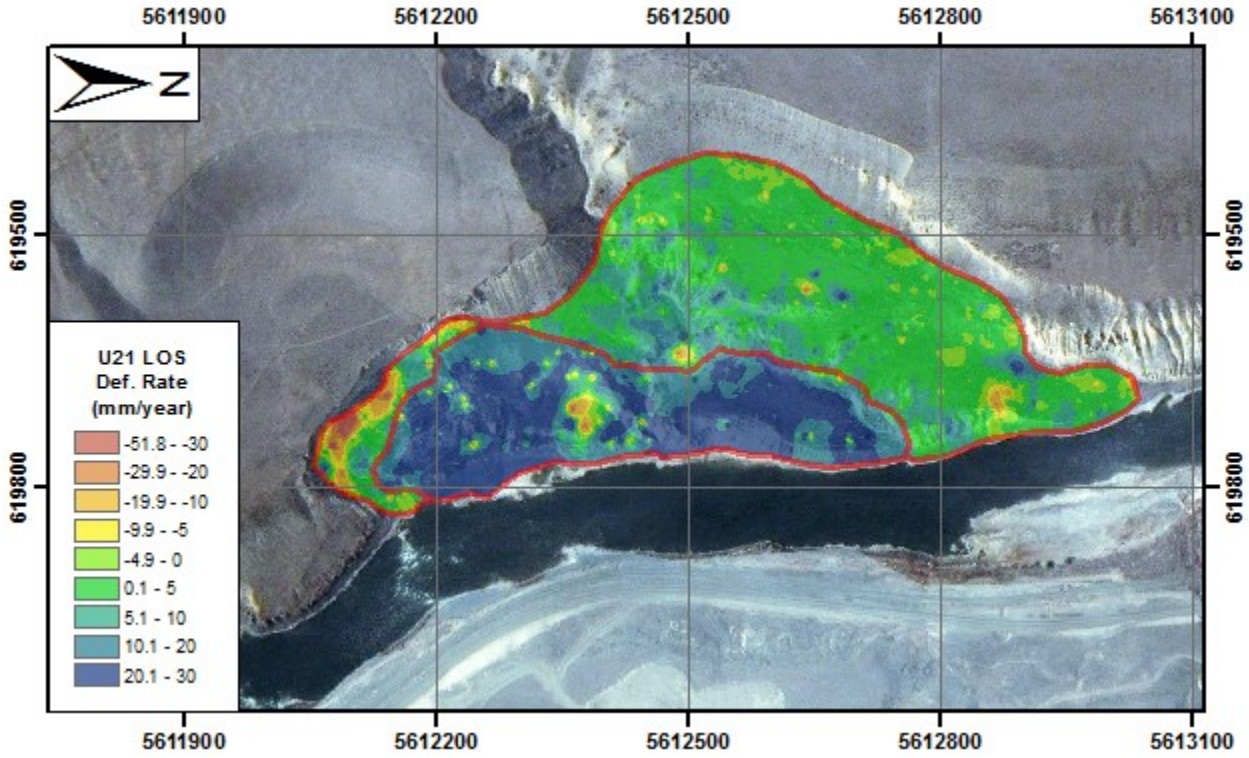

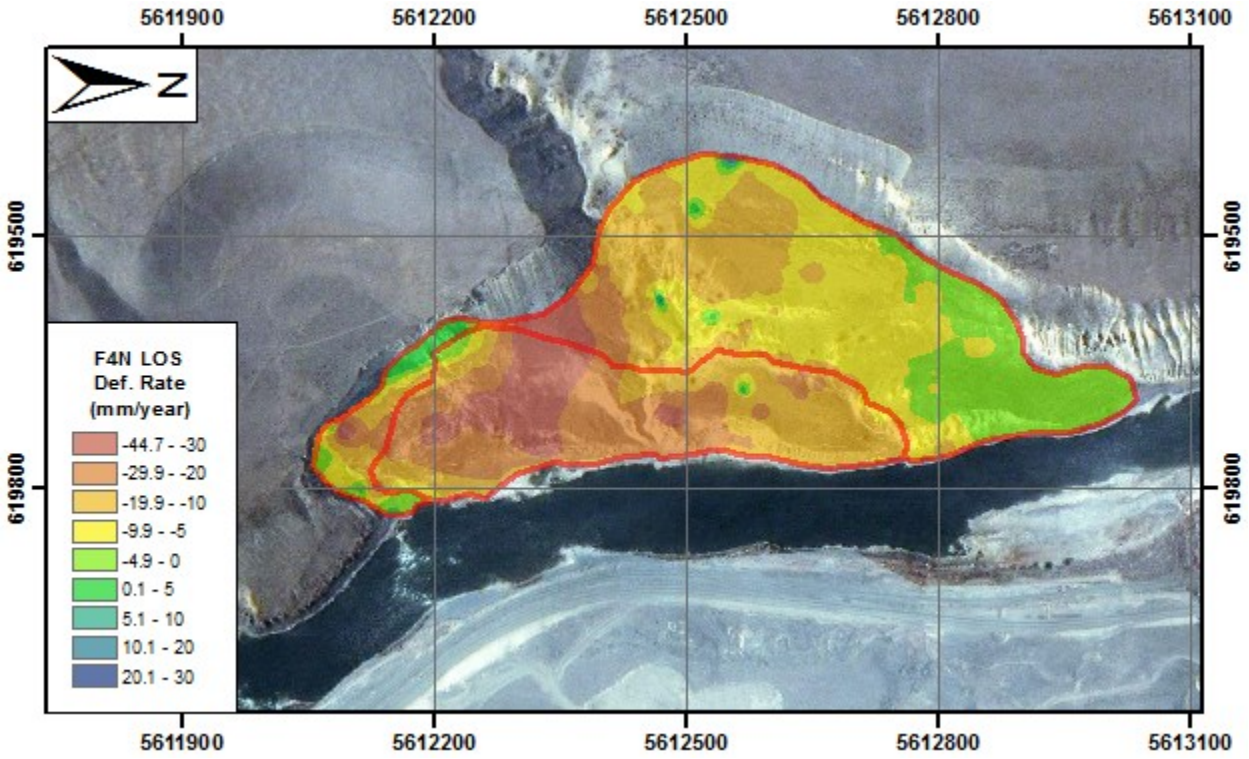
5611900
5612200
5612500
5612800
5613100
619500
619800
N
F4N LOS
Def. Rate
(mm/year)
-44.7 - -30
-29.9 - -20
-19.9 - -10
-9.9 - -5
-4.9 - 0
0.1 - 5
5.1 - 10
10.1 - 20
20.1 - 30

A.4. Barnard Slide

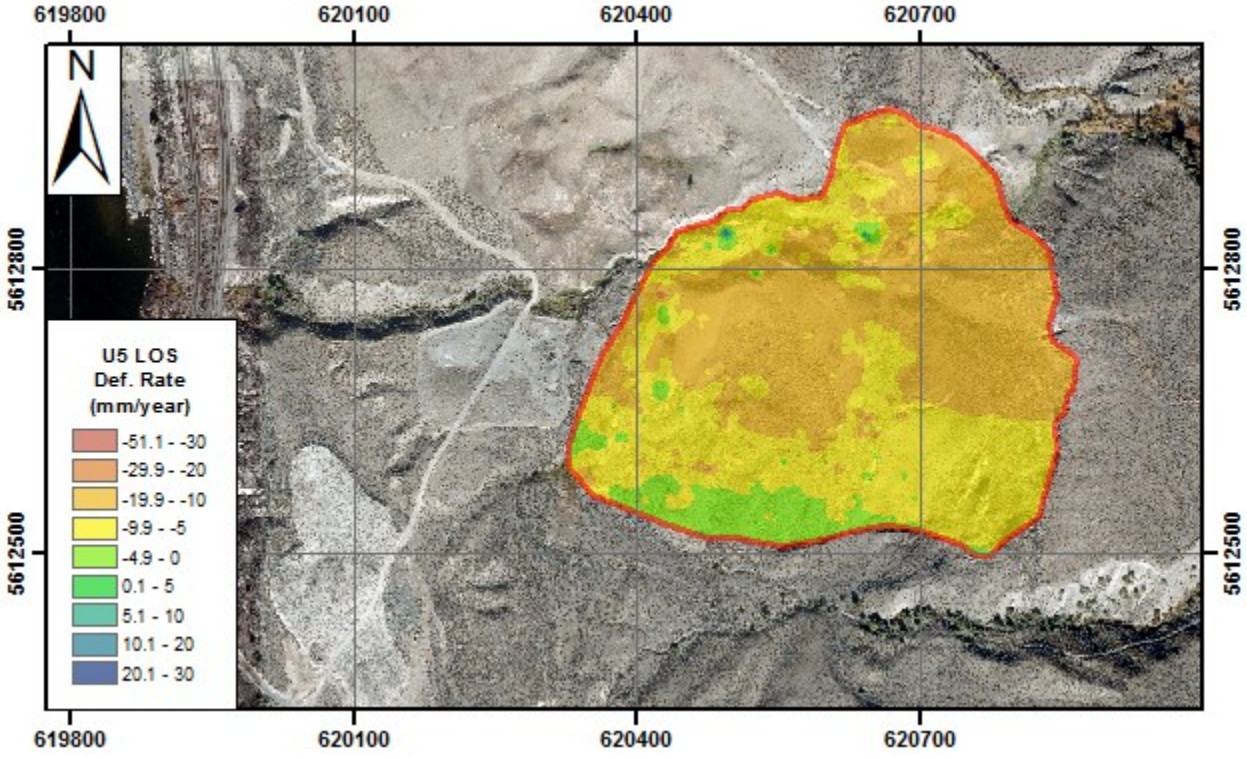

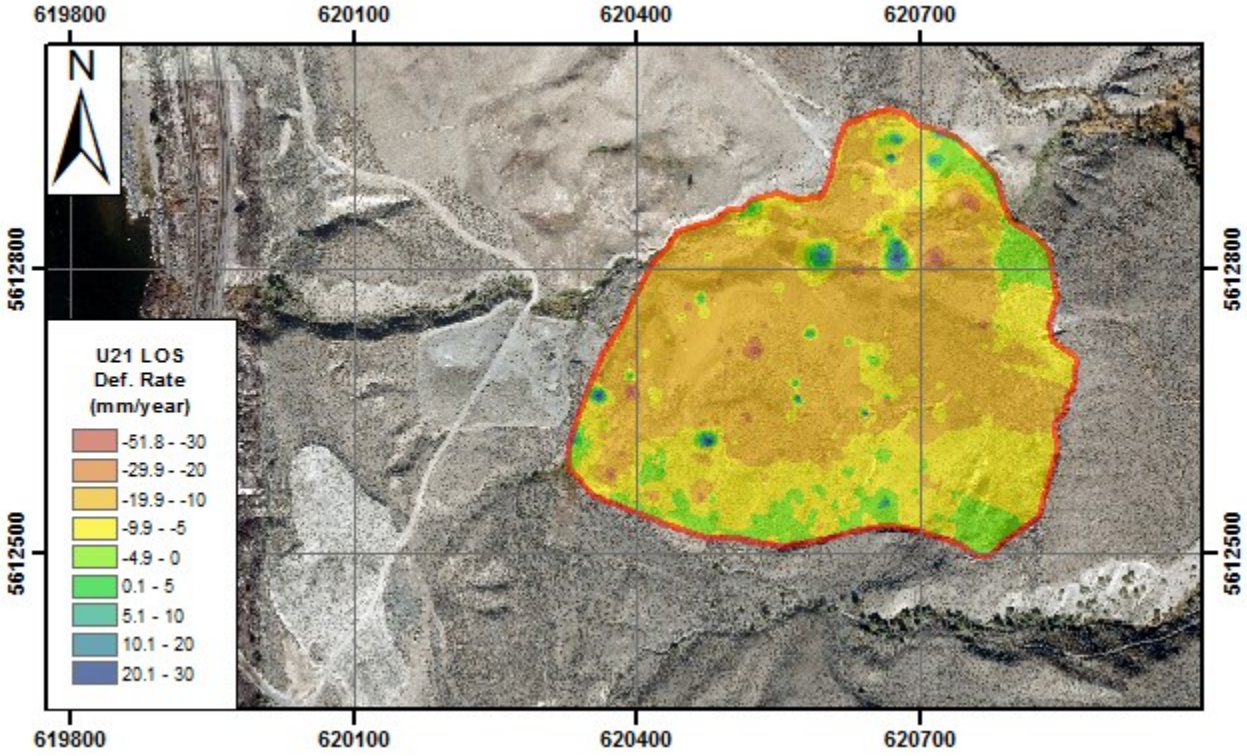

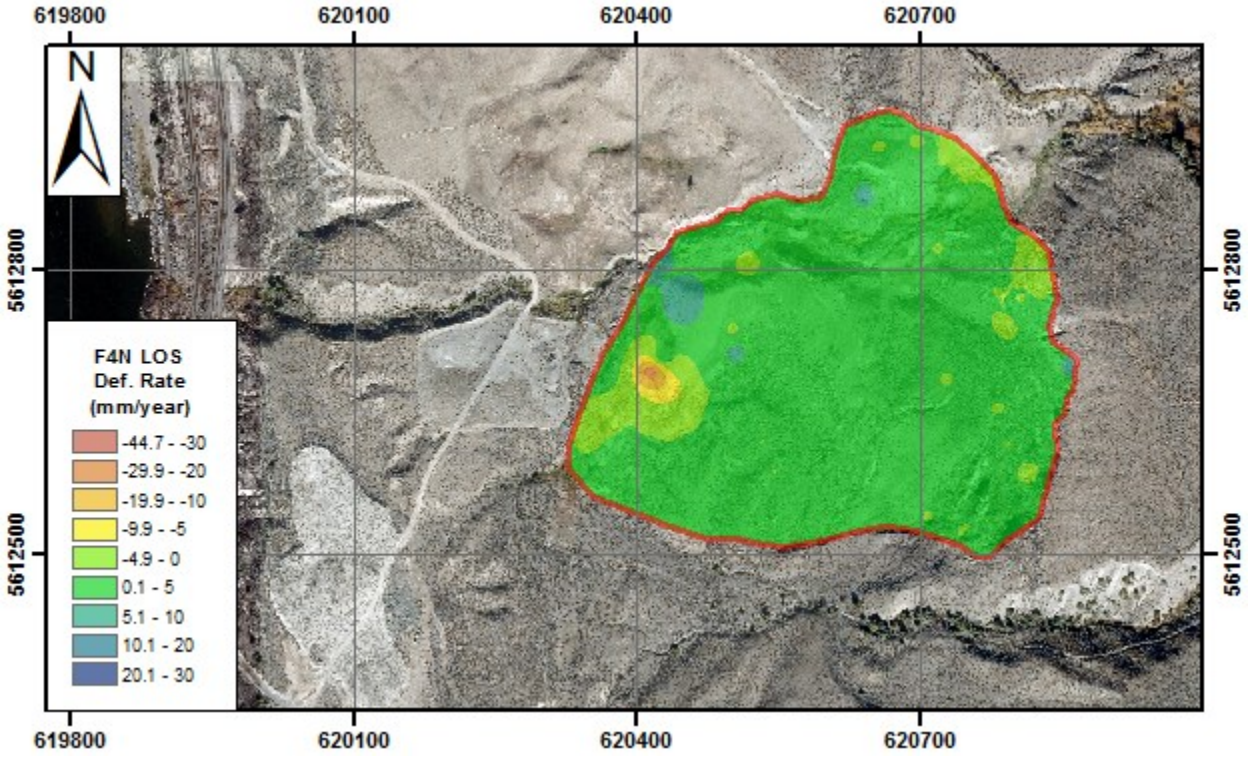
619800
620100
620400
620700
N
5612800
5612500
F4N LOS
Def. Rate
(mm/year)
-44.7 - -30
-29.9 - -20
-19.9 - -10
-9.9 - -5
-4.9 - 0
0.1 - 5
5.1 - 10
10.1 - 20
20.1 - 30

A.5. North Slide

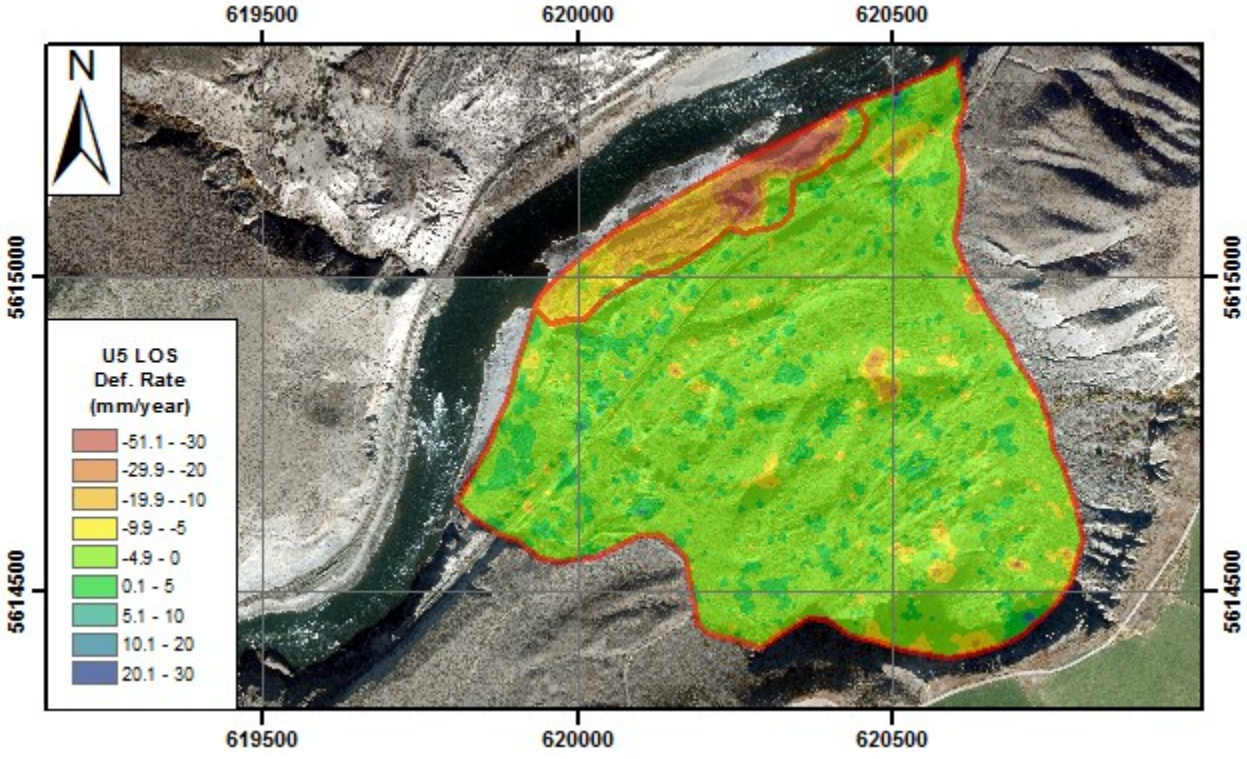

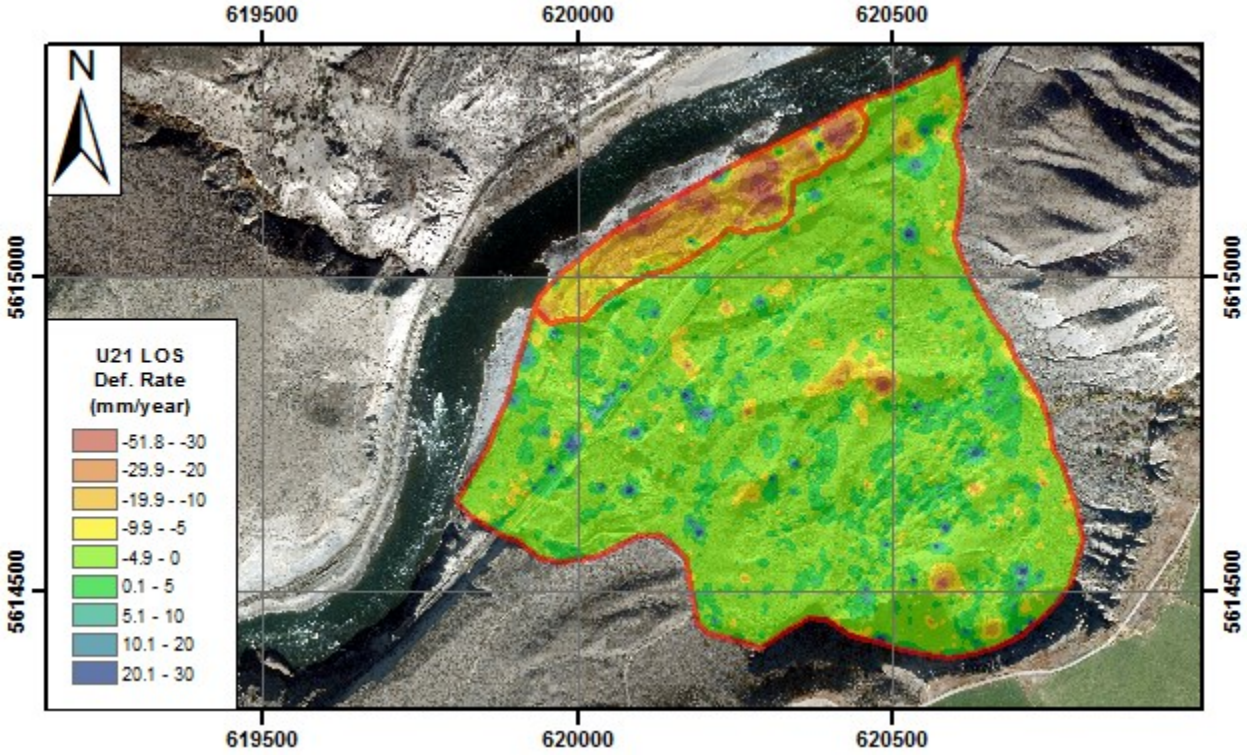

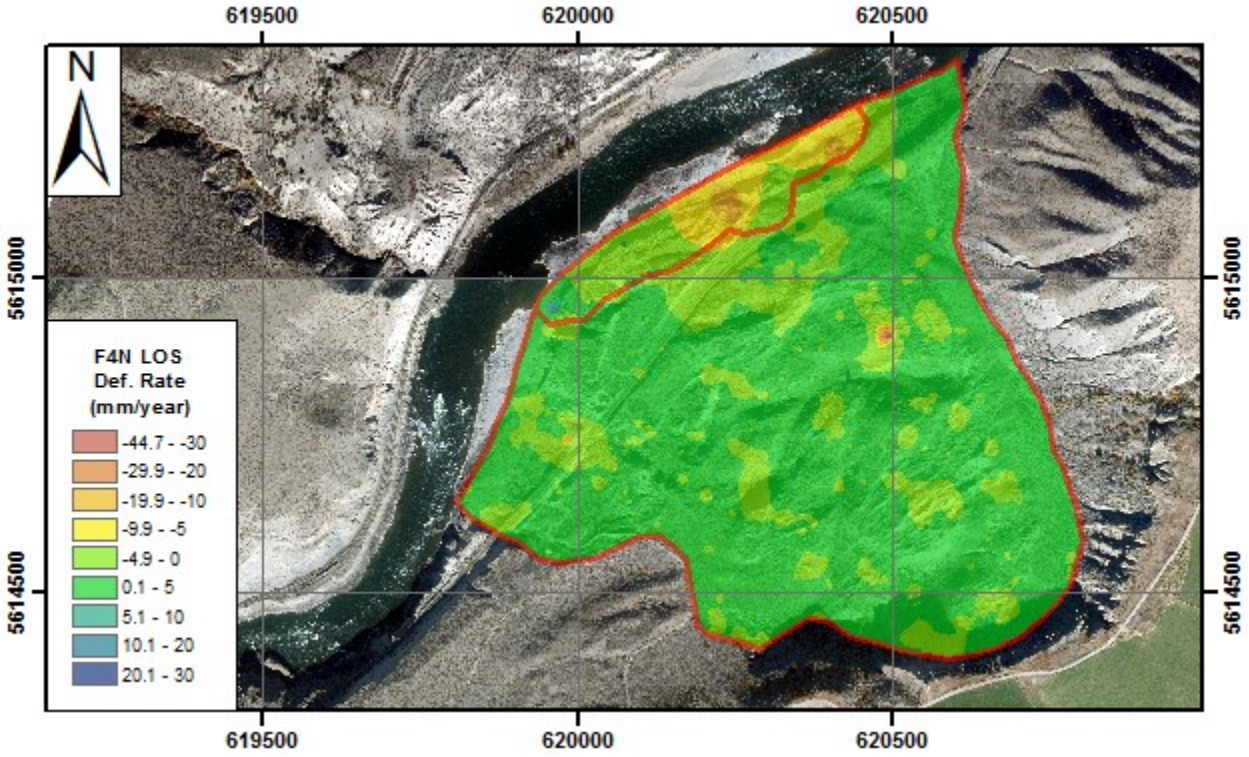
619500
620000
620500
5615000
5614500
N
F4N LOS
Def. Rate
(mm/year)
-44.7 - -30
-29.9 - -20
-19.9 - -10
-9.9 - -5
-4.9 - 0
0.1 - 5
5.1 - 10
10.1 - 20
20.1 - 30

A.6. Goddard Slide